Faculty of Aerospace Engineering

Stall Buffet Modeling using Swept Wing Flight Test Data

Sven Marschalk
October 2019

TU Delft

Stall Buffet Modeling using Swept Wing Flight Test Data

by

Sven Marschalk

to obtain the degree of Master of Science
at the Delft University of Technology,
to be defended publicly on Tuesday October 8, 2019 at 14:00.

Student number:	4595408	
Project duration:	September 10, 2018 – October 8, 2019	
Thesis committee:	Dr. ir. Q.P. Chu,	TU Delft, AE, Control & Simulation
	Dr. ir. C.C. de Visser,	TU Delft, AE, Control & Simulation
	Dr. ir. D.M. Pool,	TU Delft, AE, Control & Simulation
	Dr. J. Sodja,	TU Delft, AE, Structures & Computational Mechanics
	D. van Os,	Fokker Services B.V.

An electronic version of this thesis is available at `http://repository.tudelft.nl/`.

TU Delft

Preface

Dear reader,

In this report, I proudly present my one year's worth of work. The results presented contribute to the stall task force research group within the Control and Simulation department of the faculty of Aerospace Engineering. The goal is to develop a new system identification methodology to create generic stall models, which accurately capture aircraft stall behavior, currently for smaller aircraft manufacturers. However, the results in the research combined with concurrent and previous research could identify a more generic stall modeling methodology, for small to medium type aircraft. Ultimately, accurate stall models will increase pilot awareness and training effectiveness, mitigating LOC-I occurrences and contribute to aviation safety.

In the summer of 2018, I was looking for a research topic for my master's thesis. During a lecture on system identification, the topic of stall modeling using a system identification approach piqued my interest. Several meetings and thesis topic changes later, I could finally start my research into stall buffet modeling of the Fokker 100. I was motivated to start my thesis, as I could work with real-life flight test data, I could (hopefully) make a contribution to the industry, and I was able to experience aircraft stalls. However, I soon found out that working with real-life flight data posed a lot of challenges, which required perseverance, patience, and friends to overcome those challenges.

Therefore, I would like (personally) thank everyone involved. First of all, I would like to thank my supervisor Coen, who provided me with this amazing research opportunity as well as a lot of support and feedback. However, the research would not have been possible without the Fokker data and therefore I would like to thank Dirk, who provided the university with a large data set of stall maneuvers of the Fokker 100. Peter, a huge shout out to you for spending so much time on structuring the data and for all the help during my thesis. Daan thank you for the input, feedback, and laughs during the stall group meetings. A special thanks to Simon, Peter, Stephan, Michiel, Marc, and Joeri as C&S Upperhouse members, who have made the thesis so much more bearable. Thank you guys, for all the shared knowledge and wisdom, the (late night) music intermezzos, the strolls around campus, the inside jokes, the "we are only going for one drink" policy at the wobo's and vrimibo's, and the relaxed working atmosphere. Also a special thank you to Ankit, Leonor, Tiago, and Rohan, for all the drinks, dinners, vacation, chill sessions, parties, laughs, and relaxed working atmosphere. Alex, Arjen, Marc, Martin, and Remco, thank you guys for the motivation during the bridging program and master. So glad you all were along for the ride, and I wish you all the best. I would not have been able to graduate in a year if it were for you all, it would probably have been a lot sooner. Niek, thank you as well for your support and motivation during our phone calls. Lastly, and most importantly I would like to thank my mom, Genet, Jorn, and Linda for their unconditional love and support.

A short and final note on the structure of the work presented. In the first part, a scientific paper summarizing the main results of my thesis. Secondly, a preliminary report, including preliminary results and a literature study, is presented. Lastly, the appendices contain information on the research which was not included in the paper.

Contents

List of Figures

List of Tables

Nomenclature

Abbreviations

ADC	Air Data Computers
AFCAS	Automatic Flight Control and Augmentation System
AHRS	Attitude and Heading Reference System
AHS	Attitude and Heading System
AOM	Aircraft Operations Manual
ASP	Altimeter Set Panel
CAST	Commercial Aviation Safety Team
CFD	Computational Fluid Dynamics
CICTT	CAST/ICAO Common Taxonomy Team
CRLB	Cramér–Rao lower bound
DASMAT	Delft University Aircraft Simulation Model and Analysis Tool
DUECA	Delft University Environment for Communication and Activation
EASA	European Aviation Safety Agency
FAA	Federal Aviation Administration
FDVS	Fokker Data Verwerking Systeem
FEM	Finite Elements Method
FMS	Flight Management System
FSTD	Flight Simulation Training Devices
HARV	High-Angle-of attack Research Vehicle
ICAO	International Civil Aviation Organisation
ICATEE	International Committee for Aviation Training in Extended Envelopes
IMU	Inertial Measurement Unit

IRS	Inertial Reference System
ISDU	Inertial System Display Unit
JAA	Joint Aviation Authorities
JAR	Joint Aviation Requirements
LOC-I	Loss of Control-Inflight
MRVS	Meet en Registratie en Verwerkings Systeem
MSE	Mean Squared Error
MSU	Mode Select Unit
MTOM	Maximum Take-Off Mass
NASA	National Aeronautics and Space Administration
OLE	Ordinary Least Squares
PSD	Power Spectral Density
RAeS	Royal Aeronautical Society
RANS	Reynolds-Averaged Navier-Stokes
RMS	Root Mean Square
SME	Subject Matter Experts
SQL	Structured Query Language
STB	STandaard Berekeningen
SUPRA	Simulation of Upset Recovery in Aviation
TAS	True Airspeed
TBD	To Be Determined
TRS	Test Result Summary
UPRT	Upset Prevention and Recovery Training
UTIAS	University of Toronto Institute for Aerospace Studies

Latin Symbols

Symbol	**Description**	**Unit**
a_1	Abruptness of the stall of the flow separation parameter X	-
A	Aspect ratio	-
A_X	Aicraft body accelerations in X-direction	ms^{-2}
A_Y	Aicraft body accelerations in Y-direction	ms^{-2}
A_Z	Aicraft body accelerations in Z-direction	ms^{-2}
b	Wing span	m
c	Quarter-chord of the wing	m
$\hat{C_D}$	Estimate of the drag force coefficient	-

C_{D_0}	Drag force coefficient at α = 0	-
C_{D_α}	Derivative of the drag force coefficient with respect to α	-
$C_{D_{CT}}$	Derivative of the drag force coefficient with respect to the thrust coefficient	-
$C_{D_{\delta_e}}$	Derivative of the drag force coefficient with respect to δ_e	-
C_{D_X}	Derivative of the drag force coefficient with respect to X	-
C_L	Lift force coefficient	-
$\hat{C_L}$	Estimate of the lift force coefficient	-
C_{L_0}	Lift force coefficient at α = 0	-
C_{L_α}	Derivative of the lift force coefficient with respect to the angle of attack	-
$C_{L_\alpha^2}$	Derivative of the lift force coefficient with respect to the angle of attack squared	-
C_{l_β}	Derivative of the rolling moment coefficient with respect to the angle of sideslip	-
C_{l_p}	Derivative of the rolling moment coefficient with respect to the roll angle	-
C_m	Pitch moment coefficient	-
$\hat{C_m}$	Estimate of the pitch moment coefficient	-
C_{m_α}	Derivative of the pitch moment coefficient with respect to the angle of attack	-
$C_{m_{X,\delta_e}}$	Derivative of the pitch moment coefficient with respect to the thrust coefficient	-
$C_{m_{X,\delta_e}}$	Derivative of the pitch moment coefficient with respect to X and δ_e	-
C_{n_β}	Derivative of the yawing moment coefficient with respect to the angle of sideslip	-
f_s	Sample frequency	Hz
H_0	Gain	-
M	Mach number	-
M_{crit}	Critical Mach number	-
Q_0	Quality factor	-
q	Pitch rate	rads^{-1}
S	Wing surface area	m^2
t	Time	s
V_S	Stall speed	ms^{-1}
V_{TAS}	True Airspeed	ms^{-1}
X	Normalized flow separation point position	-

Greek Symbols

Symbol	**Description**	**Unit**

α	Angle of attack	rad
$\dot{\alpha}$	Derivative of the angle of attack with respect to time	rad
α^*	Angle of attack of the flow separation parameter X where X = 0.5	rad
α_{crit}	Critical angle of attack	rad
β	Angle of sideslip	rad
Γ	Angle of wing dihedral	rad
δ_e	Elevator deflection	rad
ζ	Set of parameters	-
Λ	Wing sweep angle at c/4	rad
λ	Taper ratio	-
τ_1	Lag time constant of the flow separation parameter X	s
τ_2	Hysteresis time constant of the flow separation parameter X	s
ω	Frequency	rads^{-1}
ω_0	Break frequency	rads^{-1}

Subscripts

0	Initial or static term

Stall Buffet Modeling using Swept Wing Flight Test Data

S. Marschalk*
Delft University of Technology, 2629 HS Delft, The Netherlands

As of April 2019, upset prevention and recovery training in flight simulation training devices is a mandatory practice for commercial and civil aircraft pilots. Aircraft stalls are a well-known upset type, therefore simulation of aircraft stall behavior is required. A key characteristic of stalls is the buffeting component, which in current stall models is still insufficiently modeled. In this research, a new methodology to more accurately model stall buffet behavior using swept wing flight test data is presented. Buffet effects occur after exceeding the critical angle of attack, with an aircraft type-specific buffet onset duration to fully develop maximum buffet intensity. The buffet transient behavior is modeled with a frequency response fit and a multivariate second-order polynomial to capture aircraft eigenmode-shape frequencies and buffet intensity respectively. Aircraft recovery and thus receding buffet effects occur at an increasing angle of attack, which is used as buffet offset. Generalization of the results was shown with the validation of data set of a straight wing aircraft, which indicates a step towards a more generic stall buffet model methodology.

Nomenclature

Roman

A_Y, A_Z	Specific forces along body axis in Y and Z direction [m/s^2]
A	Aspect ratio [-]
b	Wing span [m]
C_L	Lift coefficient [-]
c	Mean aerodynamic chord [m]
f	Frequency [Hz]
f_s	Sample frequency [Hz]
H	Transfer Function
K	Gain [-]
k_{shift}	Shifting factor
m	Mass [kg]
S	Wing surface area [m^2]
V_{TAS}	True airspeed [m/s]
Q	Quality factor [-]
X	Flow separation point [-]

Greek

α	Angle of attack [rad]
$\dot{\alpha}$	Rate of change in angle of attack [rad/s]
γ	Standard deviation
Λ	Wing sweep angle at c/4 [-]
$\hat{\zeta}$	Parameter estimates
σ	Parameter standard deviation
σ^2	Parameter variance
ω	Frequency [rad/s]

*MSc student, Control and Simulation Division, Faculty of Aerospace Engineering, Kluyverweg 1, 2629HS, Delft, The Netherlands

I. Introduction

The buffet is the aerodynamic excitation due to flow separation causing pressure fluctuations over the wing, which induces aircraft structural vibrations known as buffeting [1, 2]. Buffeting occurs at high angles of attack or high Mach numbers and negatively affect aircraft aerodynamic performance. In-flight buffeting affect aircraft handling qualities and causes structural damage, which could induce structural fatigue if sustained over an extended period of time [3]. Therefore, aircraft manufactures determine buffet characteristics and envelopes in the early design stage [4, 5].

In early studies on aircraft buffet, 2D wing models were used in wind-tunnel experiments to determine buffet effects at a certain combination of Mach number, Reynolds number and angle of attack [6–8]. These 2D wing models used strain gauges to measure the wing root bending moments, where compliance was shown by correlation of results to flight test data. Research into the transonic flight envelope led to the prediction of buffet onset and maximum buffet load using pressure measurements [1]. A combination of Computational Fluid Dynamics (CFD) calculations and wind-tunnel test led to increased accuracy of buffet characteristics, such as buffet intensity and buffet onset [4, 9]. In an experimental wind-tunnel setup multiple buffet onset prediction indicators were defined and compared with each other [10]. These buffet onset indicators are the Root Mean Square (RMS) signal variations of root strain gauges, RMS signal variations of wingtip accelerations measured with accelerometers, lift curve slope reduction, pitch moment break, axial force break and trailing edge pressure divergence [3]. The pitching moment break and lift curve slope break method proved to be inadequate to determine buffet onset when validated using flight test data [3, 11]. Additionally, a buffet intensity parameter was defined using strain gauge responses and wind tunnel ambient unsteadiness, to determine the influence of aircraft characteristic on buffeting behavior [12]. A less commonly used parameter defined buffet intensity using the total damping, wingtip accelerations, and generalized mass [13]. Buffet intensity was categorized in light, medium and heavy buffeting. when validated with flight test data. In a more recent study, fractional change transformations to determine the buffet flight envelope for a generic transport aircraft in the conceptual design stage using the aircraft wing geometries as input. Although proven adequate, the approach required a generic reference buffet onset curve or a seed aircraft with a known buffet onset curve [14].

A leading cause of aircraft accidents and incidents in commercial and civil aviation over the last decade is Loss of Control-Inflight (LOC-I) [15–17]. Therefore, mitigation of LOC-I occurrences has become a priority. Near-term mitigation solutions focus on aircraft loss of control prevention as well as aircraft recovery training, commonly referred to as Upset Prevention and Recovery Training (UPRT) [18–20]. Well-known and recurrent types of upset conditions which lead to LOC-I are aircraft stalls [21, 22]. As of April 2019, regulatory frameworks make UPRT mandatory for aircraft pilots for pilot training in Flight Simulation Training Devices (FSTD) [21, 23]. UPRT requires accurate stall models, to simulate aircraft stall behavior in FSTD.

A key characteristic of a stall is the buffet, as buffeting is an initial cue for pilots which indicates entering of the unsafe part of the flight envelope. The European SUPRA project produced enhanced aerodynamic models, based on a combination of wind-tunnel data and CFD results, for simulator environments including cueing solutions providing better and realistic buffet feedback [24]. Buffet frequency was modeled according to three structural modes and intensity was gradually increased with the angle of attack. Buffet onset was defined as exceeding the critical angle of attack, varying with Mach number. An approach to model buffet using flight test data has been used in [25] which is based on Kirchoff's theory on flow separation. Buffet onset is modeled by exceeding a fixed X-parameter threshold, whereas the frequency was identified using power spectral density analysis of the acceleration measurements. Lastly, the intensity was modeled using the X-parameter and a fixed gain. A common deficiency, which remains in current aircraft stall models is the insufficient haptic feedback of buffeting felt by pilots in stalled conditions when flying in an FSTD [26, 27].

The main contribution of this paper is a new methodology for modeling the stall buffet component using swept wing flight test data from a medium-sized transport aircraft, namely the Fokker 100. A robust and generalized methodology was proven when validated using flight test data of a straight wing business jet aircraft, namely the Cessna Citation II. However, the generalization of the methodology is dependent on the availability of type-specific aircraft parameters identified from the flight test data. In the upcoming section, an introduction on the flight test data acquisition vehicle is presented. Secondly, the third section covers the stall buffet modeling methodology. Thereafter, the results of the methodology are discussed and lastly, the final section concludes the presented research.

II. Flight Test Data Acquisition Vehicle

The flight test data acquisition vehicle in this research is the Fokker 100 aircraft. The Fokker 100 is a regional jet with twin rear fuselage-mounted engines and a T-tail configuration used for short to medium range type of operations.

Figure 1 depicts a schematic overview of the Fokker 100, which also includes the defined body-axis reference system.

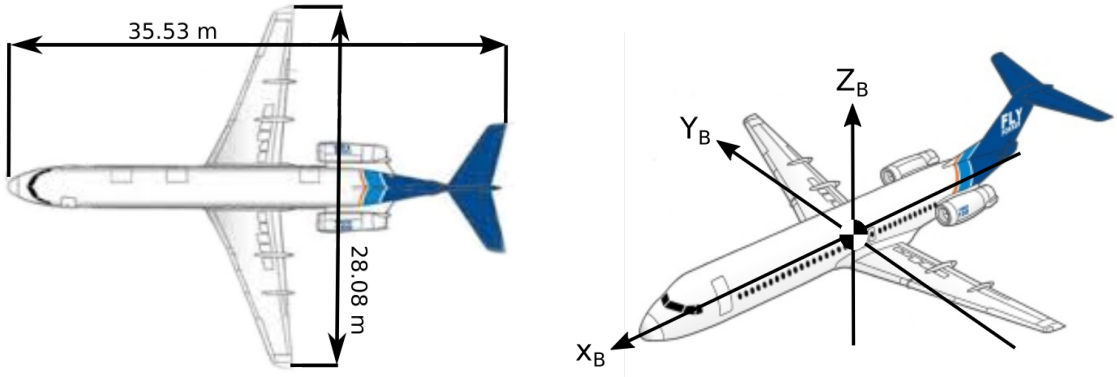

Fig. 1 A schematic overview of the Fokker 100 dimensions and the body reference frame axes definition.

The aircraft was equipped with a flight test instrumentation system, which logged the sensor measurements in a Flight Test Data Processing System (FDVS) database. A subsystem of the flight test instrumentation system used these sensor measurements to perform real-time calculations. An overview of relevant flight test instrumentation systems in this research is presented next.

A. Flight Test Instrumentation

In this research two flight data instrumentation subsystems which provide sensor measurements are used. The two flight data instrumentation subsystems are the Air Data System (ADS) and the Inertial Reference System (IRS). Additionally, an in-flight mass measurement was provided by the Flight Management System (FMS).

The ADS system consists of four subsystems, which are the pitot-static systems, angle of attack vanes, temperature probes and the Air Data Computers (ADC). The IRS entails three subsystems, which are two Inertial Reference Systems, Mode Select Unit (MSU) and an Inertial System Display Unit (ISDU). Static and pitot pressure is supplied to various instruments and systems including the ADC by three independent pitot-static systems, which consist of three pitot tubes and three static ports. Both angle of attack vanes, provide the angle of attack information to the stall prevention systems, ADC and the Automatic Flight Control and Augmentation System (AFCAS). Each ADC converts input signals from the angle of attack sensors, pitot-static system, outside air temperature probes and Altimeter Set Panel (ASP) into electrical signals, which are supplied to other various systems such as the AFCAS and IRS. Attitude and navigation information is supplied by the IRS. The IRS measures body-specific forces and body axis rotational rates, which are combined with the V_{TAS} measurements of the ADC to increase airspeed accuracy. The IRS instrumentation system was located close to the center of gravity. IRS output signals provide information to various flight and navigation systems, including the Flight Management System (FMS). All relevant measured parameters and the respective update frequencies and measures of accuracy can be found in Table 1.

Table 1 Parameters measured by ADS and AHS.

Symbol	f_s	σ^2	Source
α	16 Hz	$2.81 \cdot 10^{-6}$ rad	Left α vane
α	16 Hz	$2.32 \cdot 10^{-6}$ rad	Right α vane
A_Y	50 Hz	$8.27 \cdot 10^{-4}$ m/s^2	IRS
A_Z	50 Hz	$4.10 \cdot 10^{-3}$ m/s^2	IRS
V_{TAS}	8 Hz	$8.76 \cdot 10^{-2}$ m/s	ADC 1
V_{TAS}	8 Hz	$9.13 \cdot 10^{-2}$ m/s	ADC 2
m	40 Hz	$9.60 \cdot 10^{2}$ kg	FMS 1
m	40 Hz	$9.60 \cdot 10^{2}$ kg	FMS 2

B. Flight Test Maneuvers

As part of regulatory compliance Fokker conducted flight certification test to acquire stall certification data. Stall maneuvers were conducted according to JAR 25.201 and JAR 25.203. JAR stall maneuvers have to be conducted in both straight flight and 30 degrees banked turns, with power off and with the power necessary to maintain 1.6 V_S, where

V_S is the stall speed with flaps in approach configuration, gear retracted and maximum landing weight. Additionally, compliance is also shown in any combination of aircraft configuration i.e. all possible positions combinations of deceleration devices, flaps and landing gear, with representative weights within the certification range. In this research, only stall maneuvers in straight flight, i.e. wings-level, in clean and landing configuration are considered. A wings-level stall maneuver is initiated at an airspeed sufficiently above the stall speed, to ensure a steady deceleration rate of one knot per second until the aircraft is stalled or aircraft control reaches a stop. Normal recovery procedures are initiated by either the pilot or the stick pusher when acceptable stall behavior is noticeable or detected. Stall behavior is considered acceptable when the pilot has a clear and distinctive indication that the aircraft has entered a stall condition. Acceptable stall indications are a not immediately controllable nose-down pitching moment, which may be accompanied by a simultaneously not immediately controllable rolling motion, severe buffeting effects in terms of magnitude and severity that are strong and effective deterrents to further speed reduction, or a not immediately controllable significant roll in or out turn for dynamic stalls.

Prior to the JAR flight certification tests, Fokker also conducted stall maneuvers resembling JAR stalls in straight and turning flights. These stall maneuvers are characterized as idling stalls. A similar approach to the JAR flights was conducted, where the power levers were set to idling and the aircraft was trimmed at an airspeed within 1.2 V_S - 1.4 V_S prior to the stall. Approximate zero control inputs prior to the stall were applied to the rudder and ailerons, whereas a longitudinal control input on the elevator, prior to the stall, was applied to ensure the constant speed reduction of approximately 1 kts/s. All stall maneuvers were also flown in any likely combination of aircraft configurations. Normal recovery procedures were initiated when stalled conditions were perceived by the pilots or detected by the stall identification system, i.e. stick pusher.

A total of 190 flight recordings were used to model the buffet model in two different flight conditions, namely the clean and landing aircraft configuration. A distinction in clean and landing was made as buffet effects are dependent on flight conditions, maneuvers, and aeroelastic aircraft characteristics [28]. A clean aircraft configuration is defined as the landing gear in the 'UP' position with flaps zero. A landing configuration is defined as landing gear in the 'DOWN' position with flaps maximum. A total of 92 recordings were flown in clean configuration, the remaining 88 recordings were therefore flown in landing configuration. In Figure 2 the flight envelope in terms of angle of attack and Mach number and pressure altitude and true airspeed is shown for both aircraft configurations, where the black dots indicate the training recordings and the red dots the validation recordings.

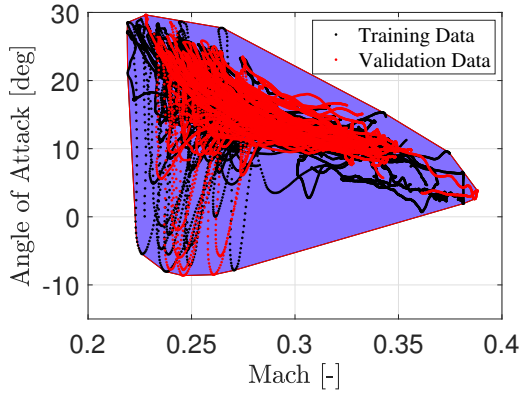

(a) Flight envelope in terms of Mach number and angle of attack in the clean configuration.

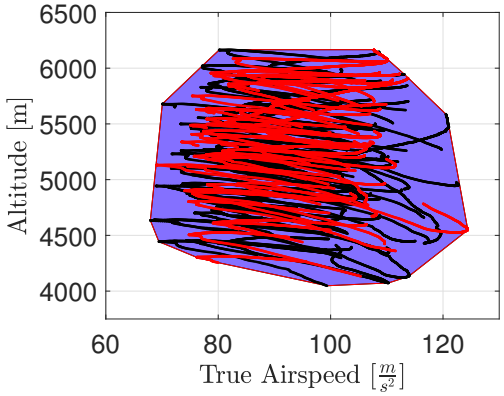

(b) Flight envelope in terms of true airspeed and altitude in the clean configuration.

In the clean configuration, a valid buffet model is identified for angles of attack ranging from 10 degrees to 27 degrees, altitudes ranging from 4.200 meters to 6.100 meters, Mach numbers ranging from Mach 0.23 to Mach 0.37 or true airspeeds ranging from 70 m/s to 110 m/s. In the landing configuration the validity of the buffet model shifts to angles of attack ranging from 5 degrees to 25 degrees, altitudes ranging from 4.000 meters to 6.200 meters, Mach numbers ranging from Mach 0.19 to Mach 0.28 or true airspeeds ranging from 60 m/s to 85 m/s. To model the buffet, a flight data recording separation of 60% and 40% was used, i.e. 60% of the data is used for model training purposes and 40% for model validation purposes.

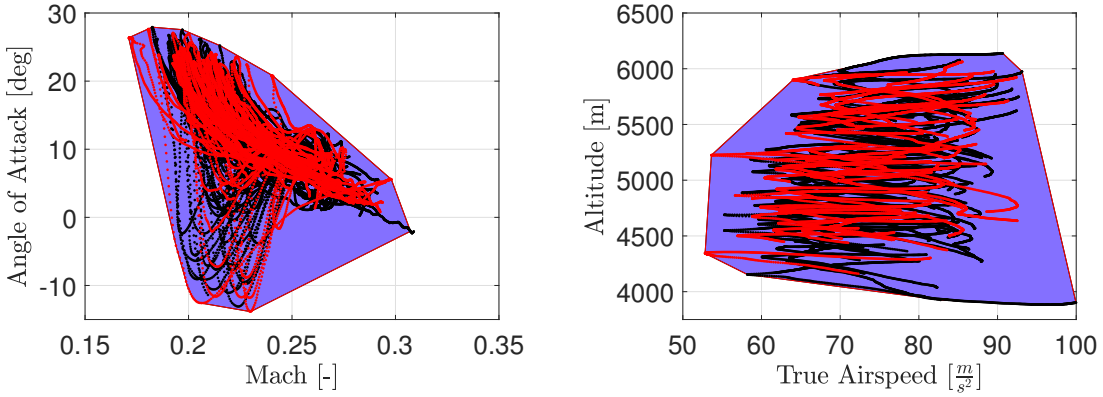

(c) Flight envelope in terms of Mach number and angle of attack in the landing configuration.

(d) Flight envelope in terms of true airspeed and altitude in the landing configuration.

Fig. 2 Flight envelopes for the Fokker 100 in terms of Mach number, angle of attack, true airspeed, and altitude in the clean and landing configuration.

C. Flight Test Data Pre- and Post-processing

An overview with relevant measured parameters for this research can be found in Table 1. A total of two additional, not readily available parameters are required, which are the lift coefficient C_L and the rate of change in the angle of attack $\dot{\alpha}$. Both parameters are however calculated in the subsystem of the flight test instrumentation. All measured parameters are filtered using a zero-order hold, low pass filter, which is a fourth-order Butterworth filter. The cut-off frequency is set at 1.5 Hertz, to remove the vibrations due to the stall buffet. A cut-off frequency of 1.5 Hertz is sufficient as buffet peak frequencies are higher than 2 Hertz, as can be seen in Figure 3. However, the cut-off frequency is a specific frequency for the Fokker 100 as buffet characteristics are aircraft dependent. A different cut-off frequency was used for the Cessna Citation II aircraft [25]. After filtering, a re-sampling procedure is required as sensor measurements had different sample frequencies and inconsistent recording lengths. All filtered parameters are re-sampled with a sampling frequency of 16 Hertz to comply with the calculations of Fokker. The re-sampled parameters α, V_{TAS} and m are averaged for each flight recording. A stall entry rate or deceleration rate is defined and calculated as the linear slope from the stall speed to an airspeed ten percent above the stall speed. Lastly, the filtered and re-sampled accelerations, in the vertical or the lateral direction, are defined as the baseline accelerations, which are part of the buffet model to simulate the vibrations of the buffet.

III. Methodology

The entire buffet model consists of four separate models, one for each combination of clean and landing configuration and lateral and vertical acceleration, which all use the same underlying methodology. First of all, the buffet onset and offset points, i.e. the activation and deactivation of the buffet model, are determined. Secondly, the transient buffet behavior is modeled, which determines the frequency and the intensity of the buffet. A frequency response fit in combination with a gain scheduling procedure using a multivariate polynomial form the basis of each separate buffet model. Lastly, the buffet models are added to the respective baseline accelerations in the respective configuration to represent the vibrations of the buffet.

A. Buffet On- and Offset Modeling

A common stall modeling technique for buffet onset and offset conditions is exceeding a fixed parameter threshold. In the SUPRA model exceeding the critical angle of attack determines the onset and offset conditions for the buffet [24]. In the work of van Horssen, the buffet onset and offset conditions are modeled according to Kirchoff's X-parameter, where the buffet (de-)activation threshold was set at $X = 0.89$ [25]. However, modeling the buffet onset and offset using

Kirchoff's X-parameter resulted in an unsatisfactory buffet (de)-activation for the Fokker 100, as the buffet onset and offset occurred at incorrect times, due to the fixed X-parameter.

In this research, the buffet onset is modeled based on exceeding the angle of attack at the maximum lift coefficient. Exceeding the angle of attack at maximum lift coefficient will change the slope in the $C_L - \alpha$ curve from positive to negative, thus the change in the sign is the activation for the buffet onset. Calculation of the slope of the $C_L - \alpha$ curve is based on a weighted, moving average function in the form of:

$$(C_{L_\alpha})_j = \frac{1}{\mathbf{w}} \frac{\Delta C_{L_j}}{\Delta \alpha_j} \tag{1}$$

where C_{L_j} and α_j are the weighted average at point j and $\mathbf{w}$ is the sum of the weighting functions. C_{L_j} and α_j are calculated using Equation 2:

$$\Delta P_j = \sum_{n=j-k_{shift}}^{n=j+k_{shift}} w_n \cdot [P(n) - P(n-1)] \text{ where } P = \{C_L, \alpha\} \tag{2}$$

where k_{shift} determines the window size of the weighted function and w_n is the respective weighted value at point n. The window size and weighted values were set according to Fokker 100 calculations. The window for the weighted average uses past and future data points, which makes it currently unusable for real-time applications. Removing future data points would make it suitable for real-time applications, however, would also decrease the smoothing accuracy. A weighted, moving average function was used to smooth the measurement data to reduce noise and artifacts present in the data set. In addition to the smoothing function, an additional constraint is set, which is a minimal angle of attack at which buffet occurs. For the Fokker 100, the angle of attack, for the buffet model to be activated, has to exceed 17.5 degrees.

A similar approach is used to determine the buffet offset, i.e. when aircraft is recovered and buffeting ends. Buffet effects end when the angle of attack increases, thus the buffet offset is set at an increasing angle of attack. However, depending on the severity and duration of the stall maneuver, the buffet offset varies with the angle of attack. Therefore, a positive rate of $\dot{\alpha}$ would suffice as the buffet offset. However, as flow attaches at lower angles of attack compared to flow separation an additional constraint was set. A change in sign of $\dot{\alpha}$ in combination with an angle of attack below 15 degrees is used as the buffet offset point. A first-order derivative of the angle of attack is calculated using a similar approach as for the buffet onset, namely a weighted moving average function.

B. Buffet Transient Modeling

1. Frequency Response Fit

A main characteristic of the buffet is captured in the frequency of the induced structural vibrations. The IRS in the Fokker 100 captures the structural vibrations by measuring the body accelerations, which are transformed into the frequency domain by applying a Fourier transform. A periodogram is obtained from the Fourier transform of the accelerations, which is the best possible estimate of a Power Spectral Density (PSD). An increase in accuracy is achieved by averaging multiple realizations for each periodogram. A periodogram for the accelerations measured at the IRS in the lateral and vertical direction for the clean configuration is shown in Figure 3.

The periodogram in the longitudinal direction is omitted from this research as the intensity in the longitudinal direction is effectively zero. Figure 3 indicates a higher intensity in the vertical direction due to the 10^{th} order of magnitude difference, indicating that the buffet in the vertical direction is the strongest. A total of four peak frequencies in the lateral direction are identified, and a total of three peak frequencies in the vertical direction are identified. A buffet model frequency response fit is based on the identified peak frequencies in each direction, which is given by the following PSD relation:

$$S_{yy} = |H(j\omega)|^2 S_{uu} \tag{3}$$

The shaping filter $H(j\omega)$ is used to model the buffet peak frequencies and a white noise input signal with an intensity equal to one is assumed. The shaping filter consists of a combination of several second-order bandpass filters:

$$H(j\omega) = \sum_{i=1}^{n} H_i(j\omega) = \sum_{i=1}^{n} \frac{K_i \frac{\omega_i}{Q_i} j\omega}{(j\omega_i)^2 + \frac{\omega_i}{Q_i} j\omega + \omega_i^2} \tag{4}$$

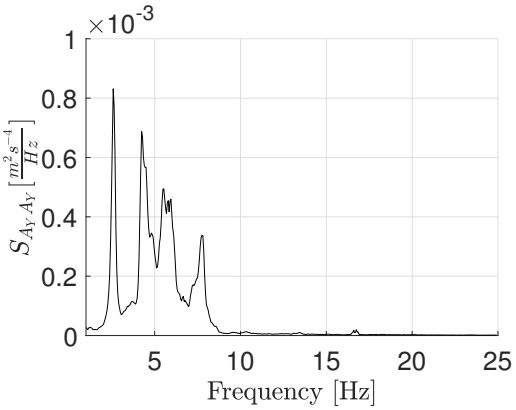

(a) Periodogram of the IRS acceleration measurements in lateral direction in the clean configuration.

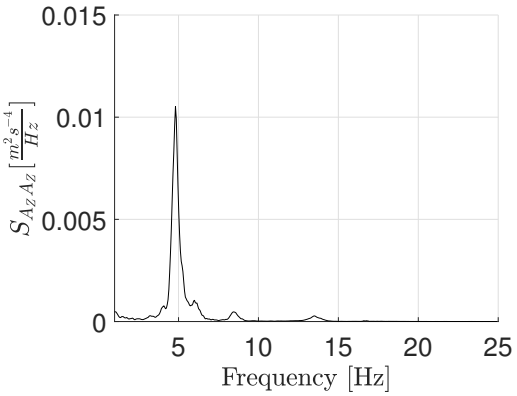

(b) Periodogram of the IRS acceleration measurements in vertical direction in the clean configuration.

Fig. 3 Periodogram in lateral and vertical direction in clean configuration.

where n is the number of bandpass filters equal to the number identified peak frequencies. A nonlinear least-squares method determines each shaping filter parameter. In `MATLAB` the function `nonlinsq` was used where the number of iterations, functions evaluations, and the Levenberg-Marquardt algorithm was set. An iterative outer loop calls the `nonlinsq` function to maximize the R^2 value, whereas the `nonlinsq` function minimizes the Mean Squared Error (MSE).

2. Buffet Intensity

Although buffet effects are present at buffet onset, the data showed that buffeting intensity scaled up gradually, to a certain maximum. In this research, the maximum buffet intensity is defined and reached when the accelerations are within the 95% confidence interval. The buffet model is modeled as a shaping filter with white noise input. To ensure the correct model output, a Gain $\hat{K}$ is multiplied to the frequency response output, which ensures the correct maximum buffet intensity is reached. This gain is calculated with $K = \frac{A_i}{2\sigma}$, where A_i is the acceleration in the lateral or vertical $i = Y, Z$ direction and 2σ is 95% confidence interval of the modeled buffet. The standard deviation for the buffet model is calculated using the time domain history:

$$\sigma_y = \sqrt{\frac{1}{N-1}\sum_{i=1}^{N}(y[i] - \mu_y)^2} \tag{5}$$

where the number of samples is large enough to ensure the best estimate of the standard deviation. Due to the complexity of the integral of the shaping filter, an analytical solution for the standard is not calculated.

Additionally, a buffet onset transient time is defined as the duration in seconds from buffet onset to the maximum buffet intensity, using the maximum buffet intensity definition as described above. An average buffet onset transient time is calculated for each buffet model, where the buffet onset transient time is the median of all recordings. Lastly, the buffet onset transient behavior, defined as the duration from buffet onset to maximum buffeting, is assumed to be quadratic based on the flight data and literature [28].

C. Complete Fokker 100 Buffet Model

The combination of buffet onset and offset, buffet frequency and intensity are captured in the buffet model and the buffet is modeled according to Equation 6:

$$A_{i,mod} = A_{i,filt} + K_i \cdot A_{i,buffet} \tag{6}$$

where $A_{i,mod}$ is the model output in terms of the acceleration in lateral or vertical direction ($i = Y, Z$), $A_{i,filt}$ is the baseline acceleration in either direction, K_i is the gain determined with a multivariate polynomial and $A_{i,buffet}$ is the frequency response of the buffet. The buffet characteristics are entailed in $K_i \cdot A_{i,buffet}$, where K_i determines the intensity of the buffet and $A_{i,buffet}$ the aircraft type-specific buffeting frequencies. Buffet effects are dependent on flight conditions, maneuvers, and aircraft aeroelastic characteristics. The buffet intensity and frequency in a flight condition also depend on the angle of attack, control surface deflections and dynamic pressure [29]. In this research, the Gain is determined using a multivariate polynomial using linear regression and ordinary least squares parameter estimation. The model input parameters to determine the Gain are set as h (as the altitude influences q), q, q/W (as the buffet intensity and frequency scale with q, whereas W accounts for the aeroelastic characteristics [28]), α and dV/dt (an increase in the deceleration rate, causes a more abrupt stall, which increases the duration of the stall and the intensity based on the flight test data). Each input is determined at the angle of attack where the lift coefficient is maximum as this was found to be the buffet onset point. A combination of two input parameters is then iteratively tested using polynomials of degree d, ranging from zero to five. Usually, lower-order degrees would suffice to fit the scattered data, as an increase would not significantly increase model parameters estimates, whereas it could induce overfitting. The domain of these polynomials is determined by rectangular grids using the minimum and maximum values of the input data. A best fit for each of the four buffet models is achieved at the lowest Root Mean Squared Error (RMSE) value in combination with the largest Coefficient of Determination (R^2) value.

As buffet characteristics are entailed in the K_i and $A_{i,buffet}$, tuning these parameters would yield a buffet model for other aircraft. In this research, data of the Cessna Citation is used to determine if a generalization of the buffet model is possible. The Cessna Citation II is a straight wing, twinjet business jet aircraft, which characteristics differ substantially compared to the Fokker 100.

IV. Results

The buffet model was identified with a data set containing 92 recordings in the clean configuration and a data set containing 89 recordings in the landing configuration. A model training set and model validation set were chosen arbitrary, with a 60% - 40 % split, in each configuration. In the first section, the results for the Fokker 100 buffet model are presented. Secondly, the model quality of the buffet model is assessed and lastly, model validation is conducted using flight test data of the Cessna Citation II.

A. Fokker 100 Buffet Model

1. Flight Envelope

In the clean configuration, a total of 92 recordings are available, where a total of 54 recordings are used for training purposes and the remaining 38 are used for validation purposes, which roughly is a 60-40 split. A flight envelope in terms of angle of attack and deceleration rate yielded the best results as inputs for the gain scheduling in clean configuration. In Figure 4 the flight envelope for the clean configuration is shown for both input terms, where the blue crosses indicate the points used for training and the black with red dots indicate the validation points. A flight envelope is given for the angles of attack and for the deceleration rate. An underpopulated regime in this flight envelope is at low angles of attack and high deceleration rates and at high angles of attack and low deceleration rates.

For the buffet models in the landing configuration, a total of 88 recordings are available. From these 88 recordings, 52 are used for training and the remaining 36 are used for validation purposes, which is also roughly a 60-40 split. A most suitable fit was achieved with a flight envelope in terms of pressure altitude and dynamic pressure over weight, which can be seen in Figure 4. In this flight envelope, an underpopulated regime can be found at low altitudes in combination with a high values for dynamic pressure over weight.

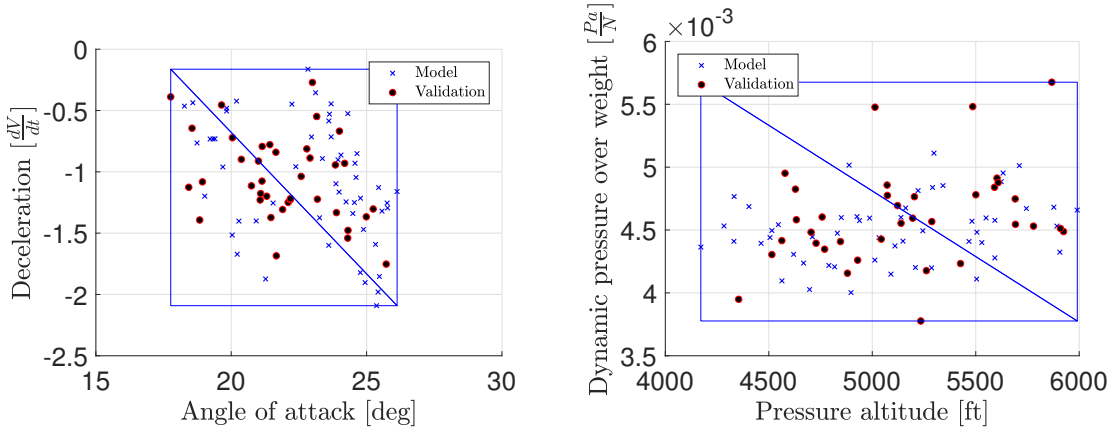

(a) Flight envelope in clean configuration in terms of angle of attack and deceleration rate.

(b) Flight envelope in landing configuration in terms of altitude and dynamic pressure over weight.

Fig. 4 Flight envelope in clean and landing configuration

2. On- and Offset Conditions

Buffet onset- and offset condition were identified separately in both directions, however, buffet onset and offset yielded similar results as can be identified from Figure 5. Figure 5 only shows the buffet onset and offset in clean configuration, however, similar results were found for the landing configuration.

The buffet onset transient behavior, defined as the duration from buffet onset to maximum buffeting, was also calculated separately for all four buffet models. A median onset transient for accelerations in the lateral direction in the clean configuration is set at 0.70s, whereas the median onset duration in the vertical direction in the clean configuration is 0.88s. The median onset duration in landing configuration is set at 1.56s in the lateral direction and 1.75s in the vertical direction. The buffet onset duration in landing configuration in either direction is approximate twice the buffet onset duration in clean configuration.

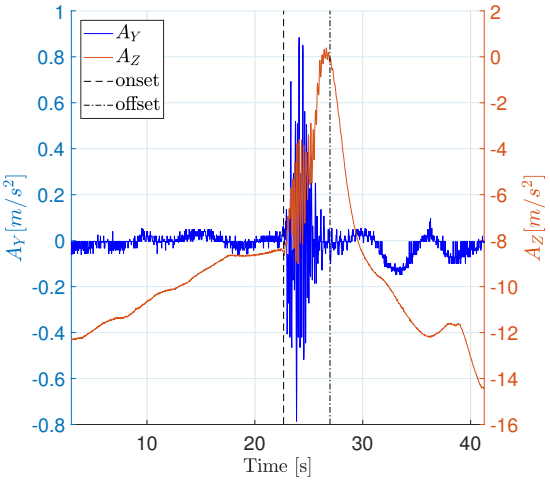

Fig. 5 Measured accelerations in lateral and vertical direction including buffet onset and offset in clean configuration.

Although similar recordings are used to calculate the buffet onset duration a difference in onset duration in the lateral and vertical direction is calculated. As normality of the onset transient time could not be assumed, a Wilcoxon signed-rank test is used to determine similarity in distributions for both populations. However, the null hypothesis was rejected, indicating that the onset time in the lateral direction and vertical direction do not come from a similar distribution. Therefore, the onset duration was set independently in each direction.

3. Frequency Response Fit

The frequency response fit in the lateral and vertical direction in the clean configuration are shown in Figure 6. The intensity of the vertical accelerations is approximately ten times larger than the intensity of the lateral accelerations, which indicates that accelerations in the vertical direction are most dominant in a stall. In the lateral direction, the four identified peak frequencies are located at 2.60 Hz, 4.40 Hz, 5.65 Hz and 7.62 Hz, whereas the three peak frequencies in

the vertical direction are located at 4.80 Hz, 8.46 Hz and 13.37 Hz. In Table 2 the results for each parameter can be found. The Root Mean Square Error (RMSE) for the model in lateral direction is $5.9670{\cdot}10^{-5}$ $\frac{m^2/s^4}{Hz}$, the relative Root Mean Square Error (RMS_{rel}) is 38.24%, whereas the coefficient of determination (R^2) equals 0.8162. The RMS in vertical direction is $1.6719{\cdot}10^{-4}$ $\frac{m^2/s^4}{Hz}$, the RMS_{rel} is 13.61%, whereas the R^2 equals 0.9800. The low Cramer-Rao lower bounds from Table 2 in combination with the low RMSE values and high value for the R^2 indicates an adequate fit for the frequency response fit in both directions.

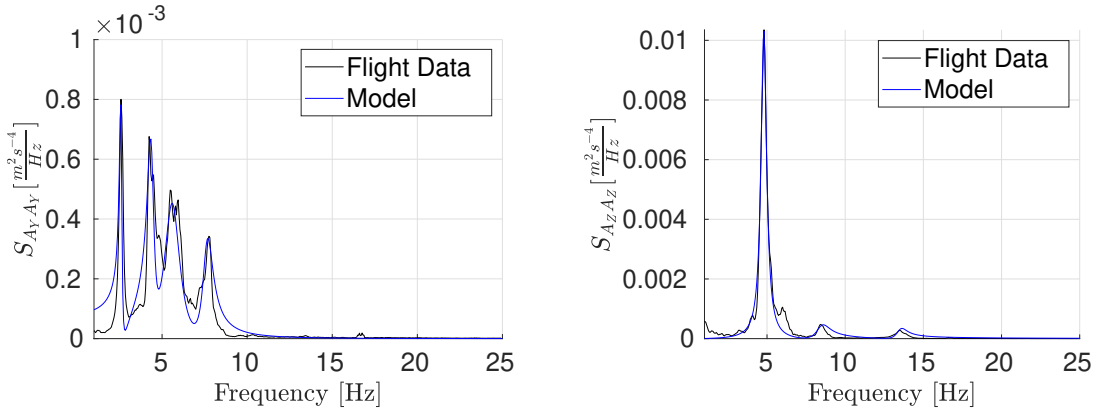

(a) Frequency response fit over 54 recordings for the lateral IRS acceleration measurements in the clean configuration.

(b) Frequency response fit over 54 recordings for the vertical IRS acceleration measurements in the clean configuration.

Fig. 6 Frequency response fit over 54 recordings for the lateral and vertical IRS acceleration measurements in the clean configuration.

Figure 7 shows the frequency response fit for the accelerations in the lateral and vertical direction in the landing direction. In the landing configuration, the intensity in the vertical direction is also approximately ten times larger when compared to the intensity in the lateral direction, thus the stall is also most dominant in the vertical direction. A total of four peak frequencies in the lateral direction are located at 2.60 Hz, 4.26 Hz, 5.89 Hz and 7.62 Hz, thus setting N in Equation 3 to four. In the vertical direction, N is set to three as there are three peak frequencies at 4.89 Hz, 8.53 Hz and 13.51 Hz. All results of the iterative, nonlinear least squares method for both frequency responses can be found in Table 3. The RMSE for the frequency response fit in lateral direction in landing configuration is $1.4486{\cdot}10^{\mathbf{-4}}$ $\frac{m^2/s^4}{Hz}$, the $RMSE_{rel}$ is 38.14%, whereas the R^2 equals 0.8296 The RMSE for the fit in vertical direction in landing configuration is $1.5544{\cdot}10^{\mathbf{-4}}$ $\frac{m^2/s^4}{Hz}$, the $RMSE_{rel}$ is 17.77%, whereas the R^2 equals 0.9645. Also in the landing configuration, the low Cramer-Rao lower bounds and RMSE values in combination with a high value for the R^2 indicates a good frequency response fit for both directions.

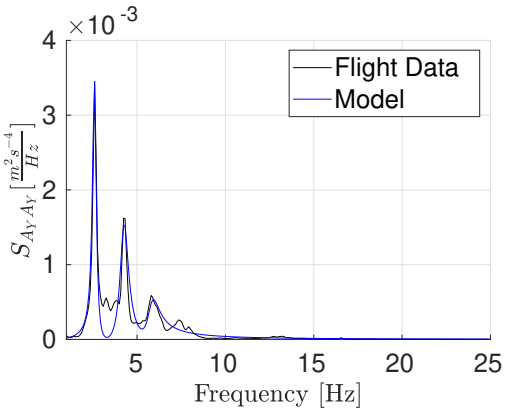

(a) Frequency response fit over 52 recordings for the lateral IRS acceleration measurements in the landing configuration.

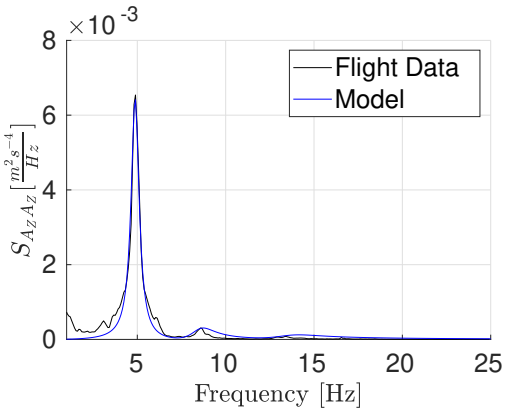

(b) Frequency response fit over 52 recordings for the vertical IRS acceleration measurements in the landing configuration.

Fig. 7 Frequency response fit over 52 recordings for the lateral and vertical IRS acceleration measurements in the landing configuration.

Table 2 Parameter estimates for the frequency response function in the lateral and vertical direction in the clean configuration.

		Lateral direction			Vertical direction		
		$\hat{\zeta}$	$\sigma(\hat{\zeta})$	$\frac{\sigma(\hat{\zeta})]}{\hat{\zeta}} \cdot 100$	$\hat{\zeta}$	$\sigma(\hat{\zeta})$	$\frac{\sigma(\hat{\zeta})]}{\hat{\zeta}} \cdot 100$
K_1	[-]	0.00159	$1.5080 \cdot 10^{-4}$	9.4974	0.10141	$8.5484 \cdot 10^{-4}$	0.8430
ω_1	[rad/s]	16.3326	$7.4838 \cdot 10^{-3}$	0.0458	30.1651	$1.7625 \cdot 10^{-2}$	0.0584
Q_1	[-]	15.0121	$1.4137 \cdot 10^{-3}$	0.0094	11.1269	$1.7369 \cdot 10^{-3}$	0.0156
K_2	[-]	0.00201	$3.7879 \cdot 10^{-4}$	18.814	0.01923	$7.1283 \cdot 10^{-4}$	3.7077
ω_2	[rad/s]	27.6503	$7.0717 \cdot 10^{-2}$	0.2558	53.1809	$2.5656 \cdot 10^{-1}$	0.4824
Q_2	[-]	9.17651	$7.8483 \cdot 10^{-3}$	0.0855	7.82235	$1.3992 \cdot 10^{-2}$	0.1789
K_3	[-]	0.00417	$2.3332 \cdot 10^{-4}$	5.5888	0.01320	$3.7902 \cdot 10^{-4}$	2.8709
ω_3	[rad/s]	35.4808	$9.6524 \cdot 10^{-2}$	0.2720	83.9878	$4.0341 \cdot 10^{-1}$	0.4803
Q_3	[-]	4.78712	$9.4047 \cdot 10^{-3}$	0.1965	13.5702	$9.4468 \cdot 10^{-3}$	0.0696
K_4	[-]	0.00151	$1.5996 \cdot 10^{-4}$	10.572			
ω_4	[rad/s]	47.9013	$6.4145 \cdot 10^{-2}$	0.1339			
Q_4	[-]	4.78712	$4.0835 \cdot 10^{-3}$	0.0401			

Table 3 Parameter estimates for the frequency response function in the lateral and vertical direction in the landing configuration.

		Lateral direction			Vertical direction		
		$\hat{\zeta}$	$\sigma(\hat{\zeta})$	$\frac{\sigma(\hat{\zeta})}{\hat{\zeta}} \cdot 100$	$\hat{\zeta}$	$\sigma(\hat{\zeta})$	$\frac{\sigma(\hat{\zeta})}{\hat{\zeta}} \cdot 100$
H_1	[-]	0.05758	$3.1835 \cdot 10^{-4}$	0.5564	0.07970	$1.3432 \cdot 10^{-3}$	1.6823
ω_1	[rad/s]	16.3337	$9.2457 \cdot 10^{-3}$	0.0568	30.7010	$5.7144 \cdot 10^{-2}$	0.1860
Q_1	[-]	10.1452	$1.5864 \cdot 10^{-3}$	0.0157	8.88653	$4.5758 \cdot 10^{-3}$	0.0515
H_2	[-]	0.03799	$1.6819 \cdot 10^{-3}$	4.5236	0.01478	$4.7843 \cdot 10^{-4}$	3.2280
ω_2	[rad/s]	26.7751	$1.7212 \cdot 10^{-1}$	0.6438	53.6058	$3.6428 \cdot 10^{-1}$	0.6835
Q_2	[-]	7.18551	$1.9449 \cdot 10^{-2}$	0.2723	5.14542	$2.2158 \cdot 10^{-2}$	0.4340
H_3	[-]	0.01696	$4.4032 \cdot 10^{-4}$	1.9170	0.00736	$1.5068 \cdot 10^{-4}$	2.0323
ω_3	[rad/s]	37.0136	$1.4573 \cdot 10^{-1}$	0.3943	84.7993	$4.6090 \cdot 10^{-1}$	0.5439
Q_3	[-]	7.32298	$1.1963 \cdot 10^{-2}$	0.2245	4.29687	$1.8046 \cdot 10^{-2}$	0.4207
H_4	[-]	0.00120	$1.6003 \cdot 10^{-4}$	13.278			
ω_4	[rad/s]	47.9320	$6.4154 \cdot 10^{-2}$	0.1339			
Q_4	[-]	0.13121	$4.1020 \cdot 10^{-3}$	3.1121			

4. Multivariate Polynomial Results

Figure 4 shows the flight envelopes which yielded the best results for the multivariate polynomials. In the clean configuration, the flight envelope is given by the angle of attack and the deceleration rate whereas for the landing configuration the flight envelope is given by the pressure altitude and dynamic pressure over weight. A second-order polynomial for all four models yielded the best results. An overview of the goodness-of-fit parameters is shown in 4b.

Table 4 Goodness-of-fit for the second-order polynomial in the clean and landing configuration.

(a) Goodness-of-fit for the second-order polynomial in the landing configuration.

		Lateral direction	Vertical direction
RMSE	[-]	1.709	2.051
RMSE_{rel}	[%]	15.55	14.98
R^2	[-]	0.621	0.642

(b) Goodness-of-fit for the second-order polynomial in the clean configuration.

		Lateral direction	Vertical direction
RMSE	[-]	2.158	3.476
RMSE_{rel}	[%]	24.06	24.05
R^2	[-]	0.572	0.572

The goodness-of-fit parameters RMSE_{rel} and R^2 in either configuration yield similar results, which indicates a similar gain proportion in either direction, due to buffet intensity per recording. Although the RMSE and relative RMSE has low values, the R^2 value is also rather low, which indicates that the model output does not entirely represent the buffet intensity. A low value for the R^2 is due to the scarceness of the data points in some regions of the flight envelope.

Lastly, one time series for the measured accelerations including the buffet models for each combination of configuration and direction are shown in Figure 8 and Figure 9. In each subfigure, the blue lines indicate the measured flight test data, whereas the red lines are the model output based on Equation 6. The subfigures in the left column show an entire flight recording, whereas the recordings on the right zoom in on the buffet part of the flight recording.

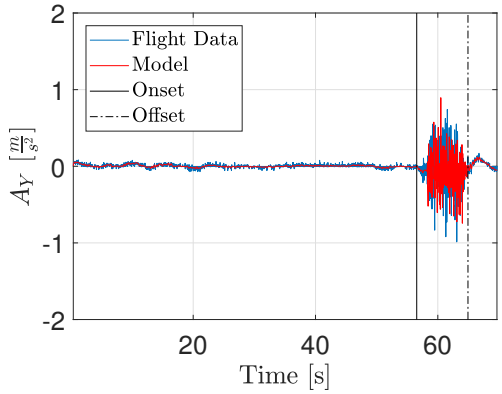

(a) Measured lateral acceleration including the lateral buffet model in the clean configuration.

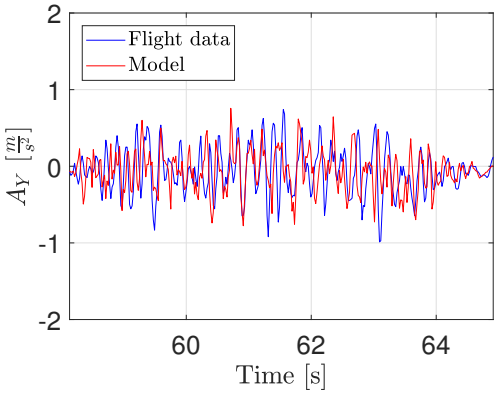

(b) Measured lateral acceleration including the lateral buffet model in the clean configuration (zoomed in on the buffet).

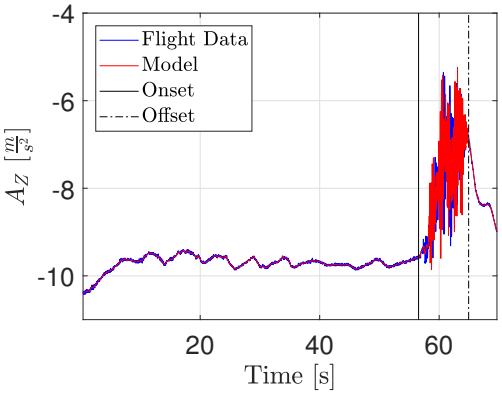

(c) Measured vertical acceleration including the vertical buffet model in the clean configuration.

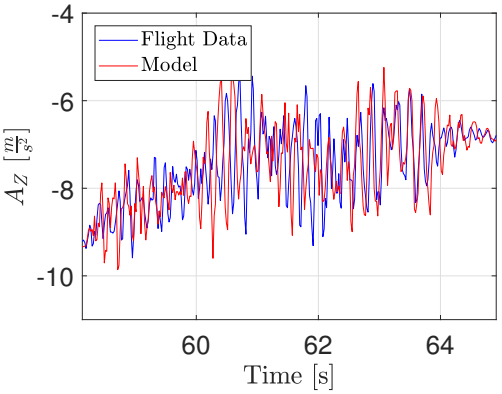

(d) Measured vertical acceleration including the vertical buffet model in the clean configuration (zoomed in on the buffet).

Fig. 8 Measured accelerations and buffet models in the lateral and vertical direction for the clean configuration.

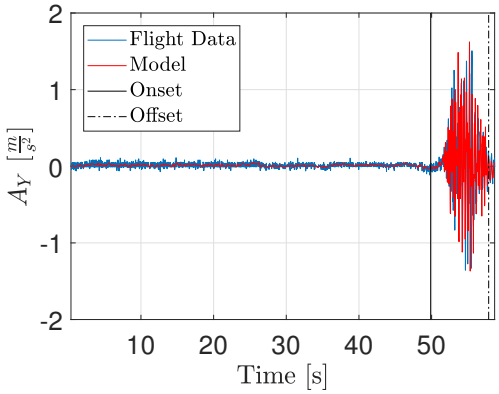

(e) Measured lateral accelerations including the lateral buffet model in the landing configuration.

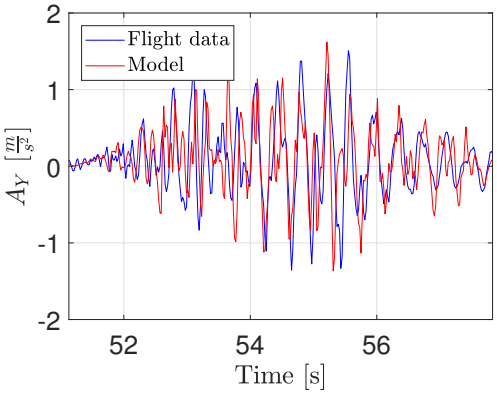

(f) Measured lateral acceleration including the lateral buffet model in the landing configuration (zoomed in on the buffet).

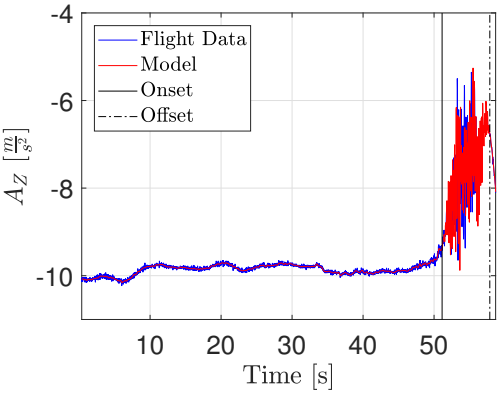

(g) Measured vertical accelerations including the vertical buffet model in the landing configuration.

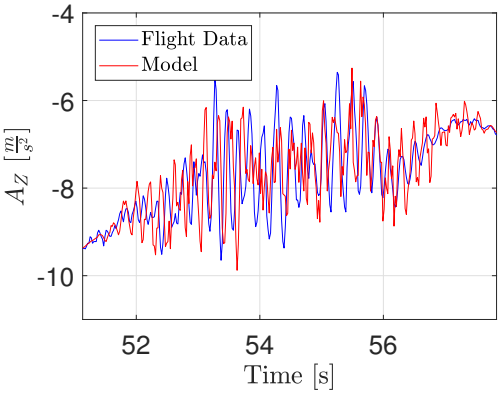

(h) Measured vertical acceleration including the vertical buffet model in the landing configuration (zoomed in on the buffet).

Fig. 9 Measured accelerations and buffet models in the lateral and vertical direction for the landing configuration.

B. Fokker 100 Buffet Model Analysis and Quality Assessment

In this section, a more in-depth analysis of the results is conducted. Additionally, the Fokker 100 model quality is assessed in terms of the goodness-of-fit parameters RMS, RMS_{rel} and R^2.

First of all, the buffet onset transient duration in each buffet model was tested for normality using the Shapiro–Wilk test and the one-sample Kolmogorov-Smirnov test. However, small p-values indicated that the hypothesis was rejected, such that normality could not be assumed. Therefore a median onset duration is defined in each of the four models. Although, similar recordings are used to determine the onset duration a difference in onset duration was calculated. Therefore, a Wilcoxon signed ranked test determined if the onset duration still came from a similar distribution. However, the hypothesis of the Wilcoxon signed-rank test was rejected, indicating that the onset duration in lateral and vertical direction does not come from similar distribution. The definition of the maximum buffet intensity could indicate why the onset duration is lower for the accelerations in the lateral direction. In the lateral direction the standard deviation are $\sigma = 0.0847$ m/s^2, $\sigma = 0.0732$ m/s^2, whereas in the vertical direction the standard deviation are $\sigma = 0.1045$ m/s^2 and $\sigma = 0.1171$ m/s^2 in the clean and landing configuration respectively. Lower values in the lateral direction could indicate

that the buffet onset duration is reached earlier. A difference in onset duration is also possible due to the separation of the flow. Flow separation for wings-level stall maneuvers usually gradually separates from the wing, inducing a turbulent airflow that may already have a stronger effect on the vertical stabilizer. Additionally, the median buffet onset time for the model in landing configuration is approximately twice as long as the buffet onset time in clean configuration. A stall in clean configuration requires thus less time to reach maximum buffet penetration when compared to a stall in the landing configuration.

Secondly, in the vertical direction in clean and landing configuration a total of three peak frequencies were identified whereas in the lateral direction four peak frequencies were identified, as can be seen in Table 3 and Table 5. An overview of all frequencies is given in Table 6. The peak frequency values are similar in their respective direction, independent of the aircraft configuration. These similarities correspond to the type-specific eigenmode shapes of the Fokker 100 aircraft. The three peak frequencies in the vertical direction are approximately located at 4.85 Hz, 8.50Hz and 13.5Hz and correspond to the fuselage vertical bending, 2^{nd} wing bending and vertical stabilizer bending respectively. In the lateral direction, these frequencies are located at 2.60 Hz, 4.30Hz, 5.75Hz and 7.62Hz, which are the asymmetrical fin bending, asymmetrical fin torsion, fuselage lateral bending and the lateral wing bending modes.

Table 5 Frequency mode-shapes for the Fokker 100.

	Clean configuration		Landing configuration	
	Lateral direction	Vertical direction	Lateral direction	Vertical direction
f_1 [Hz]	2.60	4.80	2.60	4.89
f_2 [Hz]	4.40	8.46	4.26	8.53
f_3 [Hz]	5.65	13.37	5.89	13.51
f_4 [Hz]	7.62	-	7.62	-

An overview of the goodness-of-fit parameters for the buffet model in the vertical direction and lateral direction is given in Table 6 and Table 7 respectively. In each of the four buffet models, a higher R^2 value and lower RMSE and $RMSE_{rel}$ values indicate a better fit for the frequency response compared to the polynomial fit. An increase in buffet model accuracy is likely to be achieved by increasing the accuracy of the buffet transient. The goodness-of-fit parameters indicate a better fit for the buffet models in the vertical direction in their respective configuration when compared to the buffet models in the lateral direction. A more accurate fit in the vertical direction is required as the accelerations in vertical direction were identified as most dominant in a stall. The buffet models in the landing configuration have a better fit compared to the buffet models in the clean configuration.

Table 6 Goodness-of-fit parameters for the buffet models in vertical direction.

	Clean configuration				Landing configuration			
	Frequency response fit		Polynomial fit		Frequency response fit		Polynomial fit	
RMSE	$1.6719 \cdot 10^{-4}$	$\frac{m^2/s^4}{Hz}$	3.476	-	$1.5544 \cdot 10^{-4}$	$\frac{m^2/s^4}{Hz}$	2.051	-
$RMSE_{rel}$	13.61	%	24.05	%	17.77	%	14.98	%
R^2	0.9800	-	0.572	-	0.9645	-	0.642	-

Table 7 Goodness-of-fit parameters for the buffet models in lateral direction.

	Clean configuration				Landing configuration			
	Frequency response fit		Polynomial fit		Frequency response fit		Polynomial fit	
RMSE	$5.9670 \cdot 10^{-5}$	$\frac{m^2/s^4}{Hz}$	2.158	-	$1.4486 \cdot 10^{-4}$	$\frac{m^2/s^4}{Hz}$	1.709	-
$RMSE_{rel}$	38.42	%	24.06	%	38.41	%	15.55	%
R^2	0.8162	-	0.572	-	0.8296	-	0.621	-

The total buffet model is modeled according to Equation 6, which is a white noise signal passed through a shaping filter, multiplied with a gain and added to the baseline acceleration. Although Figure 8 and Figure 9 show adequate the buffet behavior, including buffet onset and offset, using the methodology, a combination of parameters influence the model validity and model quality. First of all, the validity of each of the buffet models is given in Figure 4 in combination with the flight envelope of Figure 4. Any likely combination of input parameter for each buffet model within the valid flight envelope resulted in a positive value for the gain, indicating the gain scheduling procedure is modeled adequately. Secondly, a difference in model output and measured value might be due to the random nature of the colored noise in combination with the estimated gain and acceleration as well as the non-linearity in a stall buffet. Even so, the low RMSE values indicate that the output of the buffet model might still be within the 95% interval. Lastly, a median onset duration was used in each model, therefore the maximum buffet intensity might be reached later than the median value.

C. Model Quality Assessment using Cessna Citation II Flight Test Data

In addition to the model quality analysis of the Fokker 100 stall buffet model, another validation set is applied using the Fokker 100 stall buffet methodology. The validation set is based on the flight test data of the Cessna Citation II as described in van Horssen [25]. The data set contains a total of 69 quasi-steady stall maneuvers in clean configuration, where 54 flight recordings are used for model training and 15 flight recordings for model validation. Validation is only conducted in the clean configuration for the accelerations in the vertical direction.

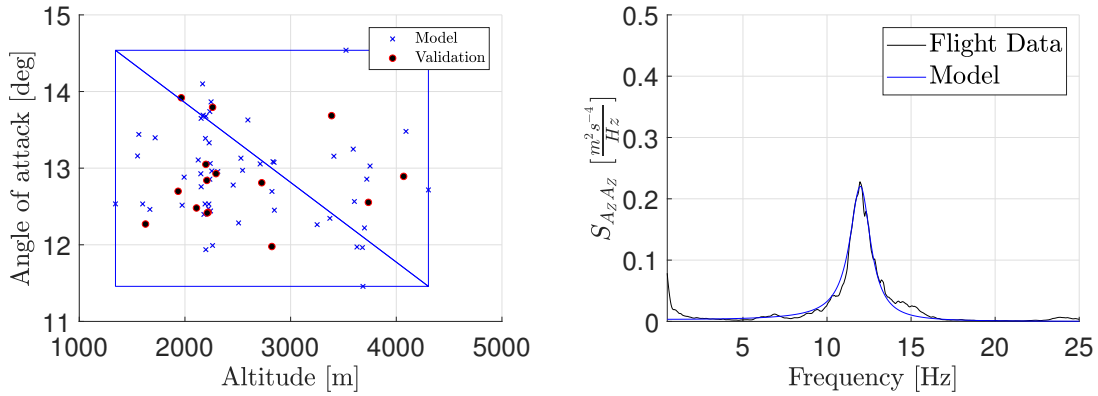

(a) Flight envelope in terms of angle of attack and altitude in the clean configuration.

(b) Frequency response fit over 54 recordings for the vertical IRS acceleration measurements in the clean configuration.

Fig. 10 Frequency response fit and flight envelope in the vertical direction in the clean configuration for the Cessna Citation II.

For the Cessna Citation, the flight envelope in the clean configuration in terms of angle of attack and altitude, shown in Figure 10, yielded the best goodness-of-fit parameters. The validity of the Cessna Citation flight envelope is at lower angles of attack and altitudes when compared to the flight envelope of the Fokker 100. The median buffet onset duration for the Cessna Citation stall maneuvers is 0.45 seconds. Buffet offset occurs at a change in the change in the sign of

$\dot{\alpha}$ in combination with exceeding the angle of attack threshold of 10 degrees. However, due to the dynamic stability of the Cessna Citation, an additional constraint for the buffet offset is required. In several stall maneuvers, two or more consecutive stalls were flown, as indicated by the increasing angle of attack after the initial stall in Figure 11. In Figure 11, buffet onset and offset occurs twice for the Cessna Citation but only once for the Fokker 100. Therefore, in addition to the current buffet offset conditions, the buffet offset was set to a different value for $\dot{\alpha}$ as long as the angle of attack is above ten degrees. In Figure 10 the frequency response fit for the vertical direction is also shown. The peak-frequency in the vertical direction is located at 12 Hertz, whereas the highest peak-frequency for the Fokker 100 is located at 4.80 Hertz, indicating a difference in structural eigenmode-shapes.

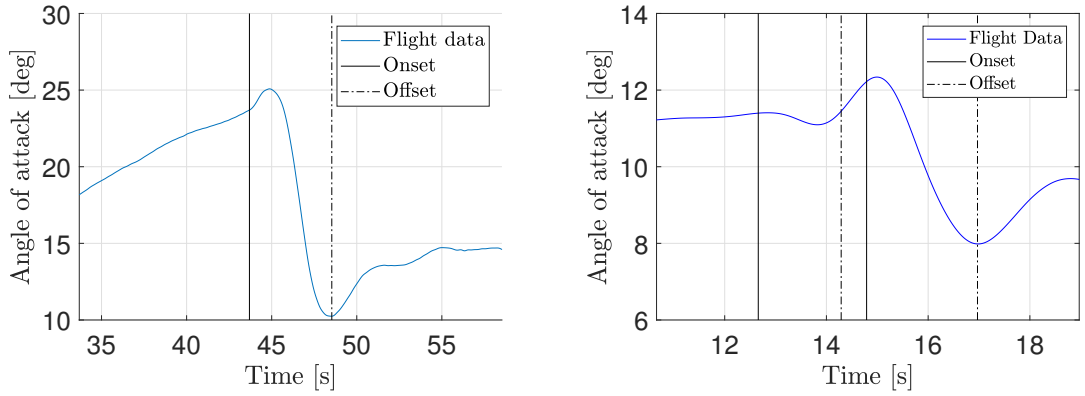

(a) Angle of attack including buffet onset and offset for the Fokker 100.

(b) Angle of attack including buffet onset and offset for the Cessna Citation II.

Fig. 11 Angle of attack including buffet onset and offset for the Fokker 100 and Cessna Citation in clean configuration.

In Table 8 the goodness-of-fit parameters are shown for the buffet model in the vertical direction and clean configuration the Fokker 100 and Cessna Citation. The frequency response fit for the Cessna Citation is adapted from the work of van Horssen [25].

Table 8 Goodness-of-fit parameters in the vertical direction in the clean configuration for the Fokker 100 and Cessna Citation II.

(a) Goodness-of-fit parameters in the vertical direction in the clean configuration for the Fokker 100.

	Frequency response fit		Polynomial fit	
RMSE	$1.6719 \cdot 10^{-4}$	$\frac{m^2/s^4}{Hz}$	3.476	-
$RMSE_{rel}$	13.61	%	24.05	%
R^2	0.9800	-	0.572	-

(b) Goodness-of-fit parameters in the vertical direction in the clean configuration for the Cessna Citation II.

	Frequency response fit		Polynomial fit	
RMSE	$1.1189 \cdot 10^{-4}$	$\frac{m^2/s^4}{Hz}$	0.2732	-
$RMSE_{rel}$	-	%	11.15	%
R^2	0.9731	-	0.6234	-

In Figure 12 the measured accelerations and buffet model in the vertical direction for the Cessna Citation are shown. In the figures the onset and offset conditions are indicated by the solid and dashed black lines. In subfigure (b) and subfigure (c) of each figure is zoomed in on the buffet model, where the window is defined from buffet onset to buffet offset.

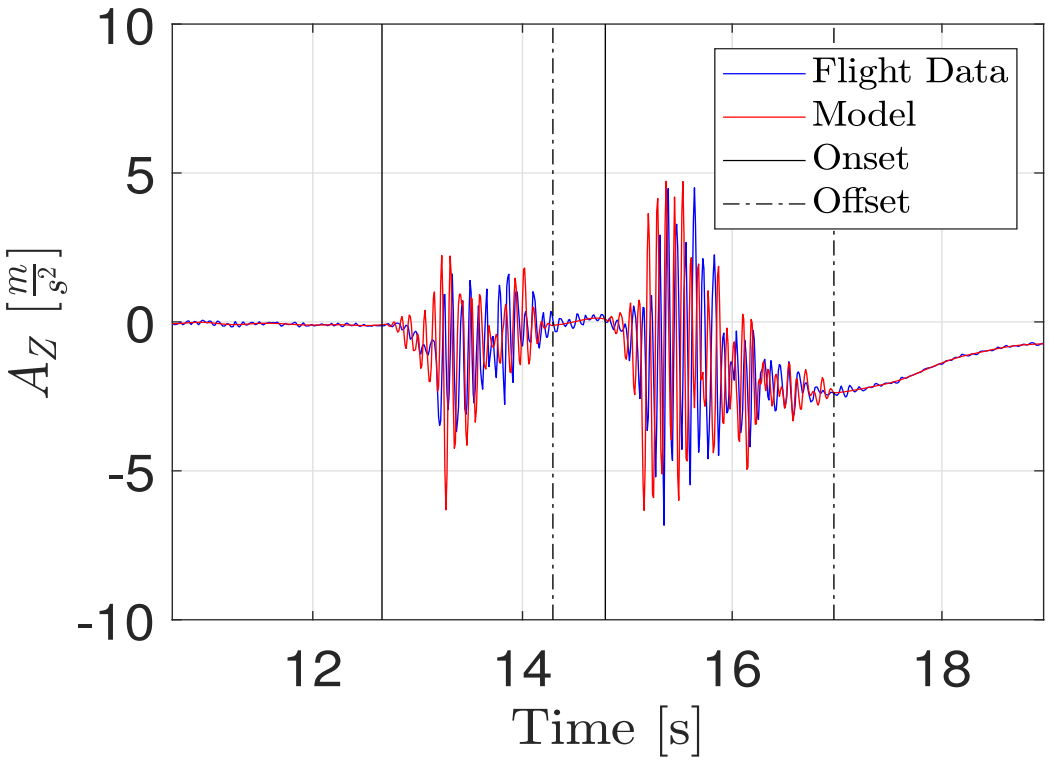

(a) Measured vertical acceleration including the vertical buffet model in clean configuration.

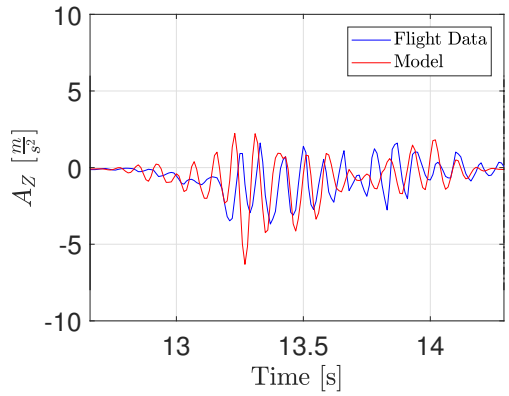

(b) Measured vertical acceleration including the vertical buffet model in the clean configuration (zoomed in on the first buffet).

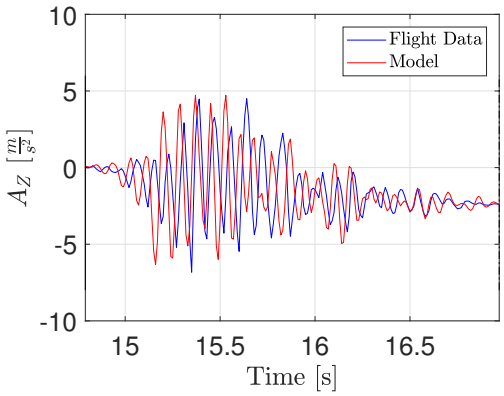

(c) Measured vertical acceleration including the vertical buffet model in the clean configuration (zoomed in on the second buffet).

Fig. 12 Measured accelerations and buffet model in the vertical direction and the clean configuration for the Cessna Citation II.

A similar frequency response fit in terms of R^2 and RMSE, a better polynomial fit in terms of R^2, RMSE, $RMSE_{rel}$, and Figure 12 indicate that the Fokker 100 stall buffet model methodology can be adapted to Cessna Citation II data and therefore generalization to another aircraft type is proven. However, the generalization of the methodology requires type-specific parameters to be available or determined from the flight test data. First of all, the flight envelopes for both

aircraft differ, which requires knowledge on the input parameters, for example, the critical angle of attack. Secondly, the buffet frequency response fit for either aircraft has to be calculated from the accelerations in the flight test data. A combination of the frequency response fit and the flight envelope also determine the values of the scheduled gains. Thirdly, the buffet onset duration has to be estimated for the different aircraft types in each direction. Lastly, the similarity in maneuvers in the flight test data should be flown. However, by setting an additional buffet offset constraint the similarity in-flight maneuver might be mitigated to some extent. However, if each of these type-specific aircraft parameters is determined, the stall buffet methodology in this research is a step towards a more generic buffet model.

V. Conclusion

In this paper, a methodology to model the stall buffet component using swept wing flight test data from a medium-sized transport aircraft, namely the Fokker 10 is presented. The stall maneuvers were flown according to JAR-25 flight certification tests. A total of four separate models were identified, one model for each combination of the clean and landing configuration and the lateral and vertical accelerations. Validation indicated adequate goodness-of-fit parameters for each of the four buffet models. An additional validation in the clean configuration in the vertical direction using straight wing flight test data was conducted. The methodology showed to be generalizable when type-specific aircraft characteristics are available. The stall buffet model output adequately represents the highly nonlinear buffeting in the flight test data.

A buffet onset point was identified from the flight data at the point where the critical angle of attack is exceeded, for angles of attack larger than 17.5 degrees. A transient onset behavior is modeled using the median time duration for the buffet to reach the maximum buffet intensity. The maximum buffet intensity is defined as the accelerations within the 95% confidence interval. The buffet onset duration was assumed to be scaled quadratically up to the maximum buffet intensity. The buffet offset point, the point where buffet effects receded, occurred at angles of attack lower than 15.0 degrees when the angle of attack started increasing again. The flight test data showed that buffet offset occurs at exceeding a zero angle of attack rate.

The buffet transient is identified by shaping a white noise signal and multiplying the signal with a gain. A combination of N second-order band-pass filters is used as shaping filters, where N is the number of identified peak frequencies from a periodogram, which represents Fokker 100 specific eigenmode-shapes. A gain scheduling procedure using a multivariate second-order polynomial estimated the buffet intensity. Adequate goodness-of-fit parameters for the frequency response fit and polynomial fit were obtained in each model.

Additional validation was conducted using straight wing flight test data from the Cessna Citation. When type-specific parameters are available, the buffet model methodology also applies to other aircraft types. In conclusion, a more generic methodology for identifying a buffet model for different aircraft is identified. The buffet model methodology could positively contribute to increased pilot awareness in flight simulation training devices as buffeting is a key characteristic of the stall. Ultimately, combining this research with concurrent research could mitigate LOC-I occurrences.

References

[1] Lemley, C. and Mullans, R., *Buffeting pressures on a swept wing in transonic flight - Comparison of model and full scale measurements*, Structures, Structural Dynamics, and Materials and Co-located Conferences, American Institute of Aeronautics and Astronautics, 1973. Doi:10.2514/6.1973-311.

[2] Caruana, D., Correge, M., Reberga, O., Despre, C. & Mignosi, A., *Buffet and buffeting active control*, Fluid Dynamics and Co-located Conferences, American Institute of Aeronautics and Astronautics, 2000. Doi:10.2514/6.2000-2609.

[3] Dang, H., and Yang, Z. , "Buffet Onset Prediction and Flow Field Around a Buffeting Airfoil at Transonic Speeds," *In 51st AIAA/ASME/ASCE/AHS/ASC Structures, Structural Dynamics, and Materials Conference: American Institute of Aeronautics and Astronautics.*, 2010. Doi:10.2514/6.2010-3051.

[4] Liguore, S. and Pitt, D., "Aircraft Buffet Prediction Using Unsteady Aerodynamic Wind Tunnel Model Six-Component Balance Data." *In 45th AIAA/ASME/ASCE/AHS/ASC Structures, Structural Dynamics & Materials Conference: American Institute of Aeronautics and Astronautics.*, 2004. Doi:10.2514/6.2004-2045.

[5] Bérard, A., Rizz, A. & Isikveren, A.T., "Development and Implementation of Aerodynamic Analysis Methods for Aircraft Conceptual Design ," *Canadian Aeronautics and Space Institute Annual General Meeting. Aircraft Design & Development Symposium.*, 2007. Retrieved on March 13, 2019, from `https://www.researchgate.net/publication/274706692_Development_and_Implementation_of_Aerodynamic_Analysis_Methods_for_Aircraft_Conceptual_Design` .

[6] Huston, W.B., Rainey, A.G. & Baker, T.F., "*A Study of the Correlation Between Flight and Wind-Tunnel Buffeting Loads*," (Technical Report NACA-RM-L55E16b)., Langley Field, VA, United States: National Advisory Committee for Aeronautics. Langley Aeronautical Lab., 1955.

[7] Skopinski, T.H. and Huston, W.B., "*A semi-empirical procedure for estimating wing buffet loads in the transonic region*," (Technical Report NACA-RM-L56E01)., Langley Field, VA, United States: National Advisory Committee for Aeronautics. Langley Aeronautical Lab., 1956.

[8] Davis, D.D., Jr and Wornom, D.E., "*Buffet Tests of an Attack-airplane Model with Emphasis on Analysis of Data from Wind-tunnel Tests*," (Technical Report NACA-RM-L57H13)., Langley Field, VA, United States: National Advisory Committee for Aeronautics. Langley Aeronautical Lab., 1957.

[9] Brunet, V., *Computational Study of Buffet Phenomenon with Unsteady RANS Equations*, Fluid Dynamics and Co-located Conferences, American Institute of Aeronautics and Astronautics, 2003. Doi:10.2514/6.2003-3679.

[10] Lawson, S., Greenwell, D & Quinn, M.K., *Characterisation of Buffet on a Civil Aircraft Wing*, AIAA SciTech Forum, American Institute of Aeronautics and Astronautics, 2016. Doi:10.2514/6.2016-1309.

[11] van Eijndhoven, J.N.A., "Buffet envelope prediction of transport aircraft during the conceptual design phase: Predict transonic, shock induced buffet onset," Master's thesis, Delft University of Technology, 2012.

[12] Mabey, D., "Some aspects of aircraft dynamic loads due to flow separation," *Progress in Aerospace Sciences*, Vol. 26, No. 2, 1989, pp. 115–151. Https://doi.org/10.1016/0376-0421(89)90006-7.

[13] Mabey, D., "Review of the normal force fluctuations on aerofoils with separated flow," *Progress in Aerospace Sciences*, Vol. 29, No. 1, 1992, pp. 43–80. Https://doi.org/10.1016/0376-0421(92)90003-Z.

[14] Bérard, A. and Isikveren, A.T., "Conceptual Design Prediction of the Buffet Envelope of Transport Aircraft," *Journal of Aircraft*, Vol. 46, No. 5, 2009, pp. 1593–1606. Doi: 10.2514/1.41367.

[15] Boeing, "Statistical Summary of Commercial Jet Airplane Accidents," , 2016.

[16] Airbus S.A.S., "A Statistical Analysis of Commercial Aviation Accidents 1958-2017," , 2017.

[17] International Civil Aviation Organization, "2018 Safety Report," , 2018.

[18] International Air Transport Association, "Loss of Control In-Flight Accident Analysis Report," , 2015.

[19] Jacboson, S.R., "*Aircraft Loss of Control Causal Factors and Mitigation Challenges*," (Technical Report DFRC-E-DAA-TN1949)., Edwards, CA, United States: NASA Dryden Flight Research Center, 2010.

[20] Crider, D.A., *Need for Upset Recovery Training*, Guidance, Navigation, and Control and Co-located Conferences, American Institute of Aeronautics and Astronautics, 2008. Doi:10.2514/6.2008-6864.

[21] European Aviation Safety Agency, "Opinion No 06/2017," , 2017. Retrieved on October 2, 2018, from `https://www.easa.europa.eu/sites/default/files/dfu/Opinion%20No%2006-2017.pdf` .

[22] Federal Aviation Administration, "120-109A - Stall Prevention and Recovery Training with Change 1," , 2017. Retrieved on October 2, 2018, from `https://www.faa.gov/documentLibrary/media/Advisory_Circular/AC_120-109A_CHG_1.pdf` .

[23] Federal Aviation Administration, "AC 120-111 - Upset Prevention and Recovery Training - with Change," , 2017. Retrieved on October 2, 2018, from `https://www.faa.gov/documentLibrary/media/Advisory_Circular/AC_120-111_CHG_1.pdf` .

[24] Abramov, N.B., Goman, M.G., Khrabrov, A.N., Kolesnikov, E.N., and Fucke, L., Soemarwoto, B. & Smaili, H., *Pushing Ahead - SUPRA Airplane Model for Upset Recovery*, Guidance, Navigation, and Control and Co-located Conferences, American Institute of Aeronautics and Astronautics, 2012.

[25] van Horssen, L.J., de Visser, C.C. & Pool, D.M., "Aerodynamic Stall and Buffet Modeling for the Cessna Citation II Based on Flight Test Data," *In 2018 AIAA Modeling and Simulation Technologies Conference: American Institute of Aeronautics and Astronautics.*, 2018. Doi: 10.2514/6.2018-1167.

[26] Advani, S. and Field, J., "Upset Prevention and Recovery Training in Flight Simulators," *In AIAA Modeling and Simulation Technologies Conference: American Institute of Aeronautics and Astronautics*, 2011. Doi:10.2514/6.2011-6698.

[27] Schroeder, J.A., Burki-Cohen, J.S., Shikany, D., Gingras, D.R., & Desrochers, P.P. , "An Evaluation of Several Stall Models for Commercial Transport Training," *In AIAA Modeling and Simulation Technologies Conference: American Institute of Aeronautics and Astronautics.*, 2014. doi:10.2514/6.2014-1002.

[28] Courtland, D.P., *Stability and Control: Flight Testing*, 2nd ed., Pergamon, The Boulevard, Langford Lane, Kidlington ,Oxford, 2014.

[29] Danowsky, B.P. and Schulze, P.C., *Control Surface Buffet Load Measurement using Aircraft Actuators*, AIAA SciTech Forum, American Institute of Aeronautics and Astronautics, 2016. Doi:10.2514/6.2016-2005.

Chapter 1

Introduction

Over the last decade mitigation of Loss of Control-Inflight became a priority as Loss of Control-Inflight (LOC-I) is a leading cause of aircraft accidents and incidents in commercial and civil aviation [1–4]. LOC-I is defined by the CAST/ICAO Common Taxonomy Team (CICTT) [5] as: "Loss of control in-flight is an extreme manifestation of a deviation from its intended flight path". Well-known and recurrent types of upset conditions which lead to LOC-I are aircraft stalls [6,7]. It is therefore that near-term mitigation solutions focus on aircraft loss of control prevention as well as aircraft recovery training, commonly referred to as Upset Prevention and Recovery Training (UPRT) [8–10]. The American Federal Aviation Administration (FAA) and the European Aviation Safety Agency (EASA) both created regulatory frameworks which come into force in 2019 and make UPRT mandatory for pilots in both Flight Simulation Training Devices (FSTD) and aircraft [6,11].

As part of LOC-I mitigation in UPRT, a proposition by the International Committee for Aviation Training in Extended Envelopes (ICATEE) was made and divides mitigation strategies into four main areas of interest [12]. Although UPRT entails a vast majority of different training aspects, the work in this plan will focus on aircraft stalls only. Creating awareness is the first step towards stall mitigation in UPRT. The second and third area focuses on preventing upset conditions by recognizing conditions leading to a stall and subsequently avoiding these conditions. If however upset conditions lead to a stall, the final step is to safely recover the aircraft from a stalled condition. Training exercises in UPRT are mainly conducted in FSTD which focus on approach-to-stall and stall exercises as stall related incidents are the most recurrent factors in LOC-I situations [6,7]. An important indicator for pilots in events before and in a stall is the so-called buffeting, which is the aircraft induced structural vibrations felt throughout the aircraft [13,14]. Buffeting effects are imposed when flow separation occurs.

A common deficiency in current aircraft stall models is the insufficient haptic feedback of buffeting felt by pilots in stalled conditions when flying in a simulator [12, 15, 16]. In this research, a plan is proposed to negate the current deficiencies in aircraft stall models. The buffet model proposed in [17,18] will serve as a starting position, where adapting and updating the model using current state-of-the-art stall modeling techniques as well as flight test data of the Fokker 100 will lead to an improved buffet model. Additionally, another main aspect of the research is to identify the influences of sweep angle on the buffet model. Lastly, the improved model shall be implemented in the Delft University Aircraft Simulation Model and Analysis Tool (DASMAT) which could be used in the SIMONA Research Simulator.

As a practical relevance, the identified buffet model will contribute to the field of flight simulator UPRT and will help increase model fidelity. An increase in model fidelity leads to increased pilot awareness and avoids negative training which increases UPRT effectiveness. Increasing training effectiveness mitigates LOC-I occurrences and will ultimately increase aviation safety.

Research Objective

As stated above two main goals of this work are creating an improved buffet model in the stall-regime as well as identifying sweep angle effects on the buffet model for the Fokker 100. Concurrent research on aerodynamic stall modeling for the Fokker 100 will be combined with this research and will provide the university with a stall flight envelope of the Fokker 100. The Fokker 100 stall model could be used as a starting position in new studies to develop a generalized stall model. Therefore,

Research Objective

The research objective is to identify, validate and verify a stall buffet model for a swept wing aircraft namely the Fokker 100 by adapting and testing current state-of-the-art stall modeling techniques on flight data of the Fokker 100.

The research objective will be divided into several sub-goals which will help contribute to the research objective. These sub-goals are defined as:

- *Perform a literature study on the aircraft dynamics during and after aerodynamic stall and the methods proposed to model these dynamics;*
- *Determine the (statistical) quality of available flight test data and identify the parameters required to model buffet effects;*
- *Gather flight test data for the Cessna Citation to mimic dynamic and static stall manoeuvres comparable to the flight test data of the Fokker 100;*
- *Determine aircraft dynamics during and after aerodynamic stall based on a literature study as well as the influences of Fokker 100 characteristics, e.g. swept wings or a T-tail configuration;*
- *Determine the current state-of-the-art stall modeling techniques and its requirements;*
- *Estimate aircraft states and aerodynamic parameters with its appropriate techniques;*
- *Test and adapt current modeling techniques to obtain a buffet model for the Fokker 100;*
- *Validate and verify the model with the flight test data of the Cessna Citation and Fokker 100;*
- *Implement the new stall model in a new DASMAT framework;*
- *Make recommendations and conclusions based on the performed work.*

Research Question

The research questions was formulated as;

Research Question

Which current state-of-the-art stall modeling techniques would identify an accurate buffet model in vertical direction for a swept wing aircraft including onset and transient behaviour using flight test data?

In order to answer the main research question a division into several sub-questions was made. These sub-questions are formulated as follows:

- *Which current state-of-the-art stall modeling techniques are suitable to model buffet characteristics with flight test data?*
- *How do Fokker 100 aircraft characteristics influence the stall behaviour and how does this stall behaviour compare to the Cessna Citation?*
- *What types of stall manoeuvres are available in the flight test database of the Fokker 100 and are suitable to model the buffet characteristics?*

Project Outline & Methodology

Achieving the research objective which is to identify, validate and verify the buffet model for the Fokker 100 requires several steps to be conducted. Most of these steps can be derived from the sub-goals presented above and can be found here.

Step 1

During the first step, an in-depth literature study is performed based on previous advances in stall and buffet modeling, which helps to create a clear overview in current stall and buffet modeling techniques. It will provide the starting position for this research. Additionally, a company visit to Desdemona is scheduled to gain more insight into industry-related aspects of stall modeling. In chapter 2 all aspects of the literature study and company visit can be found.

Step 2

Familiarization with the Fokker 100 database is the second step. It will help to provide a more clear overview of what kind of data is available in the database and what kind of data is used for buffet modeling purposes. In this step flight tests with the Cessna Citation shall be scheduled, in which data is acquired similarly to that of the Fokker 100 stall maneuvers. The similarity in the data helps to identify the influence of sweep on the buffet. Details on the data in the Fokker 100 database can be found in chapter 3.

Step 3

In the third step, the flight test data of the Fokker 100 is applied to the current buffet model found in the literature. Familiarization with the current buffet model is improved by conducting a test flight in the SIMONA Research Simulator to test the buffet. In combination with the test flight in the Cessna Citation helps to better understand the current deficiencies of stall models in simulators. Applying the Fokker 100 data to the current buffet model also entails the steps of pre-processing the data, selecting the model structure and estimating the parameters, for which the preliminary results are given in chapter 4. In this step also some validation and verification of the results are given.

Step 4

This step entails the body of this current research. An iterative procedure is used to update and alter the current buffet model in the vertical direction. A more accurate buffet model is given when the onset and transient behavior of the model is appropriately modeled, i.e. it starts and stops at appropriate times. Secondly, an improvement on the validation and verification of the results is created. And lastly, a comparison to the buffet model of the Cessna Citation shall be made. However, this is not part of this preliminary research.

Step 5

The final step is to implement the new buffet model in the DASMAT environment and test it using the SIMONA Research Simulator. However, this is also not covered in the preliminary research.

Chapter 2

Literature Study

This chapter covers a broad background on stall modeling and a more in depth analysis on stall buffet. First of all, past and current advances in stall modeling are discussed, thereafter stall and stall dynamics are entailed. Lastly, the aircraft buffet is discussed.

2.1 Background on Stall Modeling

Although high angle of attack modeling is fairly new for commercial aircraft, military applications in the high angle of attack regime were already available [19–22]. These military applications were mainly based on wind-tunnel experiments in which static and dynamic tests were conducted. National Aeronautics and Space Administration (NASA) also conducted experiments with fighter aircraft to gain insight in aircraft maneuverability, aerodynamics, handling qualities and control laws at high angles of attack [23, 24]. The data and results were later used as validation for Computational Fluid Dynamics (CFD) computations and wind tunnel experiments [25]. NASA developed a type-specific model based on a commercial transport aircraft which modeled the aerodynamics at high angles of attack [26,27]. Pilot evaluations for these models showed improved fidelity compared to a baseline model, even though buffet indications as well as asymmetric roll response was not representative for an actual aircraft.

In Europe, the Simulation of Upset Recovery in Aviation (SUPRA) project provided solutions for simulators environments, which include enhanced aerodynamic models as well as improved cueing solutions to provide a more realistic buffet feedback [28]. A combination of wind-tunnel data and CFD results were used in these extensive modeling techniques. Evaluation and verification based on Subject Matter Experts (SME) indicated the usefulness of these model in full stall recovery training [29]. It was found that buffet onset in simulators, currently set at a difference of $\pm 0.5g$, was found to be insufficient and should be lowered to an onset angle of attack of $\pm 0.03g$. Additionally, the buffet intensity (amplitude) was varied as a function of angle of attack.

At the University of Toronto Institute for Aerospace Studies (UTIAS) a representative model in the post-stall regime for T-tailed regional jets and turboprops was developed [30–32] using aircraft manufacturer data and static wind-tunnel tests. The methodology is based on the addition of aerodynamic increments on the existing aerodynamic flight envelope to construct a model at high angles of attack, which was extended to other aircraft using a geometry-based method.

In most of the papers, the main focus is modeling aerodynamic stall behavior in the stall and post-stall regime, whereas testing model fidelity is usually excluded. An increase in model fidelity leads to effective training and decreases negative training. A study by Schroeder et al. [15], evaluated several stall models based on SME, where the SME concluded that the buffet components of these stall models feel nothing like actual buffeting of a stalled aircraft. Another way of testing model fidelity was by including surprise elements in training procedures. Training procedures which include surprise elements resemble actual stalls in an aircraft better. Another study used a type-representative stall model without using

flight test data and was found to be an acceptable and suitable training procedure for pilots to properly recover in stalled conditions in various flight phases [33]. Lastly, a recent study [34] on model fidelity of full flight recovery training used a t-tail turboprop as a baseline and altered this baseline into three different models to observe a noticeable difference in each model. Lateral conditions such as roll-off were indicated as insufficient by the SME. Despite proper training instructions, improper stall recovery procedures were still initiated by several pilots, which indicates the current (incorrect) skill-based behavior.

The regulations which come into force in 2019 require adequate aerodynamic models mainly in the post-stall regime, however, the current regulations require a representative aircraft model in the stall regime, which is sufficient for training purposes. Full stall training is sufficient with representative models because modeling of stall maneuvers poses difficulties as stall recordings have unstable time histories and obtaining stall flight test data for commercial aircraft is expensive [34]. Compliance for FSTD is thus shown by adequate modeling of aerodynamics, which requires the devices to recover a fully stalled aircraft or modeling of aircraft at high angles of attack which exceed the critical angle of attack up to ten degrees [34]. Although several studies adequately modeled longitudinal aerodynamics, lateral dynamics still lack accurate modeling or are even excluded in studies [17, 18, 32, 35]. It is therefore that most models are not yet adequately modeled to represent aircraft behavior in this form, and therefore additional research is still required.

2.2 Aerodynamic Stall

Aerodynamic stall is the condition where the airflow over wings starts to separate which occurs at high angles of attack or high Mach numbers [36]. Airflow separation may occur at any given point on the aircraft however, it is assumed to be at the wings only as the wings are the main generation of lift. Additionally, any point of flow separation is considered rare [37]. An aircraft in a stalled condition is characterized by two major and sudden effects, namely a decrease in lift and an increase in (pressure) drag. At low Mach numbers flow separation occurs after exceeding a certain angle of attack called the critical angle of attack (α_{crit}). In Figure 2.1 a typical lift curve is drawn, which includes the sudden decrease of the lift coefficient when exceeding the critical angle of attack. At higher Mach numbers flow is usually separated due to occurrence of shock waves. Flow separation may occur at any given flight condition and is, therefore, an important aspect in aircraft design.

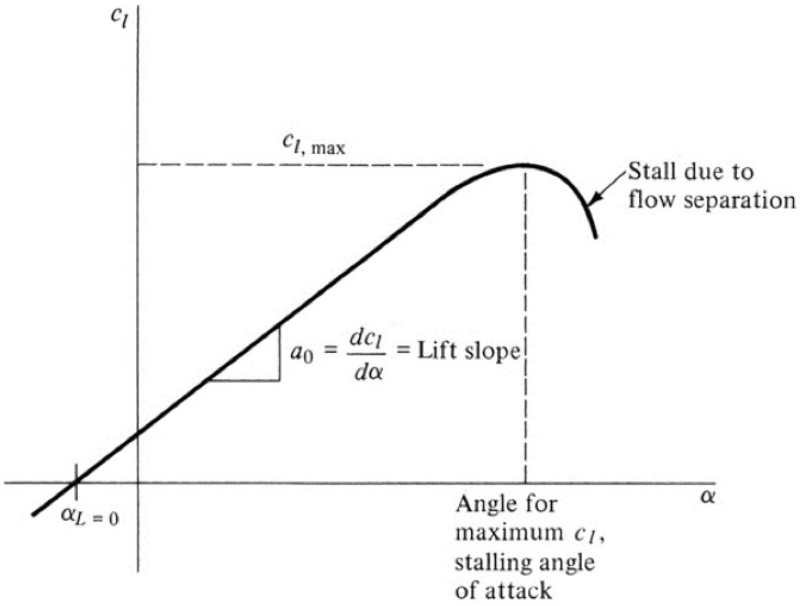

Figure 2.1: Sketch of a typical lift curve. From "Introduction to Flight" (7^{th} ed., p. 301), by J.D. Anderson Jr., 2012.

At subsonic airspeeds flow separation may be categorized into three different types, namely trailing edge stall, leading-edge stall, and thin airfoil stall. The geometric airfoil shape influences the type of

flow separation and these properties are mainly defined by airfoil thickness, camber, and nose radius [38]. A trailing edge stall is characterized by flow separation starting at the trailing edge and gradually moving forward when the angle of attack is increased. This type of flow separation is characterized by thick airfoils with a large nose radius. A leading-edge stall is a quite abrupt stall at the leading edge and causes flow separation over the entire airfoil, which is characterized by airfoils with a moderate leading-edge radius. Lastly, the thin airfoil stall is when a long separation bubble develops with increasing angle of attack when finally separating the flow over the entire airfoil [39].

In the transonic flow, regime flow is separated due to shock waves when the local Mach number on the wing exceeds Mach one. The transonic flow regime is excluded from this research as the Fokker 100 is a transport aircraft which generally fly below Mach one and the certification flight test do not include stalls at high Mach numbers.

2.2.1 Influences on Aerodynamic Stall

Aerodynamic stall is directly related to the critical angle of attack and the airspeed at which stall occurs is called the stall speed. At the stall speed, the aircraft is just able to maintain level flight. However, the stall speed differs per aircraft configuration and flight condition, which are discussed in more detail below.

Aircraft Configuration

At the stall speed, the aircraft just maintains level flight which indicates the lift and thrust equal the drag and weight. A way to decrease the stall speed is to increase the lift using high-lift devices. The Fokker 100 is equipped with double-slotted flaps which act as high-lift devices when extended. The flaps increase the lift by increasing the effective camber of the airfoil and simultaneously slightly decreasing the critical angle of attack. Slats are another form of commonly used high-lift device, however, the Fokker 100 is not equipped with slats as the leading edge is fixed.

A wing plan form parameter influencing the stall behavior is the (quarter-chord) sweep angle. The sweep angle (Λ) is defined as the angle between the lateral axis perpendicular to the aircraft centerline and the quarter chord line as can be seen in Figure 2.2.

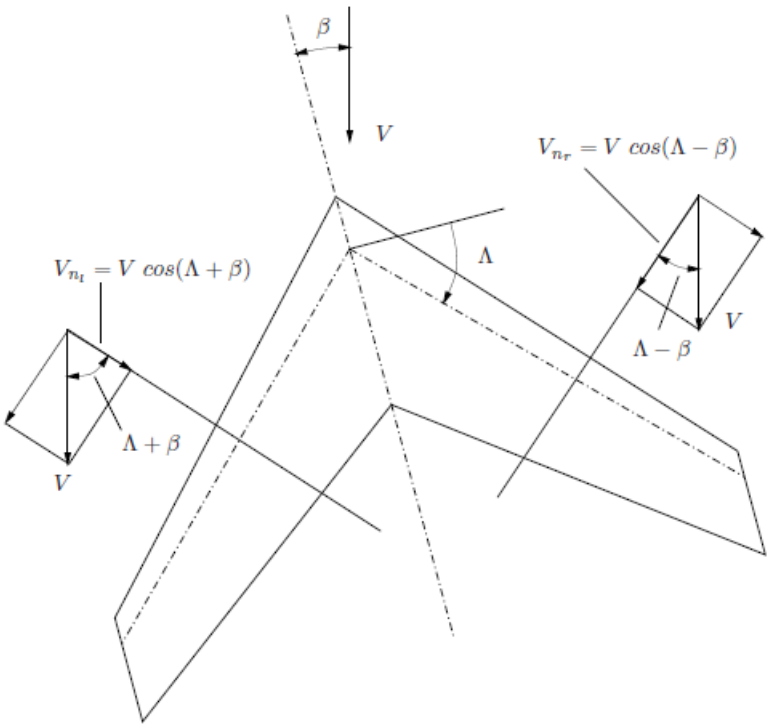

Figure 2.2: Difference in velocities over the left and right wing for a swept wing due to sideslip. From "Flight Dynamics" (p. 199), by Mulder et al, 2013.

A sweep angle was introduced for aircraft flying at subsonic airspeeds as sweep increases the critical Mach number (M_{crit}), which is the free-stream Mach number where the local Mach number along the wingspan reaches Mach 1.0. Additionally, Anderson [40] defines another main function of sweep as "delaying the drag divergence to higher Mach numbers". However, swept wings increase the lift coefficient on the outboard wings, which may initially lead to a stall at the wingtip. A stall at the wingtips leads to loss of lift behind the aerodynamic center inducing a strong pitch-up moment and roll maneuver, thus further amplifying the stalled condition [41]. Roll control is lost as no counteracting roll moment can be provided as the outboard wing is stalled. Therefore, initial flow separation should occur at the inboard wing, which decreases the downwash over the tail and induces a pitch-down moment, thus recovering from the stalled condition. Aircraft with a sweep angle, therefore, have taper ratio which helps to move the lift inboard and reducing the aerodynamic wing bending moments as well as applying a twist and variate the airfoil planform along the wingspan.

The Fokker 100 has two other devices installed which help to prevent wingtip stall. A stall promotor and a leading-edge boundary layer fence are installed on the swept wings. A boundary layer fence induces an inboard cross-flow on the inboard wing to reduce the outboard wing at high angles of attack. Although wing fences decease the pitch up and roll-off tendency an increase in drag is accompanied with the devices.

Additionally, sweep induces a difference in local velocity over the left and right wing when the aircraft is in a sideslipping flight ($\beta \neq 0$). In Figure 2.2 a schematic representation of an aircraft in a sideslipping flight is shown. A difference in local velocity affects the local angle of attack per wing. When one of the wings exceeds the critical angle of attack before the other, lift on that wing will be lost and an aircraft starts to roll to the side of the stalled wing. In practice, this is what happens when an aircraft enters a stalled condition.

Lastly, aircraft with a T-tail configuration, thus applicable on the Fokker 100, are subject to an extremely dangerous condition also known as a deep stall. At high angles of attack, far above the initial critical angle of attack, severe pitch moment instability occurs. In Figure 2.3 the effect of the horizontal tail on static longitudinal stability or pitching stability can be seen.

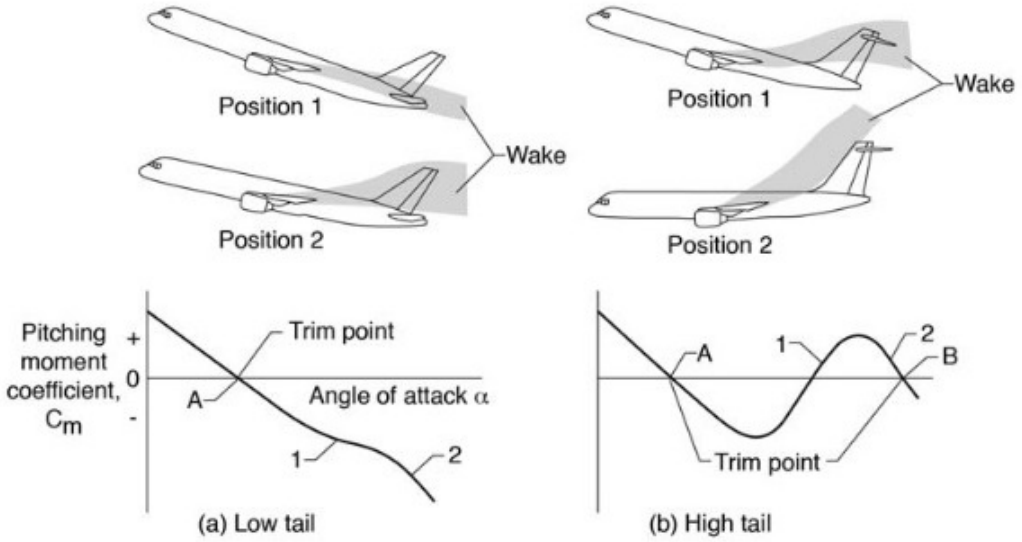

Figure 2.3: Effect of horizontal-tail position on static longitudinal stability. From "Simulation Modeling Requirements for Loss-of-Control Accident Prevention of Turboprop Transport Aircraft", by Crider and Foster, 2012.

An aircraft with a conventional tail and swept wings have reduced pitching stability when the angle of attack increase because the horizontal tail is located in the wake of the wing and has reduced effectiveness, as indicated by point 1 in the figure. However, at even higher angles of attack, the horizontal tail is operating at a lower downwash angle and higher dynamic pressure and thus increasing the pitch stability as indicated by point 2. A negative slope for the $C_m - \alpha$ curve or negative value for $C_{m_\alpha}(\frac{\delta C_m}{\delta \alpha})$

indicates a positive pitch stability.

An aircraft with sweep and a T-tail configuration can enter a deep stall as the horizontal stabilizer is in the wake of the main wings and has reduced dynamic pressure. At high angles of attack, the value for C_{m_α} changes from negative to positive and thus creating a pitch up moment amplifying the stall. Due to this the effectiveness of the elevators is substantially diminished or even negated and makes it almost impossible to recover from a stalled condition as the angle of attack cannot be reduced with a pitching motion.

To help aircraft recovery, and therefore also minimize deep stall occurrences for the Fokker 100, a stall identification system is available, namely a stick pusher. The stick pusher is a post-stall pusher which provides a nose-down input to help aircraft recovery. A stick pusher control law uses the angle of attack and the rate of change in the angle of attack as input to determine the activation of the stick pusher. At high airspeed entry rates, the stick pusher control law will activate the stick pusher at a lower angle of attack.

Another influence on the stall behavior is the center of gravity position, which determines the stall speed and handling characteristics during and after a stall. A forward center of gravity position is used to determine the stall speed. A nose-down pitching moment occurs when the center of gravity is in front of the center of pressure, which requires a negative tail load to maintain equilibrium. An increase in lift is required to maintain equilibrium and thus increases the stall speed. However, handling qualities are determined with a aft center of gravity position, as stability is decreased.

Flight Conditions
Besides aircraft configurations, flight conditions also influence the stall behavior of an aircraft. For example, banking the aircraft influences the stall. An aircraft in a steady, coordinated and horizontal turn requires an increase in lift as the lift component is now decomposed using the bank angle. An increase in lift can be achieved by increasing the angle of attack and therefore exceeding the critical angle of attack earlier compared to level flight. A common requirement in stall certification test is therefore also to show compliance using turning stalls.

Another major impact on the stall behavior are the weather conditions and specifically contamination on the wings due to weather. For example, icing- or volcanic conditions negatively affect the flow over the wings and the generated lift. A decrease in lift may require an increase in the angle of attack and therefore lowering the difference between the local angle of attack and the critical angle of attack. Although weather conditions affect stall, these conditions are difficult to model and are therefore omitted from this research.

2.2.2 Aerodynamic stall properties

Aerodynamic stall properties should be included in modeling to properly cue pilots in stalled conditions. Therefore, the ICATEE introduced the concept of comprehensive UPRT. An aircraft is said to be in an upset condition when an unintentional maneuver leads to a condition where the aircraft has a pitch attitude larger than 25 degrees nose up, a pitch attitude lager than 10 degrees nose down, a bank angle exceeding 45 degrees or within the previous mentioned parameters but at an airspeed inappropriate for the (current) conditions [11, 42]. As part of the UPRT by ICATEE four levels of mitigation are proposed which are Awareness, Recognition, Avoidance, and Recovery. The first three mitigation levels are based on the prevention of upsets. Creating awareness helps better understanding what causes an upset to happen. Secondly, recognizing upsets and subsequently preventing upset with an immediate intervention helps to prevent upset conditions. Lastly, recovery strategies are taught to safely recover from an upset by applying the correct skill-based behavior to attend the correct flight path. Although upset conditions do not automatically lead to a stall, stalls are closely linked to upset conditions and is a condition which should be trained to proficiency in flight simulators. This requires decent (post)-stall models in FSTD. As part of the improvement of flight simulators ICATEE has recommended several features to be implemented, which are the following post-stall aerodynamic properties [43].

Degradation in Static/Dynamic Lateral-Directional Stability
A lateral stability aerodynamic parameter which is degraded is the so-called 'effective dihedral' C_{l_β}. This parameter describes the response in rolling motion with a certain sideslip angle β. A desirable effective dihedral is when $C_{l_\beta} < 0$. For example, if a rolling motion to the right is initiated, a sideslip to the right is induced which is counteracted with a rolling moment in the opposite direction, stabilizing

the aircraft. However, if the aircraft has a positive sideslip, the effective angle of attack for the right wing is increased and closer to the critical angle of attack. An increase in the local angle of attack may exceed the critical angle of attack and thus stalling the right wing prior to the left wing. A decrease in lift over the right wing will induce a rolling moment to the right and positively increase the value of C_{l_β}, thus making the aircraft less stable or even unstable. An unstable value for C_{l_β} means the rolling moment is even further increased.

The effective dihedral parameter is also influenced by sweep, flap settings, and wing twist. Aircraft with backward swept wings increase C_{l_β} negatively, thus increasing the lateral stability. However, if an aircraft with a sweep angle extends the flaps the lateral stability is decreased. A similar effect occurs when wing twist is applied to an aircraft. Generally, swept-wing aircraft will have a zero or negative value for the dihedral as this diminished unfavorable effects a high angles of attack prior to the critical angle of attack.

A static directional stability parameter or the so-called 'weathercock' stability C_{n_β} parameter is also affected in stalled conditions. A favorable characteristic for the weathercock stability parameter is to provide a positive yawing motion when an aircraft has a positive sideslip angle. This will reduce the angle of sideslip and put the nose of the aircraft in the direction of the wind. Therefore, a positive value for C_{n_β} is desired. The main contribution to the weathercock stability is the vertical stabilizer, which in a sideslipping flight with a positive sideslip will generate a counter-clockwise circulation, inducing an additional negative sidewash stabilizing the aircraft. However, at high angles of attack, the wake of the wing influences the effectiveness of the vertical and horizontal stabilizer and therefore decreases the value of C_{n_β}.

A common parameter in aerodynamic flight envelopes is the roll damping parameter C_{l_p}. In simulations when the aircraft enters the aerodynamic stall envelope an addition on this parameter is usually used to simulate the sudden roll-off when an aircraft stalls. A favorable roll damping would be characterized by a negative value for C_{l_p} as this will slow down the rolling motion of the aircraft. Roll damping is influenced by taper ratio λ, aspect ratio A and sweep angle Λ. An increase in taper ratio λ or aspect ratio A negatively increases the value whereas the sweep angle positively increases the value, indicating an increased and decreased roll damping effectiveness respectively.

The roll damping has a proportional relation to the lift gradient C_{L_α} when the aircraft is in the safe flight envelope. In this part of the flight envelope, the lift gradient has a positive value as can be seen in Figure 2.1. However, when the local critical angle of attack on the downgoing wing is exceeded, the roll damping is reduced. At the stalled wing the loss of lift may even be sufficient enough to amplify the rolling motion where C_{l_p} becomes positive.

Degradation in Control Response
At high angles of attack, separated turbulent airflow origination from the wings and fuselage negatively affect the control surfaces and therefore reducing control response effectiveness. Control response effectiveness is dependent on aircraft configuration. A dangerous situation occurs when aircraft experiences full loss of control, for example, an aircraft in a deep stall, or when experiencing control reversal. Control reversal is the adverse effect on the controllability of the aircraft. A roll input at a high angle of attack may induce control reversal. For example, initiating a right turn at high angles of attack causes the left aileron to deflect downward and subsequently increasing the local angle of attack and exceeding the critical angle of attack, stalling the left wing. As a result, the asymmetric lift distribution over the wings will cause a rolling motion to the left, opposite to what was initiated.

Roll-off or Uncommanded Roll Response Requiring Significant Control Deflection to Counter
An uncommanded roll response or roll-off occurs when wings stall independently of each other due to asymmetries in aircraft geometry or (atmospheric) disturbances. As one wing stalls before the other, the induced asymmetric lift distribution will cause the aircraft to roll-off in a certain direction, depending on which wing stalls first. Even though stall behavior is highly unpredictable, aircraft characteristic sometimes affects the roll-off tendency. Additionally, the amplitude of the rolling motion depends on the span-wise separation point, where a stall at the wingtip has a larger rolling motion compared to a stall at the root of the wing.

Apparent Randomness or Non-repeatability
The stall is a highly, nonlinear process in which the airflow has unpredictable behavior. Stochastic process and unpredictable stall behavior make it difficult to repeat a stall maneuver, both in-flight and

in a flight simulator. Although, each stall maneuver differs the recovery strategy remains equivalent, which is reducing the angle of attack. Including apparent randomness in stall models will create non-repeatability resembling real aircraft stalls.

Changes in Pitch Stability
As mentioned in subsection 2.2.1 aircraft with sweep angles are particularity prone to changes in pitch stability at a higher angle of attack, which can be seen in Figure 2.3. At high angles of attack, flow separation occurs at the wingtips and the loss of lift behind the aerodynamic center creating a strong positive pitching moment. A pitch-up motion in a stall is undesirable as the mitigation strategy is to pitch down and decrease the angle of attack. Aircraft, like the Fokker 100, with a T-tail configuration, have an additional influence on the pitching stability. At angles of attack far above the critical angle of attack, the pitching moment has changed to a positive value ($C_{m_\alpha} > 0$) and pitch inputs are unable to provide a counteracting pitching motion, known as a deep stall.

Stall Hysteresis
Aerodynamic hysteresis is defined by Yang [44] as *"Aerodynamic hysteresis of an airfoil refers to airfoil aerodynamic characteristics as it becomes history-dependent, i.e., dependent on the sense of change of the angle of attack, near the critical angle of attack"*. Aerodynamic hysteresis has practical importance as it determines the lift-to-drag ratio and maximum lift coefficient at a certain angle of attack. Stall and spin recovery may be affected as the flow re-attaches at a lower angle of attack compared to the separation angle of attack, i.e. the critical angle of attack. Aerodynamic hysteresis effects are included in Kirchoff's flow separation theory [45].

Mach Effects
Mach effects is another property which is related to the stall of the aircraft. At high subsonic airspeeds, the local airflow over the wings will become supersonic, inducing shock waves that cause the flow to separate and will potentially stall the aircraft. For stall modeling purposes, Mach number is usually an independent variable in models. However, as mentioned in section 2.2 Mach effects at high subsonic airspeeds are excluded from this research. In the certification flight test only subsonic stalls were conducted, where the Mach numbers range from Mach 0.25 to Mach 0.40.

Stall Buffet
Aerodynamic stall buffet and the induced structural vibrations are an important cue in stall training. A more in-depth analysis of stall buffet is given in section 2.3.

2.3 Aerodynamic Buffet

Buffet is the aerodynamic excitation due to flow separation which causes pressure fluctuations over the wing and can lead to the initiation of aircraft structural vibrations, which is known as buffeting [13, 46]. Buffet onset is defined as the spanwise position on the wing at which aerodynamic excitation starts, which usually coincides with the initial flow separation point and is therefore assumed here. Flow separation occurs at high angles of attack or high Mach numbers and depends on the geometry of the wing, for example, the sweep angle.

Aircraft manufacturers determine buffet characteristics such as the buffet envelope in early design stages, as buffeting limits the flight envelope, buffeting determines aircraft structural limits and also induces structural fatigue [44, 47]. In-flight buffeting affects aircraft handling qualities and also decreases passenger comfort. It is therefore important to determine the buffet envelope in early stages. A common graphical representation of the buffet onset envelope is shown in Figure 2.4 and is the so-called buffet onset boundary chart. In this chart, the buffet onset point is visualized as a function of Mach number and lift coefficient.

Despite imposing limits on the aircraft flight envelope, buffeting has been proven useful for pilots. Buffeting effects are an initial cue for pilots to indicate entering an unsafe flight envelope, e.g. stalling of the aircraft. At the buffet onset point, these structural vibrations can be felt throughout the aircraft, when the percieved specific forces exceed a threshold in the human vestibular system. Even so, these vibrations can be measured using accelerometers. However, human and accelerometer perception of buffet characteristics, such as buffet frequency and intensity, is dependent on aircraft configuration and the relative location to structural modes.

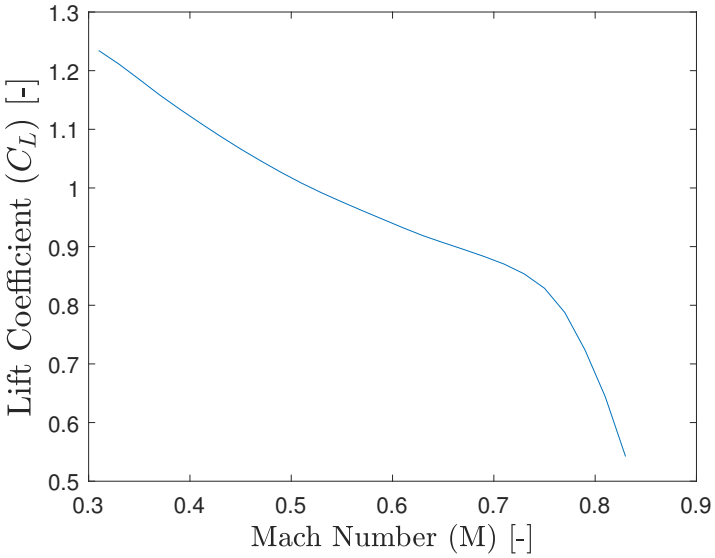

Figure 2.4: Typical buffet onset curve and flow separation at different flight regimes. Adapted from "Development and Implementation of Aerodynamic Analysis Methods for Aircraft Conceptual Design", by Bérard and Isikveren, 2009.

2.3.1 Background on Buffet Modeling

In early studies on aircraft buffet, 2-D wing models were used in wind-tunnel experiments to determine buffeting effects at a certain combination of Mach number, Reynolds number and angle of attack [48–50]. These 2D wing models used strain gauges to measure the wing root bending moments, where compliance was shown by correlation of wind-tunnel results to flight test data. Technological advances in the aviation industry led to a shift from subsonic flight to transonic flight. A new flight regime posed new technological challenges, one of which being aerodynamic effects in the transonic flight regime. Research led to buffet onset and buffet load predictions using pressure measurements [46]. Buffet onset predictions methods have been expanded over the past decade. Most of these techniques are based on wind-tunnel data experiments with some correlation to flight test data. Experimental research in 2016 using a wind-tunnel setup defined several buffet onset indicators and compared each of these indicators with each other [51]. Commonly used buffet onset indicators are Root Mean Squared Error (RMSE) signal variations of root strain gauges, RMSE signal variations of wingtip accelerations measured with accelerometers, lift curve slope reduction, pitch moment break, axial force break and trailing edge pressure divergence [52]. In several studies, for example by Dang and van Eijndhoven [37, 52], similar conclusions were found. Methods like the pitching moment break and the lift curve slope break generally did not produce satisfactory results in predicting the buffet onset point. However, the other methods did show satisfactory results when correlating the buffet onset point to flight test data.

A buffet intensity parameter, as the name suggests indicates the buffet intensity, has been extrapolated from methods such as the strain gauge responses and the wind tunnel ambient unsteadiness. Buffet intensity may be divided into three different categories, namely light, moderate and heavy when a correlation to flight test data was made. Additionally, wing characteristics also have an influence on the buffeting behavior [53].

A more recent study used aircraft wing geometries to determine the buffet envelope. In this methodology a combination of fractional change transformations and simple sweep theory as well as the buffet onset of a seed aircraft to determine the buffet envelope for any generic transport aircraft [54]. Wing geometries affecting the buffeting were identified as wing aspect ratio, taper ratio, wing quarter-chord sweep, wingtip section maximum thickness-to-chord ratio, wingtip section thickness chordwise position and wingtip section maximum camber, which are all known parameters in the early design stages. As two methods were used to determine the buffet model for a generic transport aircraft. The first method used a generic reference buffet envelope to determine the new buffet envelope. In the second method a buffet onset of a known seed aircraft was used, to determine the buffet envelope for a new aircraft. Better results were obtained with the second method, however, this requires a buffet envelope

of a seed aircraft to determine to buffet envelope for any other aircraft [36].

Currently, wind-tunnel experiments and CFD calculations are used to more accurately predict buffet characteristics in the early design stages [47,55]. A common drawback for each of these models is the fact that these are mainly based on wind-tunnel experiment and CFD calculations with little to no correlation to flight test data. Performance is satisfactory based on the made assumptions and conditions. However, a drawback of the wind-tunnel test remains the fact that it requires scaling to represent an entire aircraft, which in most studies is neglected or under-determined. CFD calculations usually include extensive optimization procedures which may be too computationally intensive and costly. Lastly, aerodynamic behavior is only fully captured in flight test data.

Currently, methods using flight test data is scarce and is currently not able to accurately predict buffet onset and transient behavior. An approach to model buffet using flight test data has been used in [17,18] which is based on Kirchoff's theory on flow separation. However, the threshold activating the buffet in the extended flight envelope requires improvement, as the model has a delayed buffet activation and a premature buffet deactivation.

Based on the literature a more suitable buffet model, which includes a more accurate buffet onset or phase-in and transient behavior, has to be identified. A starting position for the buffet onset and transient behavior could be identified based on Kirchoff's flow separation theory. Additionally, two suggestions in studies might also be worth looking into, one of which is lowering the simulator buffet onset angle of attack and the other one is varying the amplitude as a function of angle of attack [28], which both could be used in conjunction with the three different severity categories as described in the work of Mabey [53].

2.3.2 Current Stall Buffet Model

In the work of van Horssen [18], the buffet is modeled separately from the aerodynamic stall dynamics. A separation in modeling is possible as the buffet was identified to entail mainly high frequencies, whereas the stall dynamics had lower frequencies. On the frequency axis, both models were separated sufficiently. Although two separate models were developed there was still a dependency as both models were based on the same theory. The flow separation parameter 'X' based on the Kirchoff's flow separation theory was used to model aerodynamic and buffet characteristics. Therefore, Kirchoff's theory on flow separation shall be described in more detail. Secondly, familiarization with the basic concepts of the theory is applied to the current buffet model.

2.3.2.1 Kirchoff's Theory on Flow Separation

Aerodynamic behavior starts to change as the angle of attack increases and becomes more nonlinear when flow separation occurs. Kirchoff's theory on flow separation attempts to capture nonlinear, unsteady, dynamic behavior and hysteresis effects during stall [45]. The model structure for the theory is in its simplicity able to capture these aerodynamic effects which only requires four parameters and two time-constants. In the model structure, a non-dimensional state is introduced, indicated with the 'X', which defines the point on the airfoil where flow separation occurs. The X-parameter ranges from $[0, 1]$, whereby 'X = 1' indicates a fully attached airflow and 'X = 0' is a fully separated airflow. A graphical illustration of the X-parameter can be seen in Figure 2.5.

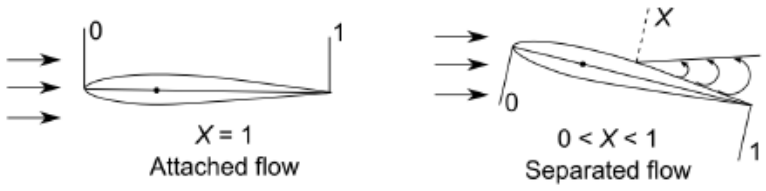

Figure 2.5: Airfoil flow separation point. From "Unsteady and Post-Stall Model Identification Using Dynamic Stall Manoeuvres", by Dias, 2015.

The flow separation point can be approximated by a first order differential equation and is given by:

$$\tau_1 \frac{dX}{dt} + X = \frac{1}{2} \cdot \left\{ 1 - \tanh(a_1 \cdot (\alpha - \tau_2 \dot{\alpha} - \alpha^*)) \right\} \tag{2.1}$$

In Equation 2.2 the four parameters influencing the flow separation point are $a_1, \alpha^*, \tau_1, \tau_2$. Parameters a_1 and α^* are related to steady airflow conditions whereas τ_1 and τ_2 are used to describe the dynamic effects of flow separation. The model validation for the longitudinal dynamics in stalled conditions was proven successful in Fischenberg [45]. A nonlinear relation between the lift coefficient and the non-dimensional state 'X' was established and is approximated by:

$$C_L(\alpha, X) = C_{L_\alpha} \left\{ \frac{1 + \sqrt{X}}{2}^2 \right\} \alpha \tag{2.2}$$

In Equation 2.2 an approximation for the lift coefficient is shown and only depends on the angle of attack (α) and the flow separation point (X). However, it can easily be extended with other aerodynamic derivatives, namely derivatives related to pitch rate (q), rate of change of angle of attack ($\dot{\alpha}$), elevator deflection (δ_e) and the lift coefficient at zero angles of attack (C_{L_0}). In the work of van Ingen [17], a model structure selection was based on a multivariate orthogonal function procedure to determine the different aerodynamic parameters for the model of the lift coefficient. In Equation 2.3 the selected model structure for the lift coefficient can be seen.

$$\hat{C_L} = C_{L_0} + C_{L_\alpha} \left\{ \frac{1 + \sqrt{X}}{2}^2 \right\} \alpha + C_{L_{\alpha^2}} (\alpha - 6^\circ)_+^2 \tag{2.3}$$

where the last term in Equation 2.3 ensures that influences on $C_{L_{\alpha^2}}$ are restricted to be in the high angle of attack regime (i.e. when $\alpha \geq 6^\circ$), which can be seen in mathematical form in Equation 2.4.

$$(\alpha - 6^\circ)_+^2 = \begin{cases} (\alpha - 6^\circ)^2, & \text{when } \alpha \geq 6^\circ. \\ 0, & \text{otherwise.} \end{cases} \tag{2.4}$$

Other models capturing nonlinear dynamics in both longitudinal, as well as lateral directional, at high angles of attack, have successfully been implemented in the work of van Horssen, van Ingen and Dias [17,18,35], in which a more in-depth description of the parameter estimation techniques was included.

In the subsections below the influence of each parameter for the differential equation as seen in Equation 2.1 is shown. Each figure below consists of two sub-figures where the first figure depicts the estimated lift coefficient and the second figure depicts the flow separation point. The lift coefficient is calculated based on Equation 2.3 where the estimates for each aerodynamic parameter and the X-parameter are given in the figure. In each figure, only one X-parameter is altered while the other parameters remain constant. However, dynamic and hysteresis effects are only captured with a dynamic movement, whereas both formulas are static. Therefore, a forced oscillating function is used to simulate dynamic effects, which is adapted from Smets [16] and is given by:

$$\alpha(t) = (7^\circ - 7^\circ \cos(4 \cdot t)) \frac{\pi}{180} \tag{2.5}$$

Parameter a_1
This parameter determines the abruptness of the stall and may be estimated based on flight test data and/or wind tunnel data. Accurate parameter estimation requires the aircraft to reach the maximum lift coefficient and this occurs when $X \approx 0.7$. Stall behavior becomes more abrupt when the value of a_1 increases. Additionally, a slight increase in the lift coefficient is obtained, which can be seen in Figure 2.6.

Parameter a^*
The parameter a^* influences at what angle of attack the flow separation is halfway along the airfoil, i.e. at what angle of attack $X = 0.5$. An increased value delays the flow separation point and also increase the critical angle of attack and therefore the maximum achievable lift coefficient. An accurate estimate for α^* also requires stall maneuvers to reach the maximum lift coefficient. Figure 2.7 shows the influences of an increased value of a^*.

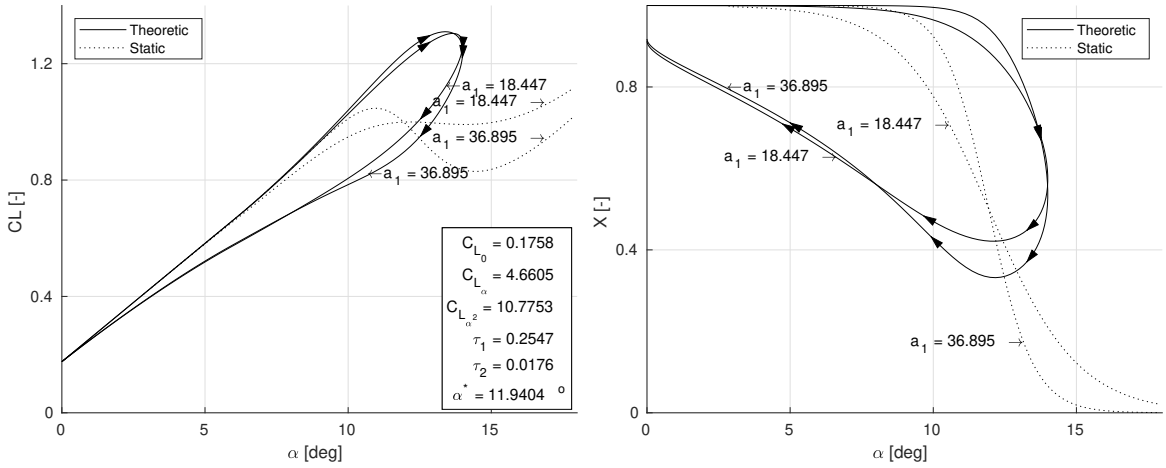

(a) Influence of a_1 on the lift coefficient.

(b) Influence of a_1 on the flow separation point.

Figure 2.6: Static and dynamic influences of a_1 on the lift coefficient and flow separation point. From "Subjective Noticeability of Variations in Quasi-Steady Aerodynamic Stall Dynamics", by Smets, 2018.

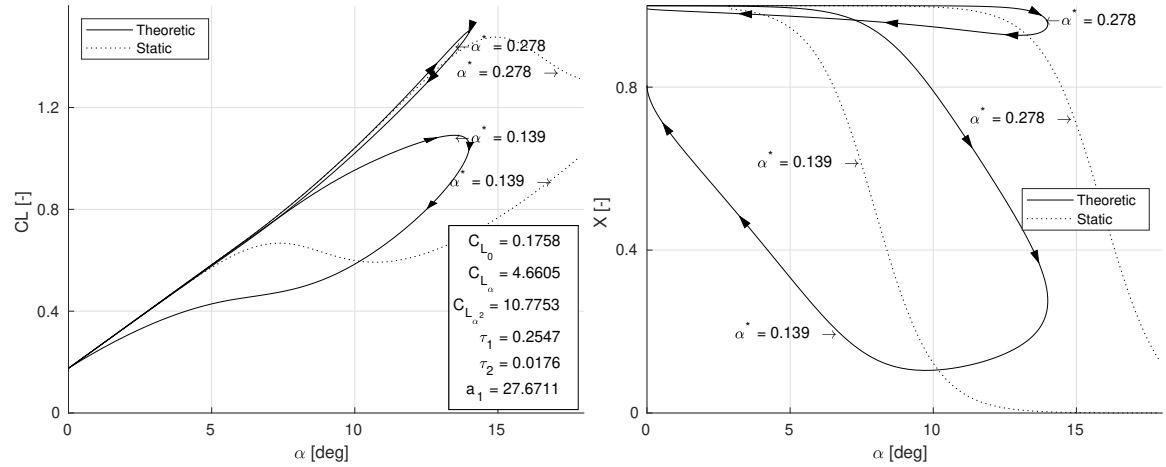

(a) Influence of a^* on the lift coefficient.

(b) Influence of a^* on the flow separation point.

Figure 2.7: Static and dynamic influences of a^* on the lift coefficient and flow separation point. From "Subjective Noticeability of Variations in Quasi-Steady Aerodynamic Stall Dynamics", by Smets, 2018.

Parameter τ_1

Airflow separation and reattachment is subjected to time delay modeled by X-parameter τ_1, as airflow requires adjustment time due to sudden changes in the angle of attack. In Figure 2.8 it can be seen that an increase in the time delay a higher C_L can be achieved at the cost that flow reattachment and thus aircraft control takes a longer time. An accurate estimation of this parameter can be achieved with dynamic stall maneuvers as steady stall approaches lead to a correlation between states.

Parameter τ_2

Lastly, the τ_2 parameter is the so-called hysteresis parameter and accounts for the hysteresis effect. Hysteresis effect depends on the rate of change in the angle of attack $\dot{\alpha}$. At a positive rate for $\dot{\alpha}$ flow separation occurs at higher angles of attack and a negative rate for $\dot{\alpha}$ will re-attach flow at lower angles of attack. Accurate estimates for this parameter are determined based on dynamic stall maneuvers. In Figure 2.9 this phenomena is shown for two different values of τ_2.

Longitudinal dynamics in stalled conditions were captured successful using model validation [45]. However, the theory only explicitly demonstrates the effect of the flow separation parameter on the lift coefficient. More recently, stall models capturing the nonlinear dynamics in longitudinal and lateral direction have been found [17, 18, 35], where a dependency was made flow separation parameter. Ad-

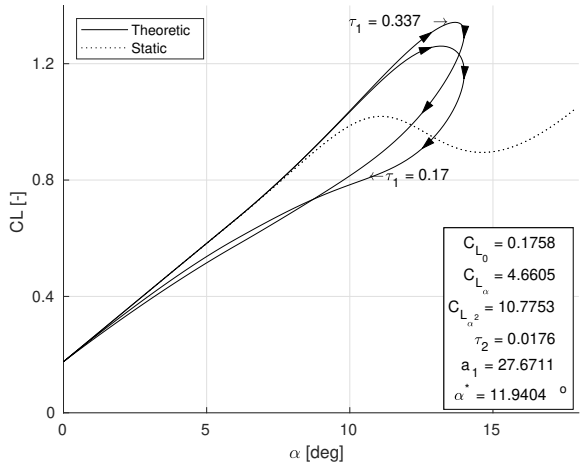

(a) Influence of τ_1 on the lift coefficient.

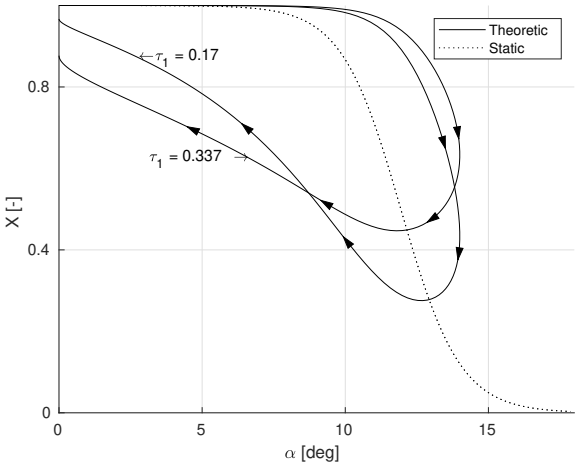

(b) Influence of τ_1 on the flow separation point.

Figure 2.8: Static and dynamic influences of τ_1 on the lift coefficient and flow separation point. From "Subjective Noticeability of Variations in Quasi-Steady Aerodynamic Stall Dynamics", by Smets, 2018.

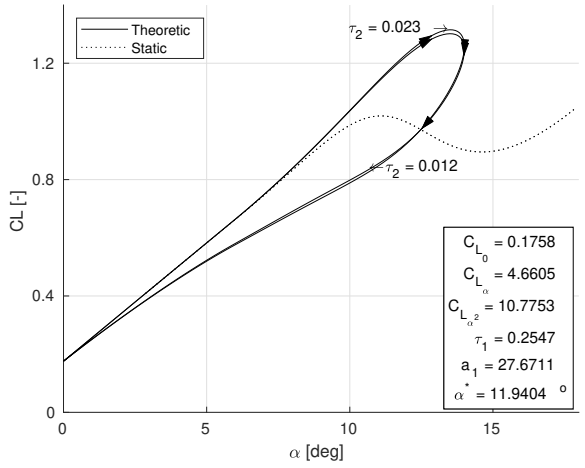

(a) Influence of τ_2 on the lift coefficient.

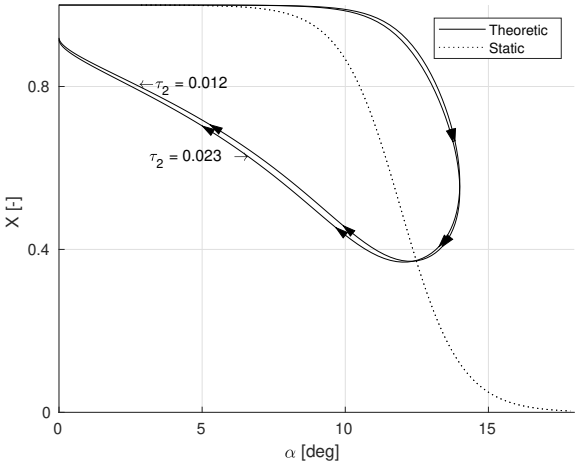

(b) Influence of τ_2 on the flow separation point.

Figure 2.9: Static and dynamic influences of τ_2 on the lift coefficient and flow separation point. From "Subjective Noticeability of Variations in Quasi-Steady Aerodynamic Stall Dynamics", by Smets, 2018.

ditionally, the aerodynamic moments and forces in the longitudinal direction were extended with the X-parameter. In Equation 2.6 the formulas for both longitudinal dynamics are shown.

$$\begin{aligned} \hat{C_D} &= C_{D_0} + C_{D_\alpha}\alpha + C_{D_{\delta_e}}\delta_e + C_{D_X}(1-X) + C_{D_{C_T}}C_T \\ \hat{C_m} &= C_{m_0} + C_{m_\alpha}\alpha + C_{m_{X\delta_e}}\texttt{max}(\frac{1}{2}, X)\delta_e + C_{m_{C_T}}C_T \end{aligned} \tag{2.6}$$

Normally aerodynamic parameters can be estimated using linear estimation techniques such as Ordinary Least Squares (OLE). However, the X-parameter is calculated using a first-order, nonlinear differential equation, which indicates that parameter estimation becomes a nonlinear optimization procedure. A nonlinear optimization procedure cannot guarantee a global optimum and optimization becomes more computationally intensive. An overview with (nonlinear) parameter optimization techniques can be found in chapter 4. Hereafter, Kirchoff's flow separation theory is used in the modeling of the buffet component in stalled conditions.

2.3.2.2 Citation Stall Buffet Modeling

In the work of Horssen [18] the buffet component was modeled using the measured body accelerations from the Attitude and Heading Reference System (AHRS) of the Cessna Citation II. The time-series of the measured accelerations were transformed to the frequency domain applying a Fourier analysis to obtain a periodogram, which is the best possible estimate of a Power Spectral Density (PSD). The periodogram was averaged over several realizations, and the periodogram in the lateral and vertical direction is shown in Figure 2.10.

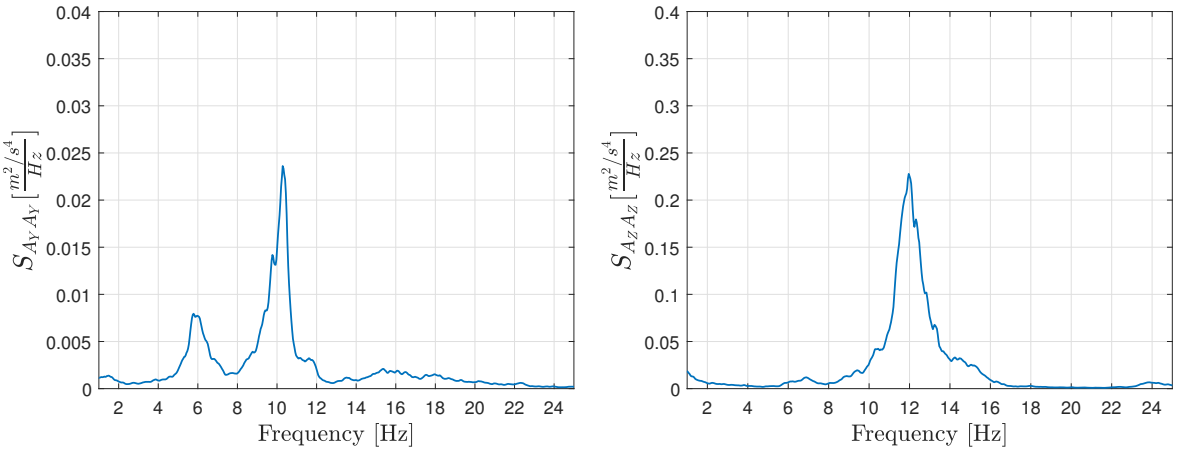

(a) Periodogram in **lateral direction** at **5,500** meter in **clean configuration** for the Cessna Citation II.

(b) Periodogram in **vertical direction** at **5,500** meter in **clean configuration** for the Cessna Citation II.

Figure 2.10: Periodogram in lateral and vertical direction at 5,500 meter in clean configuration. Adapted from "Aerodynamic Stall Modeling for the Cessna Citation II based on Flight Test Data", by Horssen, 2016.

In Figure 2.10 a peak at 6 and 12 Hz is visible for the buffet in the lateral direction, whereas the most power is located at 12 Hz for the buffet in the vertical direction. Also, the amplitude in the vertical direction is a factor ten higher than the one in the lateral direction, indicating that the vertical acceleration in a stalled condition is dominant. A periodogram in the longitudinal direction was omitted from the research as the acceleration in the x-direction was effectively zero. In both plots, the dominant frequencies are located at a higher frequency than the aircraft dynamics, which allows for separation of the low-frequency stall and high-frequency buffet models. Additionally, the altitude had no clear influence on the buffeting component, hence a single model was constructed.

The periodogram is then used to shape a filter response to fit the frequency response function. A white noise signal, with an intensity equal to one, was passed through a shaping filter, where the model structure is given by Equation 2.7 to simulate the buffet.

$$S_{yy} = |H(j\omega)|^2 S_{uu} \tag{2.7}$$

In order to model the frequency response function of the buffet a second-order low-pass filter was used. An example of a second order filter can be found in Equation 2.8.

$$H(j\omega) = \frac{H_0 \omega_0^2}{(j\omega)^2 + \frac{w_0}{Q_0} j\omega + \omega_0^2} \tag{2.8}$$

where H_0 is the gain of the filter, ω_0 is the break frequency and Q_0 is quality factor i.e. represents the amplitude of the resonance peak. A value for each parameter in the vertical direction were estimated as H_0 = 0.05, ω_0 = 75.92 rad/s, and Q_0 = 8.28. In the lateral direction two, second-order filters, one for each frequency, are used whereas only one filter was used in the vertical direction. A dependency on the flow separation parameter is created by scaling the amplitude of the buffet model in either direction with $1 - X$. In this case, a linear relationship between flow separation and buffet intensity is created as the buffet intensity increases as the X-parameter decreases. An additional gain multiplication ensures the correct buffet intensity, as well as ensuring the model stays within simulator limits. Lastly, the

phase-in and phase-out of the buffet have been set based on a threshold, i.e. the buffet is activated only if the threshold is met. Currently, the threshold for buffet activation is set at 0.89. In Figure 2.9 an example for the buffet model in the lateral direction is shown.

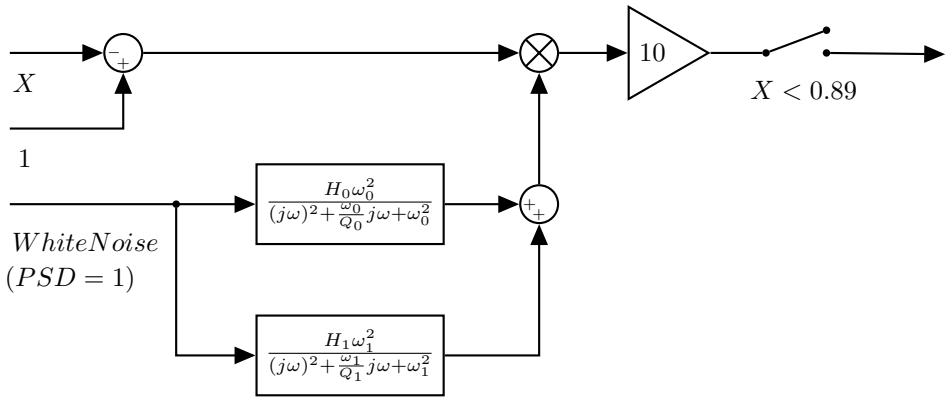

Figure 2.11: Effect of the flow separation on the stall buffet, example given of the lateral stall buffet. Adapted from "Aerodynamic Stall Modeling for the Cessna Citation II based on Flight Test Data", by Horssen, 2018.

In the work of Smets [16], the buffet model showed good compliance with reality based on SME opinions. However, improvements in the current buffet model are still required. Currently, the phase-in and phase-out of the stall buffet model are inaccurate as can be seen in Figure 2.12 which shows the acceleration in both lateral and vertical direction. An improvement was made by incorporating the time delay parameter τ_1, but this only partially solved the problem.

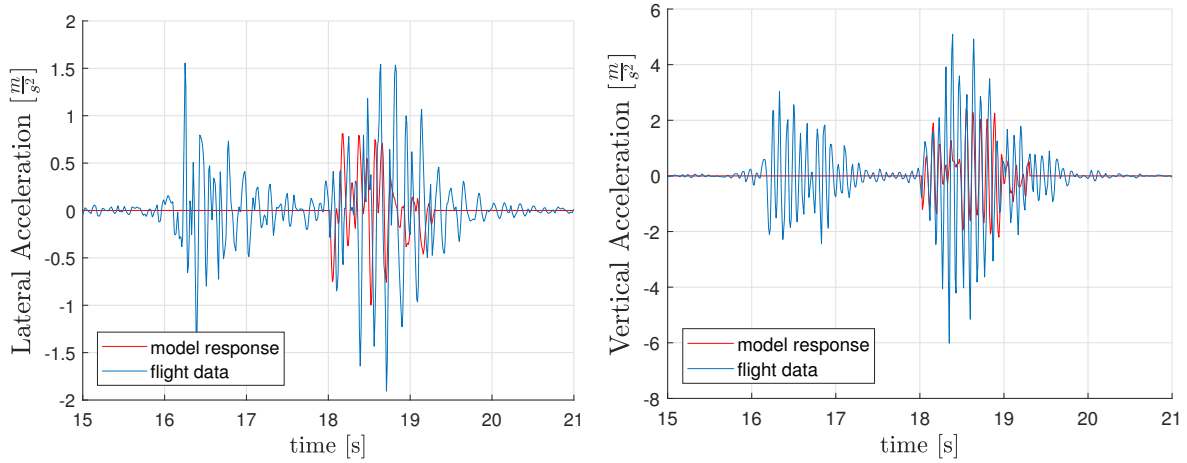

(a) Timeseries for the lateral accelerations for both flight test data and model response.

(b) Timeseries for the vertical accelerations for both flight test data and model response.

Figure 2.12: Accelerations in vertical and lateral direction. Adapted from "Aerodynamic Stall Modeling for the Cessna Citation II based on Flight Test Data", by Horssen, 2016.

Chapter 3

Flight Data

In this chapter, an overview of aspects related to the flight test data of Fokker is given. First of all, the stall maneuvers were flown with the Fokker 100 and therefore some characteristics of the Fokker 100 are given in section 3.1. section 3.2 entails the different flight test instrumentation used during the stall maneuvers. The stall test flights were conducted as part of the Joint Aviation Requirements (JAR) certification test. Fokker also conducted several stall maneuvers which can be found in section 3.3. A short introduction on how the data is stored is covered in section 3.4. Lastly, section 3.5 contains noteworthy aspects of the flight data.

3.1 Fokker 100 Characteristics

The Fokker 100 is a regional jet with twin rear fuselage-mounted engines used for short to medium range type of operations. Its Maximum Take-Off Mass (MTOM) is 44,450 kilogram and the maximum operating altitude is 35.000 feet. The two Rolls-Royce Tay Mk 650 turbofan engines provide a maximum thrust of 67.17 kN. An overview of external dimensions for the Fokker 100 is given in Figure 3.1, whereas the dimensions for the Cessna Citation II can be found in the work of van Horssen and van Ingen [17,18]. An overview of dimension for both aircraft can be found in 3.1[1]. From the characteristics and the dimensions in the table and the figure, a large difference in aircraft size and sweep angle can be seen, however, the aspect ratio, taper ratio, and dihedral are quite similar for each aircraft.

Table 3.1: Fokker 100 and Cessna Citation II characteristics.

(a) Characteristics of the Fokker 100.

Name	Symbol	Value	[Unit]
Wing Span	b	28.07	$[m]$
Wing Area	S	93.50	$[m^2]$
Aspect Ratio	A	8.43	[-]
Taper Ratio	λ	0.1966	[-]
Sweep Angle (c/4)	Λ	17.4	$[^\circ]$
Dihedral	Γ	2.5	$[^\circ]$

(b) Characteristics of the Cessna Citation II.

Name	Symbol	Value	[Unit]
Wing Span	b	15.9	$[m]$
Wing Area	S	30.0	$[m^2]$
Aspect Ratio	A	8.43	[-]
Taper Ratio	λ	0.2386	[-]
Sweep Angle (c/4)	Λ	1.4	$[^\circ]$
Dihedral	Γ	4.0	$[^\circ]$

[1] Aircraft characteristics and dimensions are obtained from the Aircraft Operations Manual (AOM) and technical drawings of the Fokker 100 and Cessna Citation II

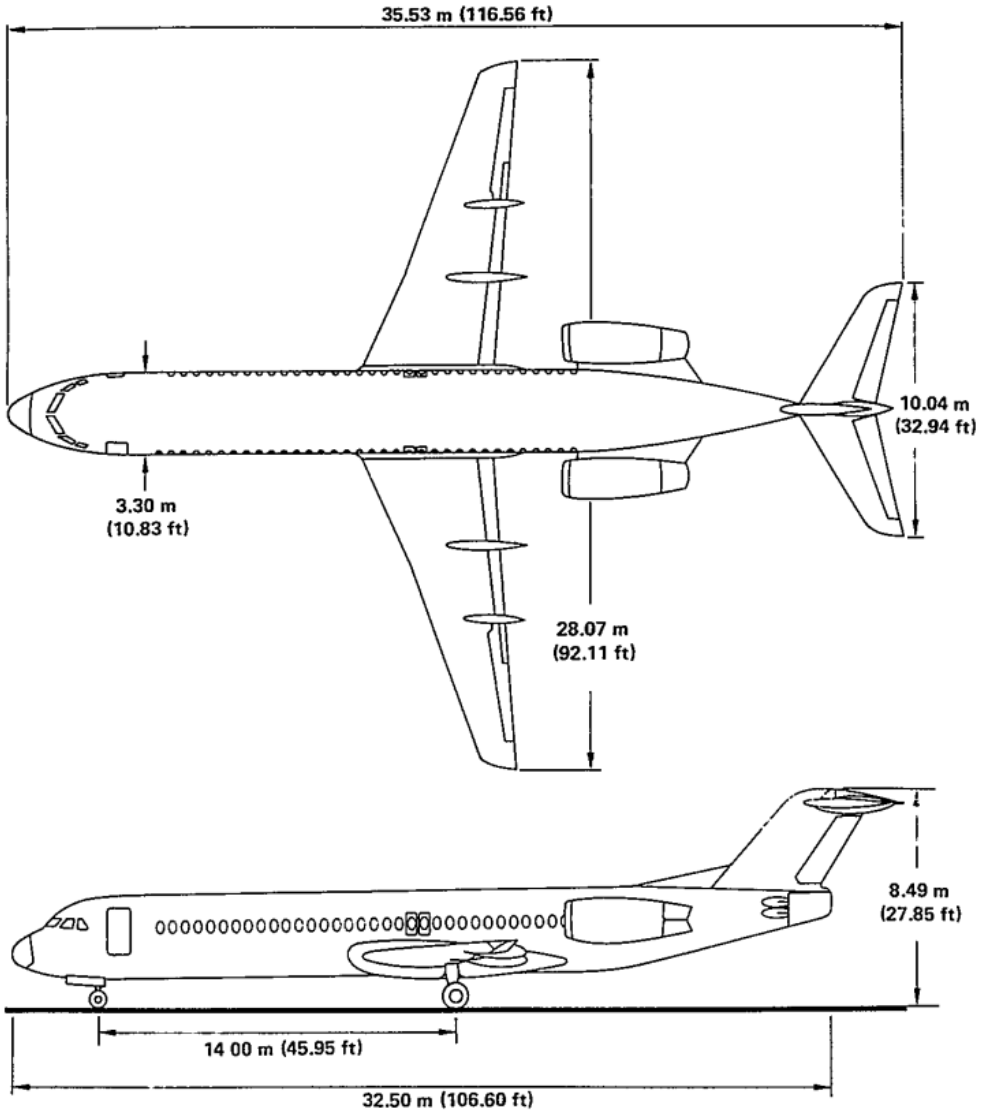

Figure 3.1: An overview of Fokker 100 dimensions. From "Aircraft operating manual for the Fokker 100".

3.2 Fokker 100 Flight Test Instrumentation

To comply with the regulations Fokker had to conduct flight certification tests to acquire certification data with the Fokker 100. Therefore, two important instrumentation systems used during these tests, which are the Air Data System and the Inertial Reference System (IRS), shall be explained in more detail below. Lastly, the processing of the measured parameters shall be discussed.

Air Data System

The air data system consists of four subsystems which are three pitot-static systems, two angle-of-attack vanes, two temperature probes, and two Air Data Computers (ADC). The pitot-static system provides information on the static and pitot pressure to the air data computer as well as various other systems. Location of the three pitot tubes is at the forward fuselage, whereas the three static ports are located on the left- and right-hand side of the fuselage. Interconnection of left and right static ports minimize the influence of side-slip. Air data computer one and two receive pressures from the pitot and static system one and two respectively. System three provides pressure information to the standby systems. The two angle-of-attack vanes sensors are located left (vane 1) and right (vane 2) of the forward fuselage and provide information on angle-of-attack to the stall prevention system, Automatic Flight Control and

Augmentation System (AFCAS) and ADC. Outside air temperature is provided to the ADC with two temperature probes. Lastly, the two ADC convert the inputs from the angle-of-attack sensors, pitot-static system, temperature probes, and Altimeter Set Panel (ASP) into electrical signals. These signals are used as inputs for other subsystems including the AFCAS and Flight Management System (FMS).

Inertial Reference System

In the Fokker 100, two IRS, a Mode Select Unit (MSU) and a Inertial System Display Unit (ISDU) are installed, which provide information on attitude and navigation by measuring body-specific forces and body axis rotational rates. An increase in accuracy is achieved when True Airspeed (TAS) information from the ADC is provided to the IRS. The IRS output signals are provided to various flight and navigation systems, for example, the FMS.

Data Processing

Measured data from these instrumentation systems are pre-processed in the Meet en Registratie en Verwerkings Systeem (MRVS) by the various MRVS data reduction stations. An overview with the measured and processed in-flight parameters provided by the MRVS can be found in Table 3.2.

Table 3.2: Parameters measured by ADS and AHS.

Name	Symbol	Sample Frequency [Hz]	σ^2	Unit	Source
Angle of Attack (AoA)	α	16	2.81e-06	$[RAD]$	Left AoA Vane
	α	16	2.32e-06	$[RAD]$	Right AoA Vane
Body Accelerations	A_{X_B}	50	4.74e-04	$[m/s^2]$	IRS
	A_{Y_B}	50	8.27e-04	$[m/s^2]$	IRS
	A_{Z_B}	50	4.10e-03	$[m/s^2]$	IRS
True Airspeed	V_{TAS}	8	8.76e-02	$[m/s]$	ADC 1
	V_{TAS}	8	9.13e-02	$[m/s]$	ADC 2

The pre-processed data from the MRVS is provided to the Fokker Data Verwerking Systeem (FDVS). In the FDVS STandaard Berekeningen (STB) or Standard Calculations are performed which are added to the FDVS database. These standard calculations are required for further analysis of flight test results. In the STB the calculated input parameters are synchronized using linear interpolation with a common sample frequency of 16 Hertz. In most cases the sampling frequency of 16 Hz is sufficient, however, some output parameters require different sample rates and are calculated entirely based on this new sample rate and parameters. Additionally, interpolation at higher sample rates may introduce additional noise characteristics and scatter on the output. The calculation of parameters, such as the lift coefficient, Mach number, and rate of change of angle of attack, used in this research is conducted according to Fokker Report DAS-100-012.

3.3 Fokker 100 Stall Maneuvers

As part of certification and compliance with JAR regulations, Fokker also had to conduct stall test flights. Stall tests are conducted according to JAR 25.201 - stall demonstration and JAR 25.203 - Stall characteristics. Compliance has also been shown for stall warning devices and stall speeds, however, a description is omitted here and can be found in AC 25-7D [56]. The purpose of aircraft stall testing is:

- Defining the reference stall speeds, which varies for any likely combination of aircraft weight, altitude and aircraft configuration;
- Demonstrating adequate handling qualities, which allow safe recovery from the highest attainable angle of attack under normal flight conditions;
- Determining an adequate pre-stall warning, either aerodynamic (buffet) or artificial (stick shaker) to allow a safe recovery from a high angle of attack.

An increase in the angle of attack should be maintained during stall testing up until the point where the aircraft behavior gives the pilot a clear and distinctive indication, which is either aerodynamic or artificial, of a stalled aircraft. A summary of the stall demonstration and stall characteristics is given for the wings level stalls only.

JAR-25-201 Stall Demonstration

Stall demonstration should indicate a safe recovery from an unintentional stall by applying normal recovery procedures, thus requiring no unusual piloting techniques. Stalls are demonstrated in wings-level conditions and 30 ° banked turns with power off or on, for all normal operation configurations. Stall characteristics are tested with an aft center of gravity limit, which is the most adverse stall condition. Stall tests are flown at trimmed conditions, were hands-off flight is possible, at an airspeed 13 percent to 30 percent above the stall speed, with the appropriate power settings. Longitudinal control is applied to ensure a steady deceleration rate (stall entry rate) of 1 kts/s or 3 kts/s until the aircraft is in a stalled condition. Unreversed control inputs should produce the correct roll and yaw until the aircraft is stalled. In addition, prevention of or recovery from a stall should be possible using normal control inputs. Lastly, aircraft susceptible to deep stalls, should provide adequate recovery control at, and sufficiently beyond, the critical angle of attack.

JAR-25-203 Stall Characteristics

An aircraft is considered stalled when the pilot has a clear and distinctive indication to cease increasing the angle of attack, and normal recovery techniques are initiated. A clear and distinctive indication of an aircraft in a stalled condition is given by one or any of the stall characteristics listed below. First of all, pitch attitude stops increasing or a pitch control is held for two seconds at aft stop, whichever condition occurs later. Secondly, an distinctive, easily recognizable, and uncommanded nose-down pitch which cannot be easily arrested. In addition to the nose-down pitch, a not immediately controllable rolling motion is also present. The accompanied rolling motion may not exceed a roll angle of approximately 20 degrees for a wings-level stall, from stall to recovery. Lastly, a strong and effective deterrent for further speed reduction is demonstrated by the aircraft as an unmistakable and inherent aerodynamic warning, i.e. the stall buffet. A deterrent buffet is for example characterized by an intensity that inhibits cockpit instruments reading and requires a strong determined effort to increase the angle of attack any further.

In the database with flight recordings, stall maneuvers characterized by STALL-CHARACT-IDLING are available, which resemble the JAR wings-level stall maneuvers.

3.4 Fokker 100 Stall Data Storage

All data is currently maintained with `MICROSOFT SQL Server Management Studio` and is accessible through the TUD Network only. In Figure 3.2 an overview of the `MICROSOFT SQL` database structure is depicted. Initially, the structure consisted of a combination of aircraft, flight and recording parameters as this combination used in the MRVS data. Later on, additional tables were included to have a better overview of other aspects, such as other parameters.

However, the database only contained compressed data which required decoding. A decompression tool was written in `MATLAB` which reversed engineered different compression types, such as IEEE754 format, (non-)equidistant, to decode the data. A final validation at the end of each data decompression was conducted to ensure data quality[2].

3.5 Fokker 100 Stall Data

All data can be extracted from the database using a Structured Query Language (SQL) query. Initially, 303 out of 617 stall recordings excluded information on landing gear position during the stall maneuver and were unusable for modeling purposes. A classification of To Be Determined (TBD) was assigned to a stall maneuver when this landing gear setting was applicable. The chief engineer at Fokker Services provided the necessary documents to determine the landing gear settings for all 303 stall recordings. An increase in model validity could be achieved when these parameters are available. An overview of all recordings with missing landing gear parameters was obtained using `MATLAB`, which was later exported to a `MICROSOFT EXCEL` file[3]. A manual check of all obtained testkaarten was used to manually update all 303 stall recordings accordingly. A reversed procedure was used to update the stall recordings in the database. All stall recordings now have a landing gear classification.

[2] A full overview of data decompression is given in the *'TE-2545-MRVS Archive.pdf'*-file at Fokker Services
[3] The file can be found in `'./STALL TASK FORCE/Fokker [NDA]/testkaarten/MissingLandingGear.xls'`

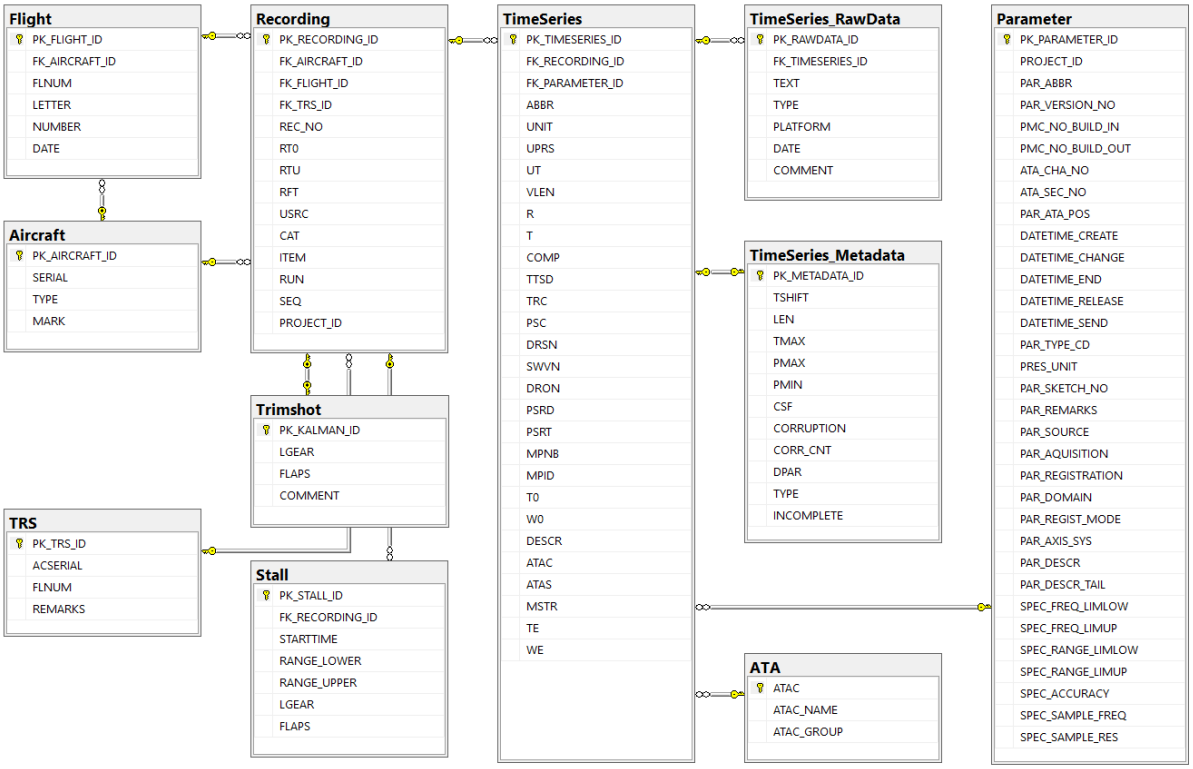

Figure 3.2: An overview of the Microsoft SQL database structure.

Although the data set of stall recordings included 617 stall maneuvers, not all stall recording are usable for modeling purposes. For example, missing sample values in input parameters in the STB process may lead to a gap in the output parameter, which are indicated logged in the table *'TimeSeries_Metadata'* in the correction count (CORR_CNT) list. If a parameter in a stall recording has a correction count greater than zero, this recording is omitted. A correction count of zero is chosen as sufficient stall recordings remain for buffet modeling purposes.

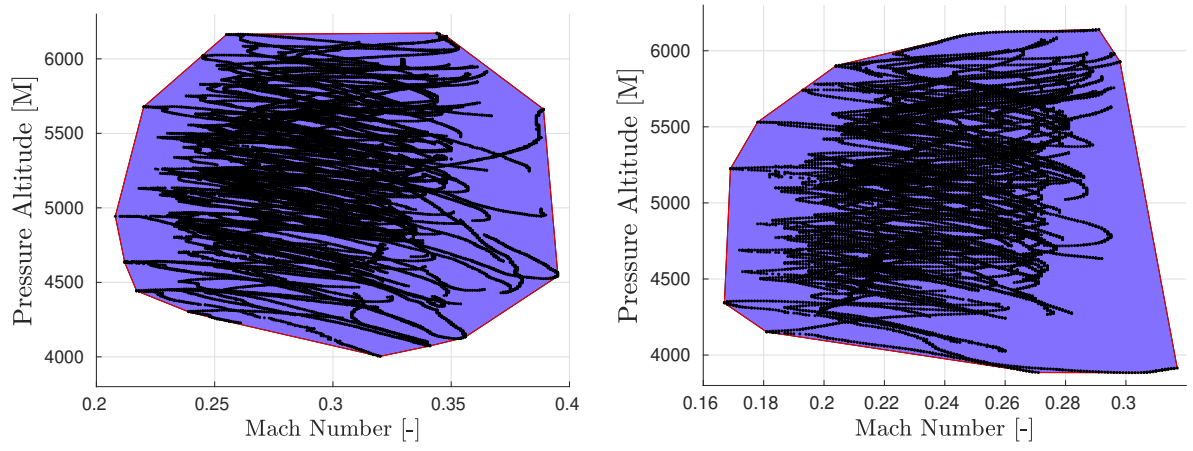

(a) Flight envelope in **clean configuration** (N=100).

(b) Flight envelope in **landing configuration** (N=99).

Figure 3.3: Flight envelope in clean and landing configuration in terms of pressure altitude and mach number.

Buffet effects are dependent on flight conditions, maneuvers, and aeroelastic aircraft characteristics [57]. The buffet intensity and frequency in a certain flight condition depend on the angle of attack, control surface deflections and dynamic pressure [57]. Therefore, two flight conditions were chosen which are

idling stalls in a clean configuration and idling stalls in landing configuration. Both conditions are also chosen in order to compare results from the Citation buffet model. The clean configuration is defined as the landing gear in the 'UP' position and flaps $0°$ whereas a landing configuration is defined as the landing gear in the 'DOWN' position and flaps $42°$. An overview of both conditions as well as the number of recordings can be seen in Figure 3.3.

For both aircraft configurations, the pressure altitude lies approximately between $4,000$ and $6,000$ meters. In the work of [18], it was assumed that the effect of altitude on the buffet was negligible. However, at Desdemona, a generic aircraft model was used which scaled the buffet with altitude. In the model, a scaling factor of 1.00 was applied up to a pressure altitude of $5,000$. The scaling factor was linearly interpolated from 1.00 to 0.45 for the altitudes ranging from $5,000$ to $8,000$ meter. Altitudes above $8,000$ meter are extrapolated with a scaling factor of 0.45. Therefore, the flight envelope is further divided based on pressure altitude. This division is based on previous work and the model of Desdemona and chosen to be $5,000$ meters and below, between $5,000$ and $5,500$ meters and above $5,500$ meters.

Further inspection of the flight data revealed vibrations measured at other locations instead of the IRS which is located close to the center of gravity. In several test flights, accelerometers were mounted close to the pilot seats. These vibration measurements can be used to simulate the perceived buffeting from the pilots perspective.

3.6 Cessna Citation Stall Data

To resemble flight test maneuvers of the Fokker 100, test flights with the Cessna Citation were flown. A detailed set of characteristics of the Cessna Citation can be found in the work of van Ingen [17] and van Horssen [18]. In Table 3.3 the maneuvers were flown to resemble the data from Fokker can be seen. Each flight condition was flown in sets of five. On the first day, a total of eighteen maneuvers were flown of which three were used as a so-called test stall. The last day, twenty additionally stalls were flown, also in sets of five. Additionally, an iPhone was used to measure the vibrations close to the pilot seats, as it was taped onto the bottom of the pedestal, which will be used to match the data of Fokker. An iPhone was chosen due to time constraints, simplicity of installation, short term availability and compatibility with the Delft University Environment for Communication and Activation (DUECA) system, which is the system that logs the data. A disadvantage of the iPhone is the low update frequency and the noisiness of the measured signal.

Table 3.3: Flight test manoeuvres flown with the Cessna Citation.

Date	Set	Manoeuvre	Altitude	Flaps	Gear	dV/dt	Inputs
03/12/2018	1	Clean (5x)	16,000 ft	$0°$	UP	1 $\frac{kts}{s}$	VAR
	2	Clean (5x)	16,000 ft	$0°$	UP	3 $\frac{kts}{s}$	VAR
	3	Flaps (5x)	16,000 ft	$40°$	UP	1 $\frac{kts}{s}$	VAR
05/12/2018	4	Clean (5x)	13,000 ft	$0°$	UP	1 $\frac{kts}{s}$	NONE
	5	Clean (5x)	13,000 ft	$0°$	UP	3 $\frac{kts}{s}$	NONE
	6	Flaps (5x)	13,000 ft	$40°$	UP	3 $\frac{kts}{s}$	VAR
	7	FlapsGear (5x)	13,000 ft	$40°$	DOWN	1 $\frac{kts}{s}$	VAR

In Table 3.3 the inputs are given as 'VAR' or 'NONE'. A 'NONE' input is when the pilots do not give any inputs when in the stall and try to stall the aircraft for three to five seconds. A 'VAR' input is a quasi-random input or wiggle input as defined by [17], on the pitch and roll channels.

Chapter 4

Preliminary Results

In this chapter all current preliminary results can be found. In section 4.1 an analysis on the buffet at the IRS location is conducted, whereas section 4.2 covers the buffet analysis at the pilot seat. In section 4.3 the data pre-processing of the measured parameters is conducted. In section 4.4 the X-parameters are estimated using the measured parameters from section 4.5. Lastly, the Fokker data is applied to the Cessna stall buffet model and a first time series is shown.

4.1 Buffet Analysis for the Fokker 100

As a baseline, the model of van Horssen [18] was used and therefore a PSD was made for each flight condition is made for the Fokker as well. In this case, a periodogram is made using `MATLAB` as this is the best available estimate of the discrete-time power spectral density. A stall recording is converted from the time domain to the frequency domain using the periodogram. A better estimate of the periodogram is obtained when two preparatory steps are conducted. First of all, the data has been removed from linear trends using `MATLAB`s `detrend` function. A detrend procedure is required as this increase the approximation. Usually, detrending affects lower frequencies, therefore, it should not pose any problems. Secondly, a Hanning window is used to smooth the periodogram.

In order to be able to compare the results for each periodogram the linear interpolation method `interp1` in `MATLAB` is used. In this case, the returned vector contains interpolated values at the specified frequency range set from minus maximum sample frequency to maximum sample frequency with a frequency step equal to the frequency resolution. Lastly, an average over N recordings and thus N periodograms is made using the `nanmean` function in `MATLAB`, which omits NaN values from the calculation.

In the figures below a similar layout is preserved. Each row represents an altitude change, which means that the top row is the low altitudes, the middle row entails the medium altitudes and the bottom row entails the higher altitudes of the flight envelope. Each column indicates the aircraft configuration, thus the first column represents the periodogram for all clean configurations and the second one the landing configurations. In each subfigure title, the number of recordings to create the periodogram can be seen between brackets. Figure 4.1, Figure 4.2, Figure 4.3 show the periodogram in longitudinal, lateral and vertical direction respectively. As for buffet comparison, each figure has equal limits on its axis except Figure 4.2, which has been changed due to better graphical representation. As mentioned in section 3.5 the intensity of the buffet decreases as the altitude increases which is also clearly visible in the figures below, especially for the aircraft in the clean configuration.

Buffet in Longitudinal Direction

In the longitudinal direction, a strong peak at approximately 5 Hertz is noticeable in all configurations as can be seen in Figure 4.1. An aircraft stalling in clean configuration has a broad spectrum up to 15 Hertz containing power with peaks at seven, nine and thirteen Hertz. In a landing configuration, the

spectrum is less broad and a large peak at 5 Hertz is clearly visible in all subplots.

Buffet in Lateral Direction

As for the buffet in the lateral direction, peaks occur at lower frequencies and at approximately 10 Hertz power goes to zero. Similarly to the longitudinal direction a peak at 4 Hertz occurs, however a larger peak is observed at 2 Hertz. An interaction between the fuselage and vertical stabilizer inducing different bending and torsion modes of the aircraft are the main contribution to the different peaks observed in each periodogram. The intensity of the buffet in the lateral direction is ten times higher as compared to the buffet in the longitudinal direction. Compared to the Cessna Citation, as seen in Figure 2.10, the lateral buffet is present at lower frequencies.

Buffet in Vertical Direction

Lastly, the most important buffet component or at least the buffet component which is largest in intensity. A factor ten larger than the buffet in the lateral direction and a factor hundred larger compared to the buffet in the longitudinal direction. Similarly, a strong peak is visible for the vertical buffet at approximately 5 Hertz. Additional, but weaker peaks are visible at 8 Hertz. In comparison to the Cessna Citation, these peaks are equal in intensity but unequal in frequency. As the Fokker 100 is a larger aircraft and a, therefore, slower adaptability to changes the frequencies are lower when compared to the smaller Cessna. However, equality in peak intensity can be attributed to the distance to the center of gravity. The main contribution to these modes could be due to the flow separation over the wing and the interaction between the separated flow and the horizontal stabilizer.

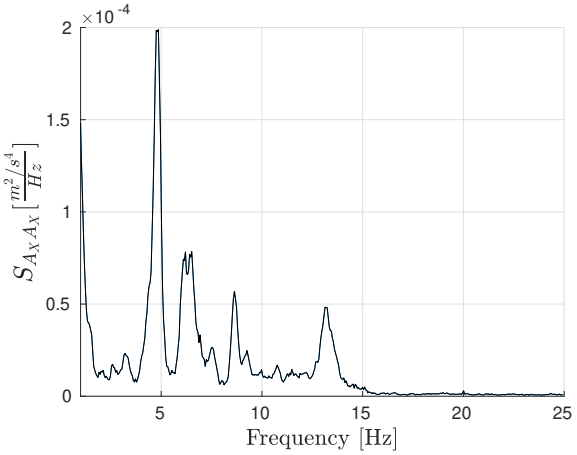

(a) Periodogram in **longitudinal direction** for altitudes below **5,000** meter in **clean configuration** (N=22).

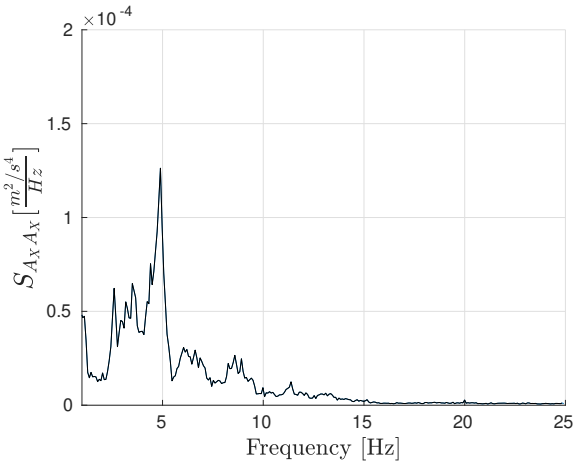

(b) Periodogram in **longitudinal direction** for altitudes below **5,000** meter in **landing configuration** (N=31).

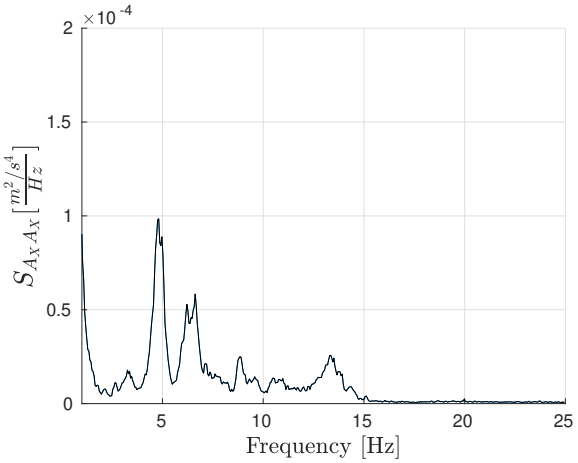

(c) Periodogram in **longitudinal direction** for altitudes between **5,000** and **5,500** meter in **clean configuration** (N=28).

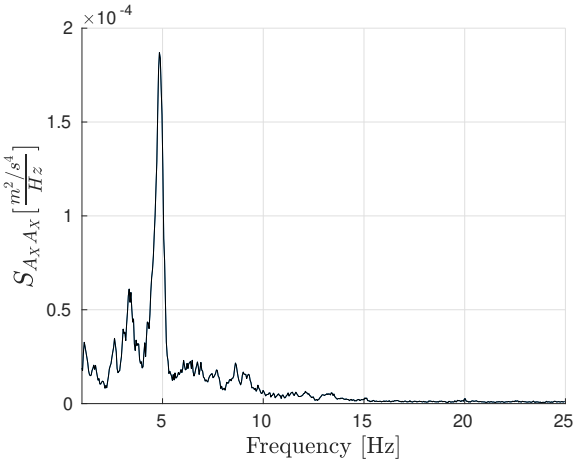

(d) Periodogram in **longitudinal direction** for altitudes between **5,000** and **5,500** meter in **landing configuration** (N=27)

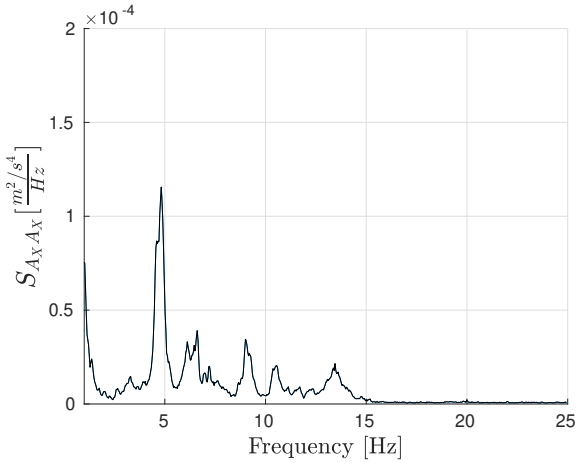

(e) Periodogram in **longitudinal direction** for altitudes above **5,500** meter in **clean configuration** (N=29).

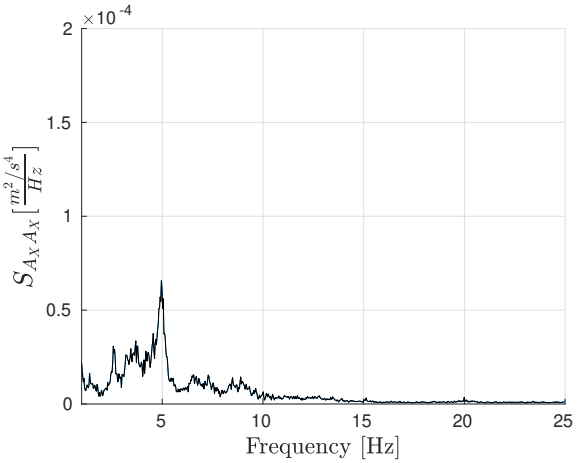

(f) Periodogram in **longitudinal direction** for altitudes above **5,500** meter in **landing configuration** (N=20)

Figure 4.1: Periodogram in longitudinal direction for altitudes between 4,000 and 6,000 meter in both clean and landing configuration.

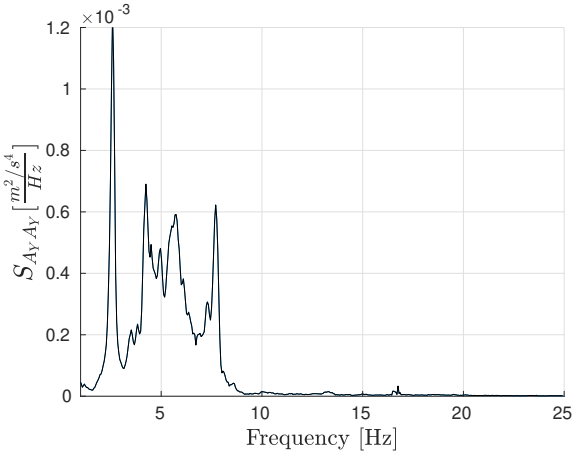

(a) Periodogram in **lateral direction** for altitudes below **5,000** meter in **clean configuration** (N=22).

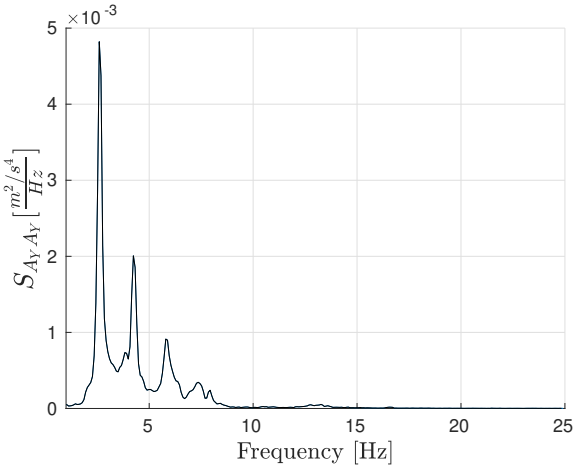

(b) Periodogram in **lateral direction** for altitudes below **5,000** meter in **landing configuration** (N=31).

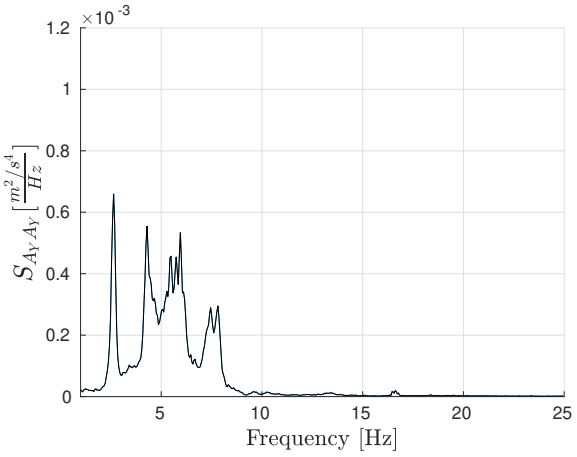

(c) Periodogram in **lateral direction** for altitudes between **5,000** and **5,500** meter in **clean configuration** (N=28).

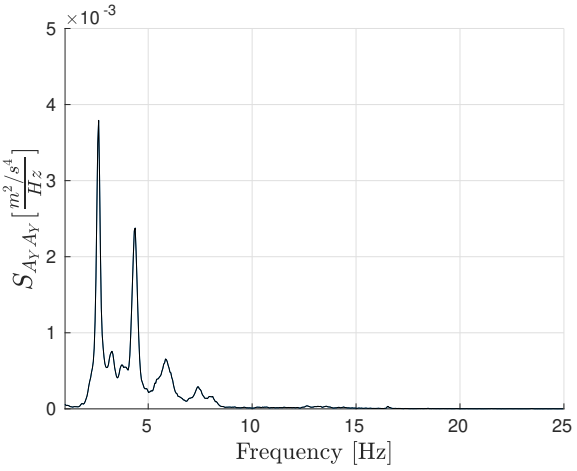

(d) Periodogram in **lateral direction** for altitudes between **5,000** and **5,500** meter in **landing configuration** (N=27)

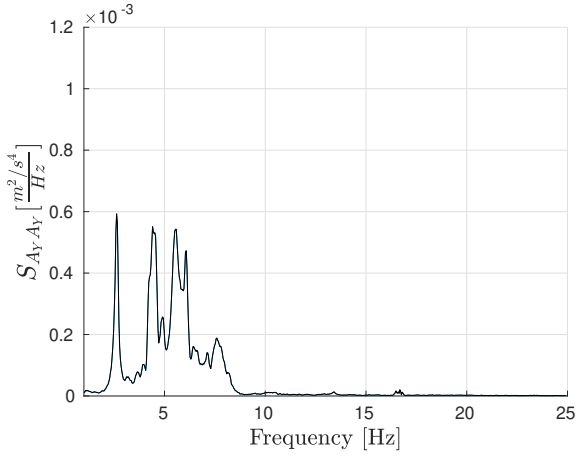

(e) Periodogram in **lateral direction** for altitudes above **5,500** meter in **clean configuration** (N=29).

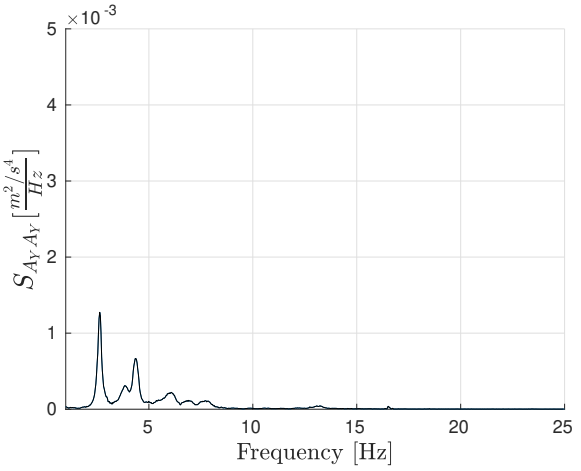

(f) Periodogram in **lateral direction** for altitudes above **5,500** meter in **landing configuration** (N=20)

Figure 4.2: Periodogram in lateral direction for altitudes between 4,000 and 6,000 meter in both clean and landing configuration.

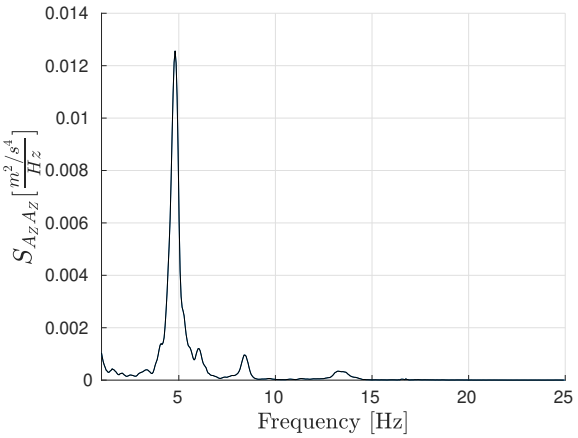

(a) Periodogram in **vertical direction** for altitudes below **5,000** meter in **clean configuration** (N=22).

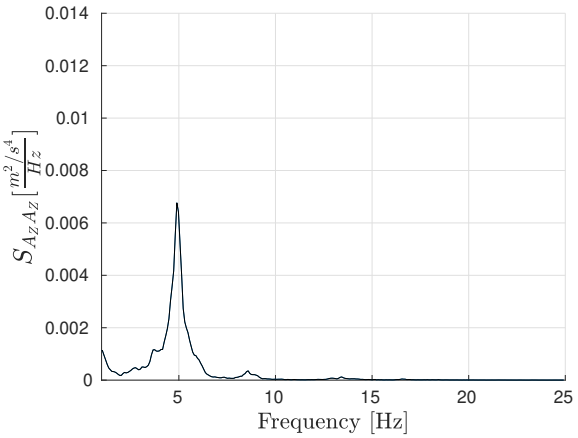

(b) Periodogram in **vertical direction** for altitudes below **5,000** meter in **landing configuration** (N=31).

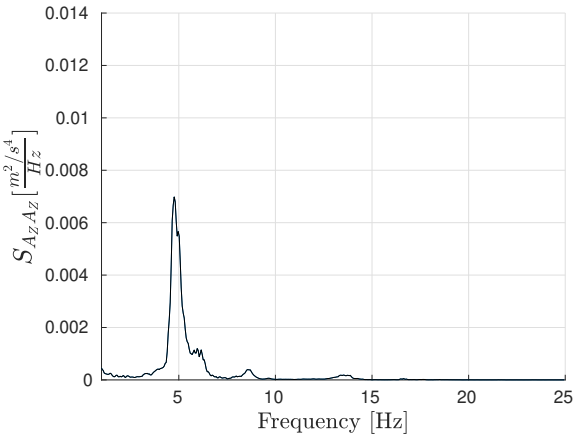

(c) Periodogram in **vertical direction** for altitudes between **5,000** and **5,500** meter in **clean configuration** (N=28).

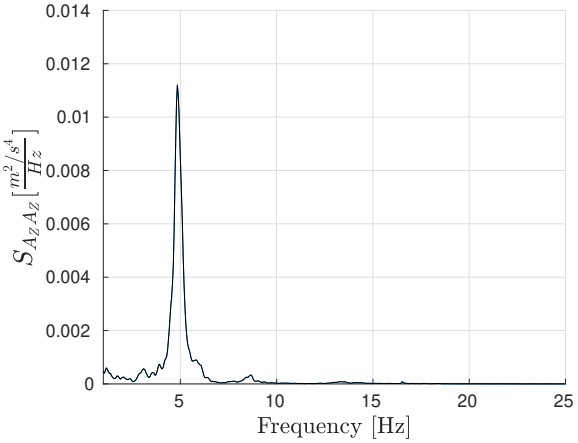

(d) Periodogram in **vertical direction** for altitudes between **5,000** and **5,500** meter in **landing configuration** (N=27)

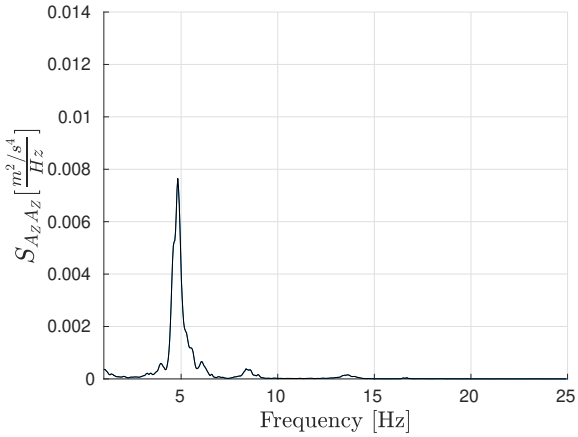

(e) Periodogram in **vertical direction** for altitudes between above **5,500** meter in **clean configuration** (N=29).

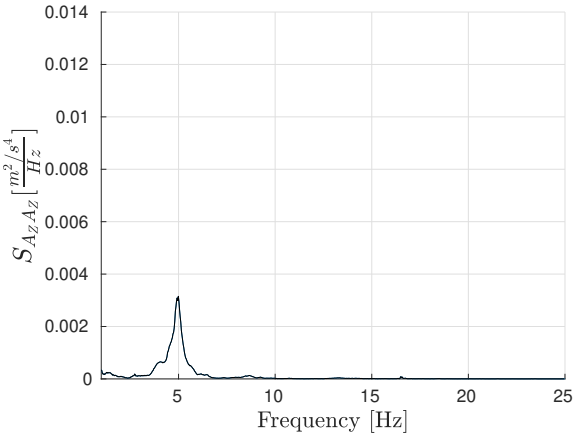

(f) Periodogram in **vertical direction** for altitudes above **5,500** meter in **landing configuration** (N=20)

Figure 4.3: Periodogram in vertical direction for altitudes between 4,000 and 6,000 meter in both clean and landing configuration.

4.2 Pilot Seat Vibrations

Although, buffet modeling based on the measured IRS data in each stall test flight may be sufficient. In this section, an extension is made to acquire more insight into the effect of the position within the aircraft relative to the center of gravity. An advantage of the flight test data are the recordings which contain accelerometer measurements at the pilot seat, which indicates the buffeting effects as observed and felt by the pilots. A common deficiency mentioned SME was the insufficient buffet feedback, in terms of intensity, in aircraft models based on accelerometer data close to the center of gravity.

Therefore, recordings containing these accelerometers under the pilot seat are extracted from the database. Similarly, recordings with a correction count greater than zero are again omitted from the data. A different data set is used compared to the previous section as not all recordings include pilot seat accelerometer data. Additionally, only the accelerations in the lateral and vertical direction were measured in these recordings.

In each of the figures below a similar layout is preserved. A similar approach is used as in Figure 4.1, Figure 4.2 and Figure 4.3, which means that each row represents a different altitude and each column indicates the accelerometer location. In the column on the left all periodograms at the IRS location are shown and the column on the right all periodograms at the pilot seat location are shown. Also, the number of recordings can be seen in between brackets in the subfigure title. Figure 4.4 and Figure 4.5 contain the information on the aircraft buffet in the lateral direction for the aircraft in clean and landing configuration respectively, whereas Figure 4.6 and Figure 4.7 represent the information for the buffet in vertical direction.

4.2.1 Fokker 100 Buffet in Lateral Direction

The buffet in the lateral direction at the pilot seat and IRS can be obtained for aircraft in the clean configuration from Figure 4.4 and for aircraft in the landing configuration in Figure 4.5. In both figures a noticeable difference can be seen, as the accelerations at the pilot seat are at lower frequencies with higher intensity compared to the accelerations at the IRS, where the peak occurs at approximately 1 Hertz. On closer inspection similar peaks in the data can be seen at 3 and 5 Hertz for both accelerometer locations, however, the intensity differs due to the larger peaks at lower frequencies. The general trend of decreased intensity with increased altitude remains for both accelerometer locations.

4.2.2 Fokker 100 Buffet in Vertical Direction

In Figure 4.6 and Figure 4.7 similar effects as in lateral direction can be seen. At the pilot seat, the accelerations occur at lower frequencies with higher intensity. In a clean configuration, the peak frequencies occur at 0.5 Hertz, with several smaller peaks occurring at 1.8, 3 and 5 Hertz. Aircraft buffet when in the landing configuration has a lower intensity at these frequencies.

A remarkable effect in the pictures can be observed when the location of the accelerometer is changed from close the center of gravity to further away from the center of gravity, i.e. moving the accelerometer from the IRS to the pilot seat. Normally, in aerodynamic stall modeling aircraft structures are assumed to be rigid, however, these plots show a response of a nonrigid structure. It may well be that the induced vibrations on the wings and stabilizer induce effects at lower frequencies further away from the center of gravity. Additionally, an increased arm causes a larger vibration and thus an increase in buffet intensity, which is also clearly visible.

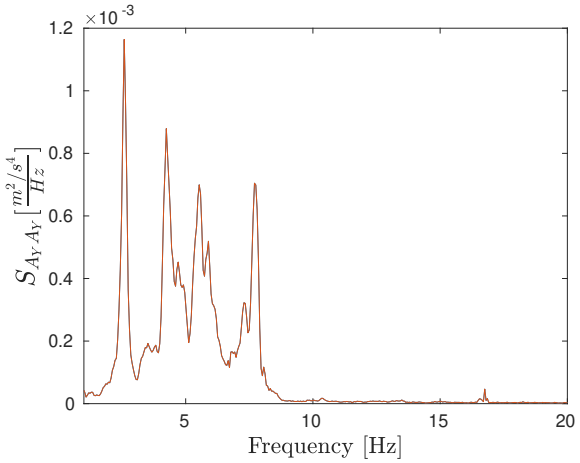

(a) Periodogram in **lateral direction** for altitudes between **4,000** and **5,000** meter in **clean configuration** at the IRS location (N=17).

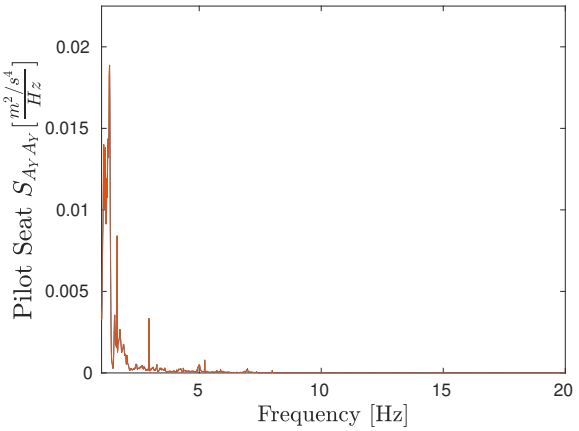

(b) Periodogram in **lateral direction** for altitudes between **4,000** and **5,000** meter in **clean configuration** at the pilot seat location (N=17).

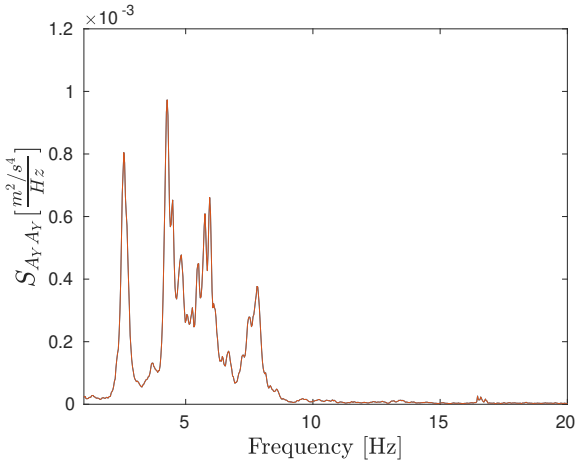

(c) Periodogram in **lateral direction** for altitudes between **5,000** and **5,500** meter in **clean configuration** at the IRS location (N=18).

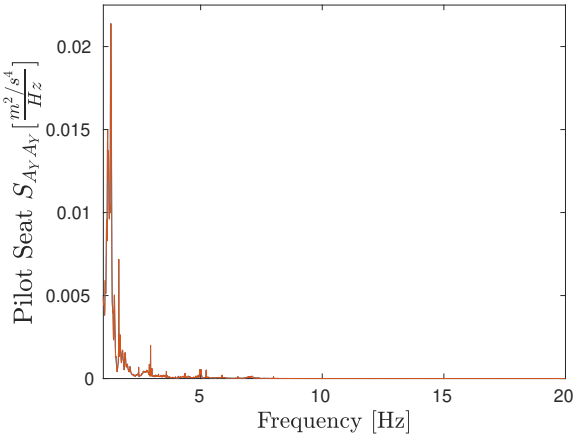

(d) Periodogram in **lateral direction** for altitudes between **5,000** and **5,500** meter in **clean configuration** at the pilot seat location (N=18).

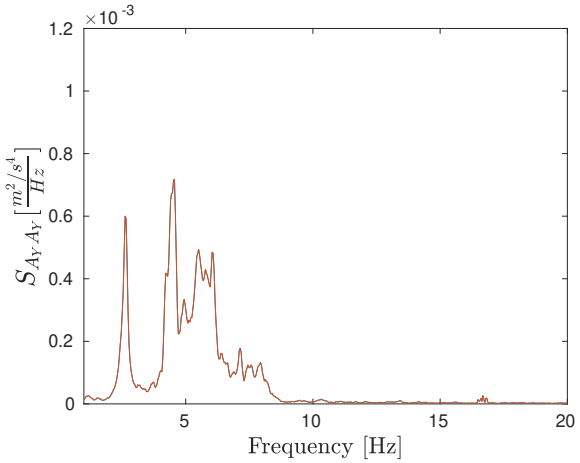

(e) Periodogram in **lateral direction** for altitudes between **5,500** and **6,000** meter in **clean configuration** at the IRS location (N=19).

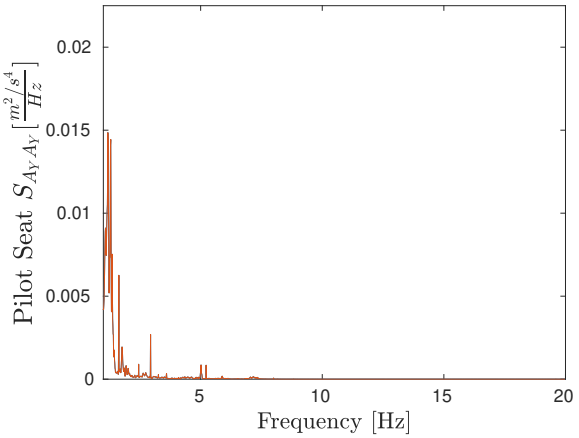

(f) Periodogram in **lateral direction** for altitudes between **5,500** and **6,000** meter in **clean configuration** at the pilot seat location (N=19).

Figure 4.4: Periodogram in lateral direction for altitudes between 4,000 and 6,000 meter in clean configuration for the accelerometers located at the pilot seat and IRS.

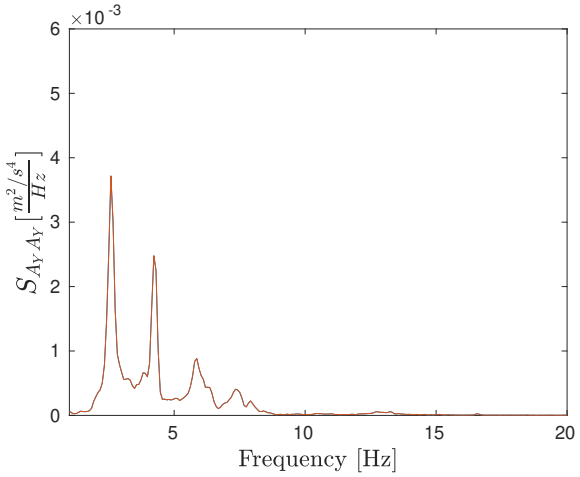

(a) Periodogram in **lateral direction** for altitudes between **4,000** and **5,000** meter in **landing configuration** at the IRS location (N=24).

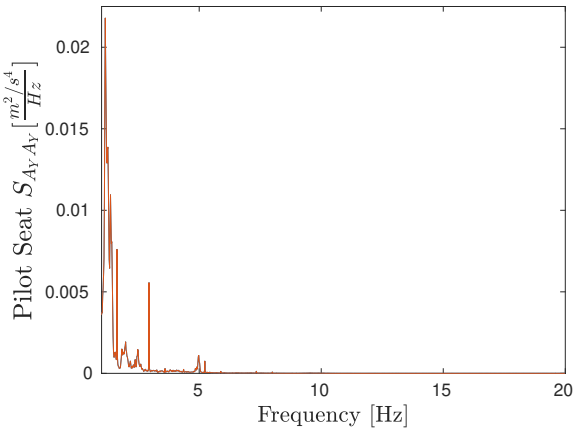

(b) Periodogram in **lateral direction** for altitudes between **4,000** and **5,000** meter in **landing configuration** at the pilot seat location (N=24).

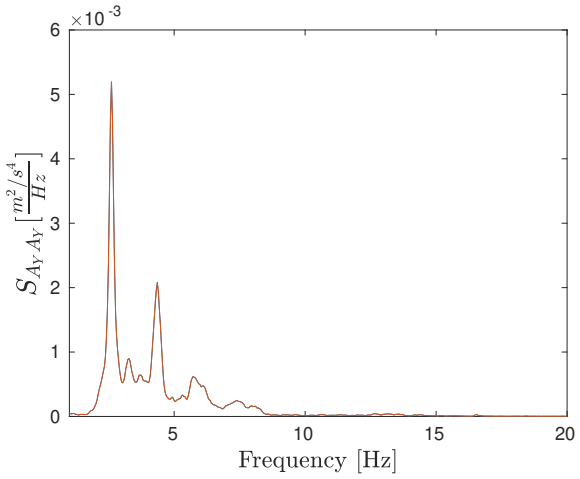

(c) Periodogram in **lateral direction** for altitudes between **5,000** and **5,500** meter in **landing configuration** at the IRS location (N=20).

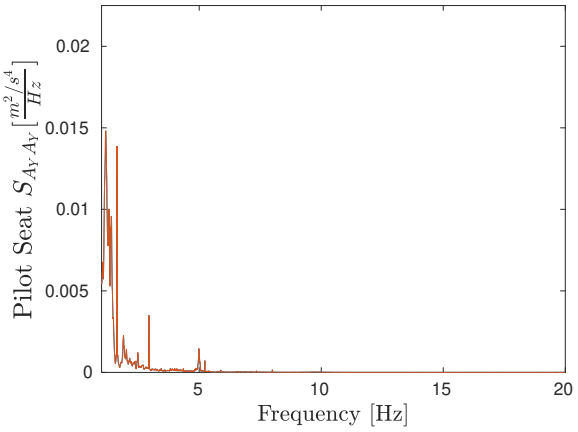

(d) Periodogram in **lateral direction** for altitudes between **5,000** and **5,500** meter in **landing configuration** at the pilot seat location (N=20).

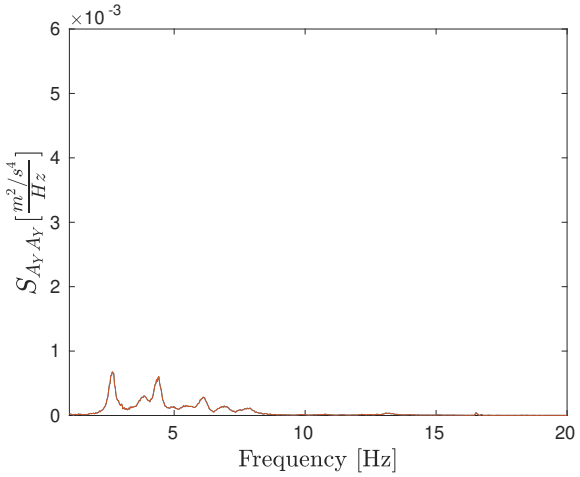

(e) Periodogram in **lateral direction** for altitudes between **5,500** and **6,000** meter in **landing configuration** at the IRS location (N=15).

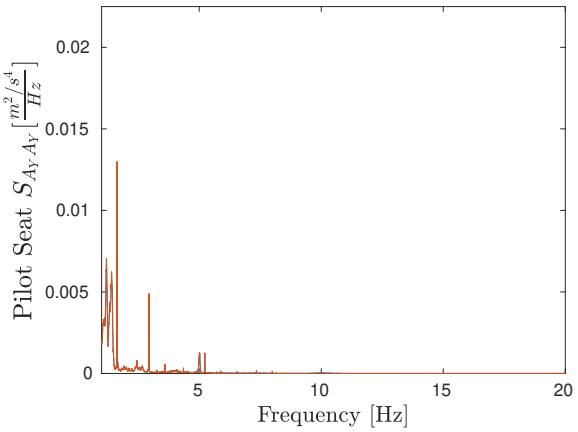

(f) Periodogram in **lateral direction** for altitudes between **5,500** and **6,000** meter in **landing configuration** at the pilot seat location (N=15).

Figure 4.5: Periodogram in lateral direction for altitudes between 4,000 and 6,000 meter in landing configuration for the accelerometers located at the pilot seat and IRS.

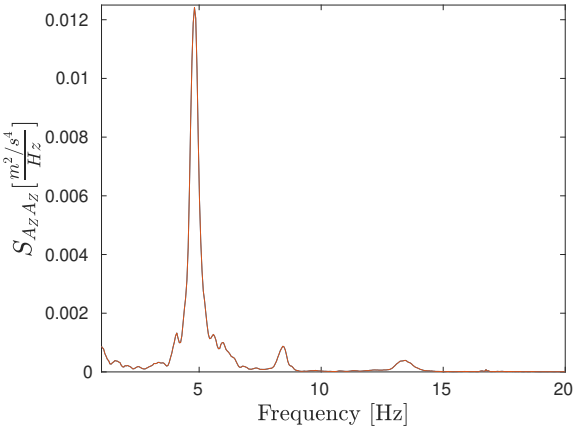

(a) Periodogram in **vertical direction** for altitudes between **4,000** and **5,000** meter in **clean configuration** at the IRS location (N=16).

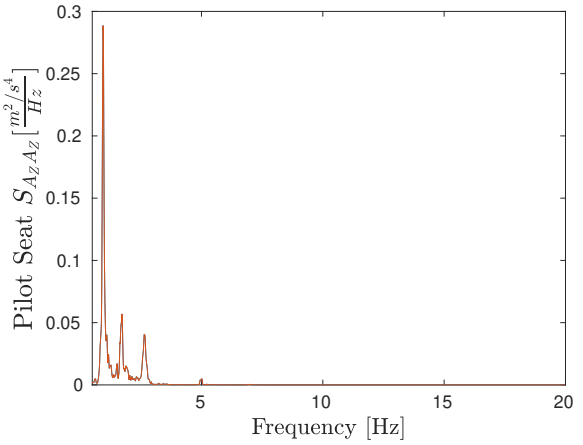

(b) Periodogram in **vertical direction** for altitudes between **4,000** and **5,000** meter in **clean configuration** at the pilot seat location (N=16).

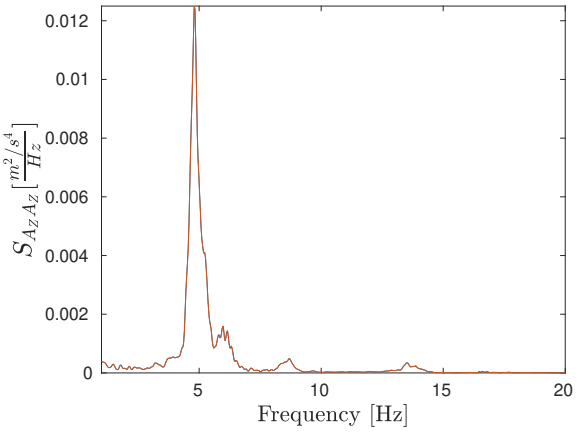

(c) Periodogram in **vertical direction** for altitudes between **5,000** and **5,500** meter in **clean configuration** at the IRS location (N=19).

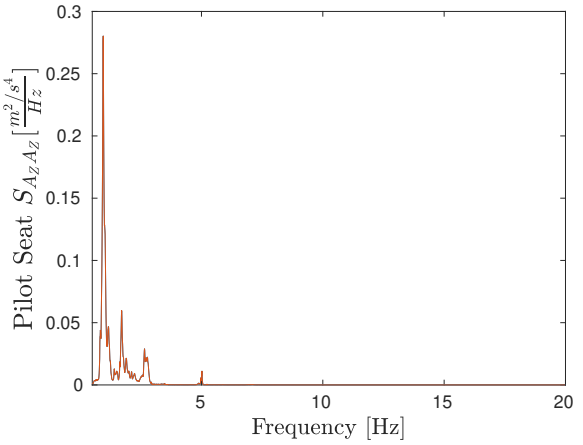

(d) Periodogram in **vertical direction** for altitudes between **5,000** and **5,500** meter in **clean configuration** at the pilot seat location (N=19).

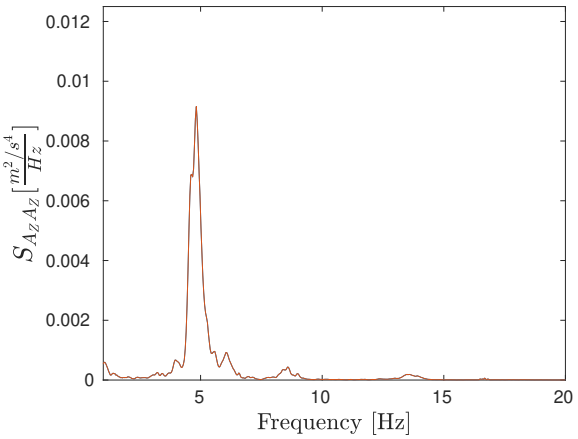

(e) Periodogram in **vertical direction** for altitudes between **5,500** and **6,000** meter in **clean configuration** at the IRS location (N=18).

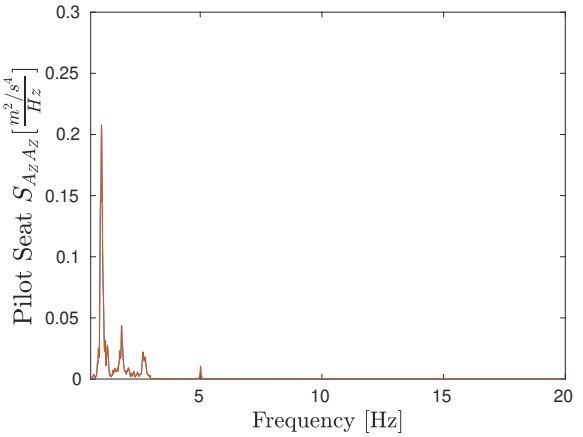

(f) Periodogram in **vertical direction** for altitudes between **5,500** and **6,000** meter in **clean configuration** at the pilot seat location (N=18).

Figure 4.6: Periodogram in vertical direction for altitudes between 4,000 and 6,000 meter in clean configuration for the accelerometers located at the pilot seat and IRS.

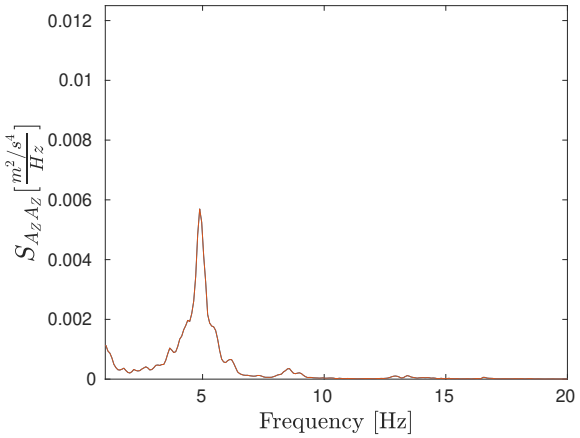

(a) Periodogram in **vertical direction** for altitudes between **4,000** and **5,000** meter in **landing configuration** at the IRS location (N=16).

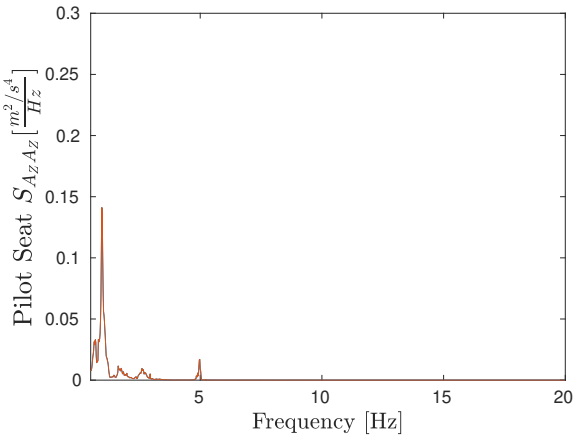

(b) Periodogram in **vertical direction** for altitudes between **4,000** and **5,000** meter in **landing configuration** at the pilot seat location (N=16).

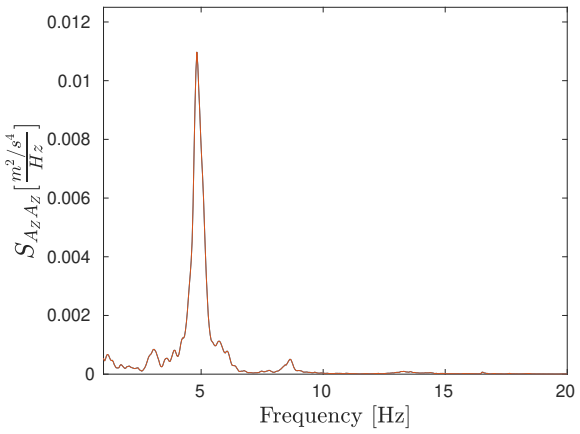

(c) Periodogram in **vertical direction** for altitudes between **5,000** and **5,500** meter in **landing configuration** at the IRS location (N=19).

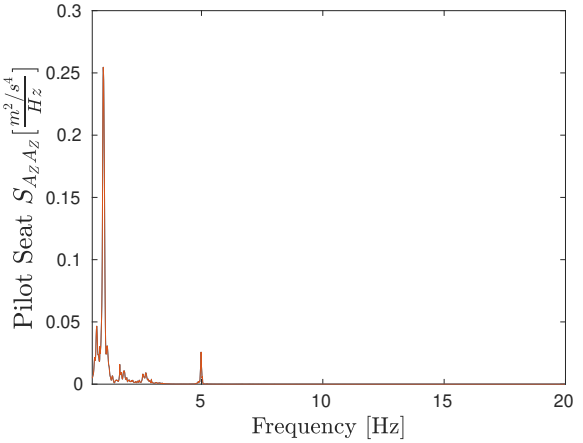

(d) Periodogram in **vertical direction** for altitudes between **5,000** and **5,500** meter in **landing configuration** at the pilot seat location (N=19).

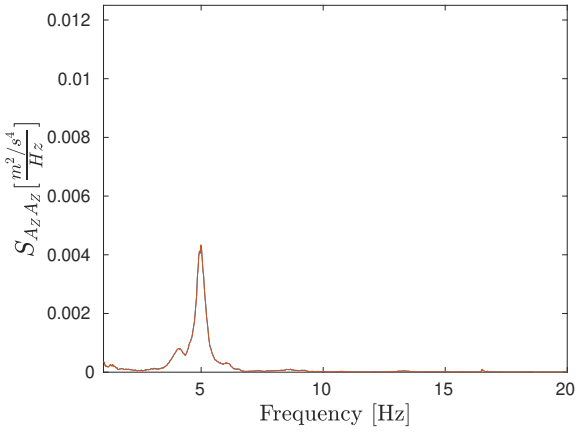

(e) Periodogram in **vertical direction** for altitudes between **5,500** and **6,000** meter in **landing configuration** at the IRS location (N=18).

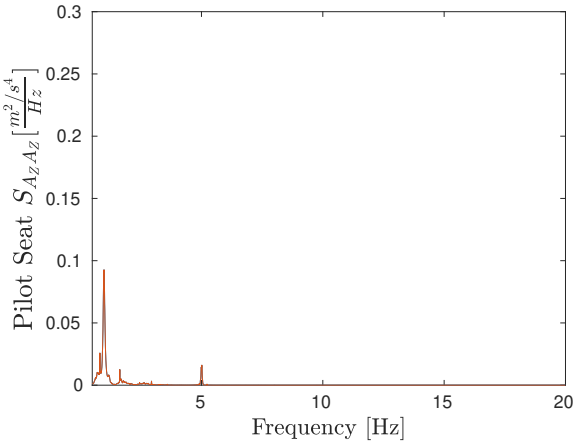

(f) Periodogram in **vertical direction** for altitudes between **5,500** and **6,000** meter in **landing configuration** at the pilot seat location (N=18).

Figure 4.7: Periodogram in vertical direction for altitudes between 4,000 and 6,000 meter in landing configuration for the accelerometers located at the pilot seat and IRS.

4.2.3 Cessna Citation Buffet at Pilot Seat

In Figure 4.8 the acceleration measurements from the iPhone can be seen. Despite the noisiness of the signal a clear peak in the vertical direction can be seen at approximately 14 Hertz, which is quite similar to the result shown in Figure 2.10. Also two peaks in the lateral direction indicate a similar result, however these are located at higher frequencies.

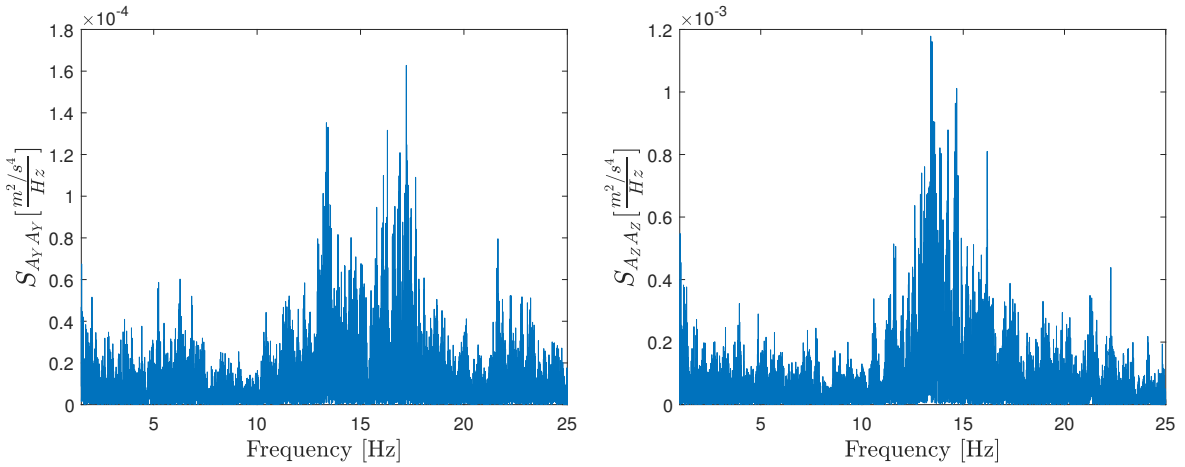

(a) Periodogram in **lateral direction** at **5,000** meter in **clean configuration** at pilot seat (N=10).

(b) Periodogram in **vertical direction** at **5,000** meter in **clean configuration** at pilot seat (N=10).

Figure 4.8: Periodogram in lateral and vertical direction at 5,000 meter in clean configuration for the iPhone accelerometers located at the pilot seat.

4.3 Data Pre-Processing

A few preparatory steps have to be conducted before a buffet model can be created. First of all, the measured data contains measurement and process noises which have to be filtered out, which is covered in subsection 4.3.1. Secondly, for each recording, a common time step is applied using an interpolation procedure which is the topic of subsection 4.3.2.

4.3.1 Data Filtering

As already mentioned in section 3.2 some parameters are measured and others are calculated with the formulas according to Fokker Report DAS-100-012. To model the buffet, the following parameters are required which are the body accelerations (A_X, A_Y and A_Z), the angle of attack (α), the lift coefficient C_L and the rate of change of angle of attack ($\dot{\alpha}$). However, these calculations are based on the best-estimated parameters without noise, thus a filter is required. Therefore, a fourth-order Butterworth filter with a zero-order hold is used to filter the data. Butterworth filters are commonly used in signal processing as passband of the filter is maximally flat, which is traded for a less steep roll-off after the cut-off frequency. A fourth-order Butterworth filter with a half-power frequency (-3 dB) at 3 Hertz is used and is shown in Figure 4.9. The half power-frequency is set at 3 Hertz as the buffet component in vertical direction for the Fokker 100 has its main power at 5 Hertz.

4.3.2 Data Interpolation

After filtering the data there still remain irregularities in the data sizes, which requires resampling of the data for which the `interp1` function in `MATLAB` is used. In Algorithm 1 the pseudocode for this interpolation procedure is given for each stall parameter.

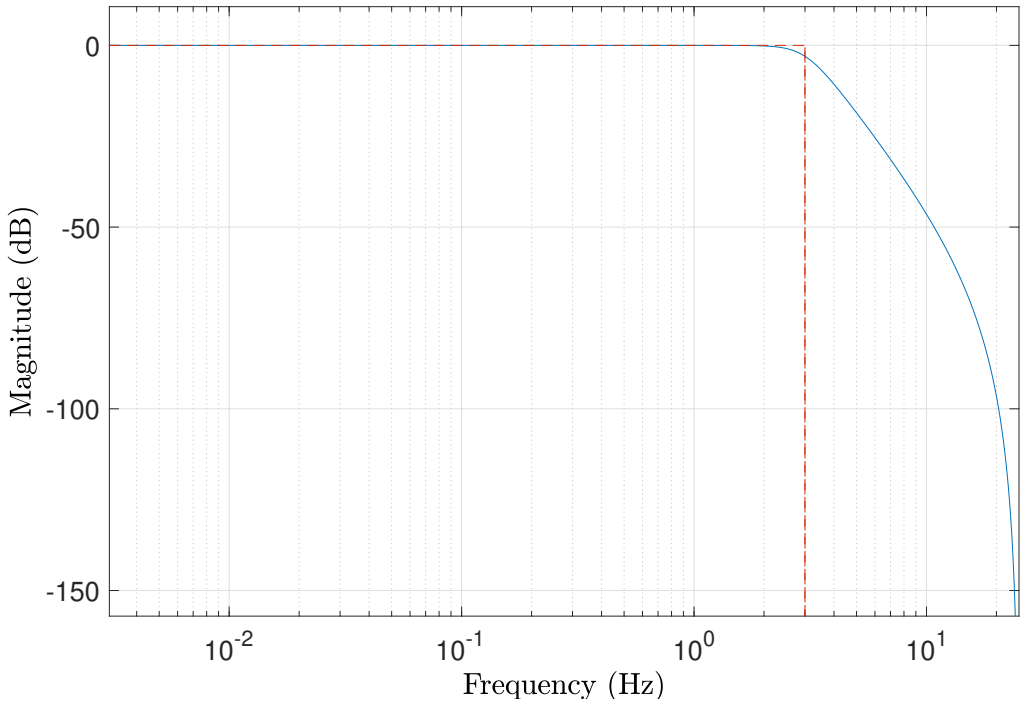

Figure 4.9: Magnitude response of a fourth order Butterworth filter with a half power frequency at 3 Hertz.

Algorithm 1 Pseudocode for stall data interpolation

Inputs:
  α: angle of attack
  $\dot{\alpha}$: rate of change of angle of attack
  C_L: lift coefficient
  A_X: body acceleration in x-direction
  A_Y: body acceleration in y-direction
  A_Z: body acceleration in z-direction
Initialize:
  $F_S \leftarrow 50$ [Hz] (sample frequency)
  dt $\leftarrow 1/F_S$ [s] (time step)
Procedures:
  for All Stall Recordings **do**
    $t_{START} \leftarrow$ `maximum`($\alpha_{t=1}$, $\dot{\alpha}_{t=1}$, $C_{L,t=1}$, $A_{X,t=1}$, $A_{Y,t=1}$, $A_{Z,t=1}$)
    $t_{END} \leftarrow$ `minimum`($\alpha_{t=end}$, $\dot{\alpha}_{t=end}$, $C_{L,t=end}$, $A_{X,t=end}$, $A_{Y,t=end}$, $A_{Z,t=end}$)
    t $\leftarrow t_{START} : dt : t_{END}$
    $\alpha \leftarrow$ `interp1`(α_t, α, t)
    $\dot{\alpha} \leftarrow$ `interp1`($\dot{\alpha}_t$, $\dot{\alpha}$, t)
    $C_L \leftarrow$ `interp1`($C_{L,t}$, C_L, t)
    $A_X \leftarrow$ `interp1`($A_{X,T}$, A_X, t)
    $A_Y \leftarrow$ `interp1`($A_{Y,T}$, A_Y, t)
    $A_Z \leftarrow$ `interp1`($A_{Z,T}$, A_Z, t)
    if length states is unequal **then**throw error

4.4 Parameter Estimation

In this section, the current parameter estimation methods are covered used in the preliminary results. With parameter estimation techniques one tries to find the best parameter given for a model structure and data set, where minimizing a cost function by altering the parameters. When a cost function is

defined as a nonlinear function of the model parameters, linear parameter estimation can no longer be used and thus nonlinear parameter estimation techniques have to be used.

In MATLAB a nonlinear optimization toolbox is available, which contains multiple optimization algorithms. In the toolbox two, commonly used types of algorithms are gradient-based algorithms and gradient-free algorithms. As the name of the algorithm suggest one uses the gradient of the cost function with respect to the estimated parameter and the other does not. In MATLAB the gradient algorithms are the interior point, active set, Levenberg-Marquardt, Trust Region Reflective, Sequential Quadratic Programming, and the gradient-free algorithms are Nelder-Mead Simplex and Pattern Search. In the work of Nocedal [58] a more detailed background on these algorithms can be found. In this work, the fmincon function with the gradient-based algorithm called interior point is used as this function is able to limit the search space, i.e. parameter bounds could be given to constraint the problem.

For the parameter estimation the model functions are given by Equation 4.1:

$$\begin{aligned} \hat{C_L}(\alpha, \dot{\alpha}, \zeta) &= C_{L_0} + C_{L_\alpha}\left\{\frac{1+\sqrt{X}^2}{2}\right\}\alpha + C_{L_{\alpha^2}}(\alpha - 6^\circ)_+^2 \\ \tau_1 \frac{dX}{dt} + X &= \frac{1}{2}\cdot\Big\{1 - \tanh(a_1 \cdot (\alpha - \tau_2\dot{\alpha} - \alpha^*))\Big\} \end{aligned} \tag{4.1}$$

where the parameters to be estimated are ζ = [C_{L_0} C_{L_α} $C_{L_{\alpha^2}}$ τ_1 τ_2 a_1 α^*] and the cost function is given by:

$$\arg\min_{\zeta} J = (C_L - \hat{C_L}(\alpha, \dot{\alpha}, \zeta))'(C_L - \hat{C_L}(\alpha, \dot{\alpha}, \zeta)) \tag{4.2}$$

which was used trying to estimate the parameters. In this case, the model structure was based on C_L formula of van Ingen [17] as this model is the best current estimate. However, nonlinear parameter estimation techniques do not always converge to a global optimum but converge to a local minimum. Therefore, one solution was limiting the search space by setting lower and upper bounds on each parameter. Each bound is based on a physical assumption or on the previous work of van Ingen and van Horssen [17, 18]. An overview for each lower and upper bound is given in Table 4.1.

Table 4.1: Lower and upper bounds for the nonlinear optimization problem for each parameter.

Parameter (ζ)	C_{L_0}	C_{L_α}	$C_{L_{\alpha^2}}$	τ_1	τ_2	a_1	α^*
Lower bound	-2	0	-2	0.001	0	0	0
Upper bound	2	10	2	1	1	80	0.65

Additionally, the fmincon function was run multiple times with different initial conditions to optimize the performance and be sure to a global minimum was found. In the end, engineering judgment is still required to determine the best parameter estimates.

In this preliminary result, the model fit quality is evaluated based on the Mean Squared Error (MSE). In Table 4.2 an overview for each flight condition can be seen.

Table 4.2: X-Parameter estimates for each flight condition for the Fokker 100.

Altitude [m] (h)	Configuration	C_{L_0} [-]	C_{L_α} [-]	$C_{L_{\alpha^2}}$ [-]	τ_1 [s]	τ_2 [s]	a_1 [-]	α^* [rad]	MSE
h< 5,000	CLEAN	0.7220	2.0589	1.2369	0.9206	0.9256	57.9987	0.3957	0.1753
5,000 , h , 5,500	CLEAN	0.5816	2.8314	-0.2743	0.4964	0.5493	58.0811	0.3634	0.0431
h> 5,000	CLEAN	0.6068	2.6697	0.3089	0.6466	0.7326	52.8012	0.3636	0.1598
h< 5,000	LANDING	1.3597	3.3124	-1.1387	0.2205	0.8811	72.2436	0.3363	0.1809
5,000 < h < 5,500	LANDING	1.4328	2.6982	0.2835	0.4921	0.3183	44.4712	0.3353	0.2102
h> 5,000	LANDING	1.3680	2.7883	-0.0889	0.4412	0.3472	36.4568	0.2997	0.3511

As mentioned subsubsection 2.3.2.2 the buffet model for the Cessna Citation is based on fitting a frequency response function with a second-order low-pass filter on the data.

$$H(j\omega) = \frac{H_0\omega_0^2}{(j\omega)^2 + \frac{w_0}{Q_0}j\omega + \omega_0^2} \tag{4.3}$$

where the estimated parameters are ζ_2 =[H_0, ω_0, Q_0]. Frequency response is fitted using the `lsqnonlin` function using the Levenberg-Marquardt algorithm as this function is able to deal with nonlinear functions. In this case, the data for the Fokker 100 is fitted in a similar fashion as for the Cessna Citation. In Table 4.3 the values for each parameter, the unit and the Cramér–Rao Lower Bound (CRLB) is depicted. For the model fit the MSE was $2.6561e-14$ and the coefficient of determination (R^2) was 0.9752.

Table 4.3: Parameter estimates for the frequency response function.

Parameters (ζ_2)	[Unit]	Value	CRLB
H_0	[-]	0.0101	2.0976e-05
ω_0	[rad/s]	30.0886	2.5057e-03
Q_0	[-]	11.2794	2.2846e-04

A decent model fit was obtained as a high R^2 value in the combination with low CRLB values. In Figure 4.10 the frequency response can be seen for the Fokker 100 in the clean configuration for altitudes below 5,000 meter.

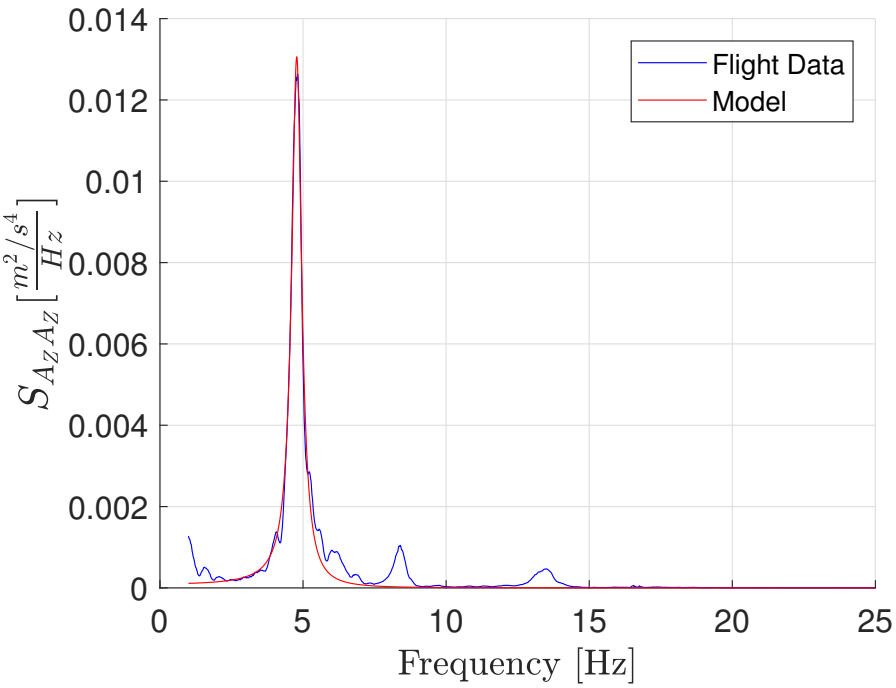

Figure 4.10: Periodogram for the fitted frequency response function in vertical direction for altitudes below 5,000 meter in clean configuration

4.5 Current Buffet Model on Fokker 100 Data

In this section, the results for the buffet model of the Cessna Citation, based on Figure 2.11, on the Fokker 100 data is shown. In terms of modeling and validation data an 80/20 rule is used, where 80% is used for creating the model and 20% is used to validate the model. However, only the result for one flight condition is shown here, which is the stall maneuvers below 5,000 meter and for the aircraft in the clean configuration. As the buffet model is fitted around the zero value, the buffet model output is added to the vertical acceleration and is depicted in Figure 4.11.

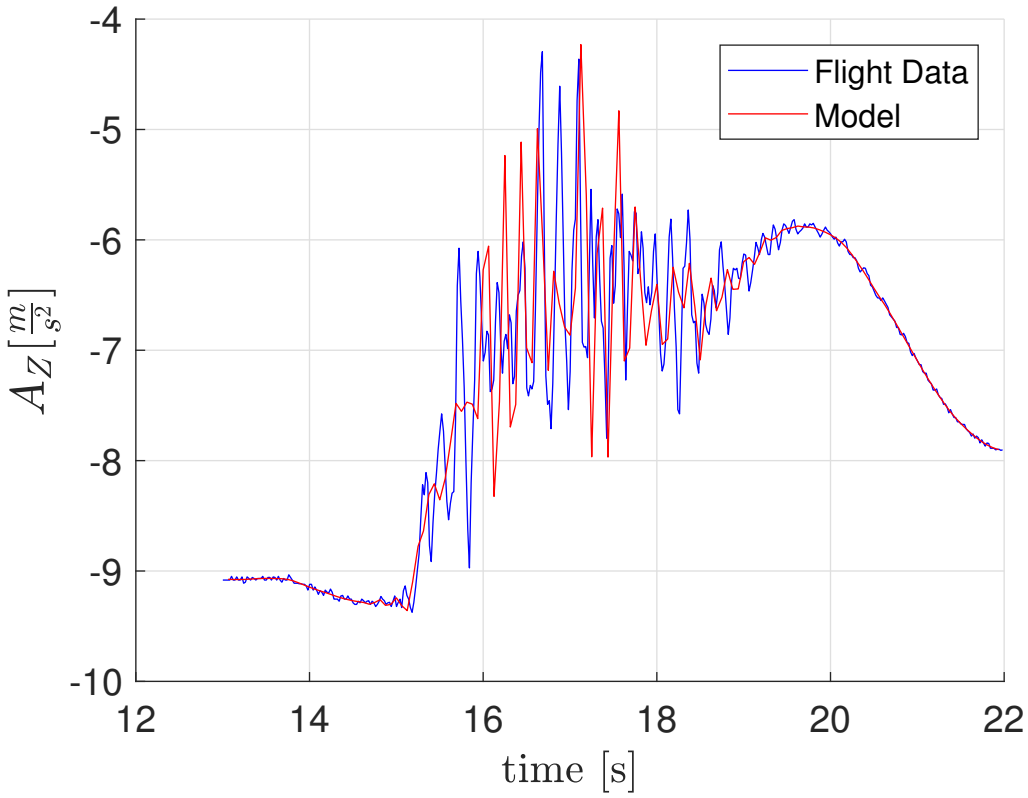

Figure 4.11: Buffet model in vertical direction for altitudes below 5,000 meter in clean configuration.

Figure 4.11 is zoomed in over a time span of nine seconds as this clearly shows the buffet phase-in and phase-out are not modeled correctly for the Fokker data as well.

Chapter 5

Fokker 100 Stall Buffet Modeling

In this chapter, a new methodology on how to model the buffet for the Fokker 100 shall be given. First of all, the phase-in or buffet onset shall be discussed. Secondly, the buffet transient modeling is briefly explained and lastly the buffet offset point is discussed.

An important aspect of the buffet is the buffet onset point as this is the point pilots become aware of an impending stall. In current stall models, the buffet onset is either modeled as surpassing a fixed angle of attack [28] or surpassing a fixed X-parameter threshold of 0.89 [18]. However, when using the X-parameter as buffet onset, the data indicate a different X value for the buffet onset, which can be seen in Figure 5.1.

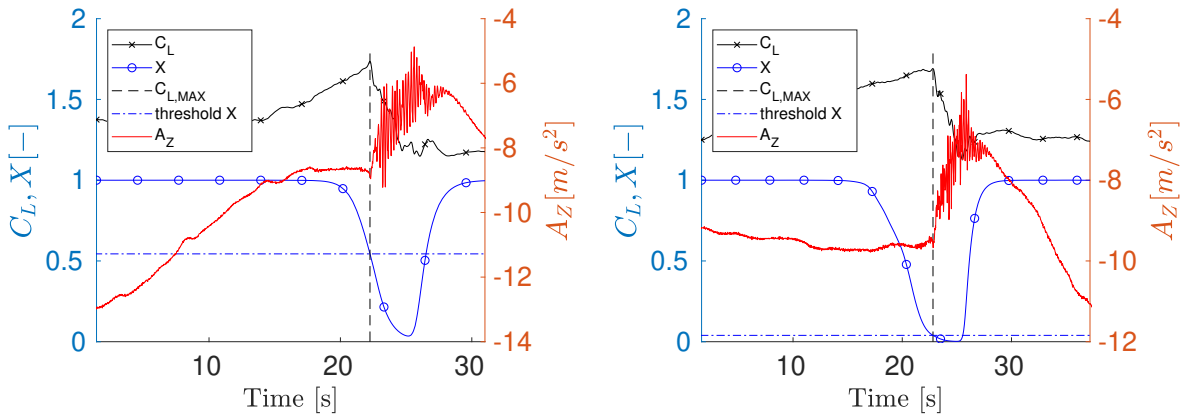

(a) Buffet onset point for the aircraft in clean configuration in terms of vertical acceleration, X-parameter and lift coefficient.

(b) Buffet onset point for the aircraft in clean configuration in terms of vertical acceleration, X-parameter and lift coefficient.

Figure 5.1: Buffet onset based on the X-parameter for aircraft in clean configuration.

Figure 5.1 contains information on the acceleration, the non-dimensional X-parameter and the lift coefficient for different recordings in a clean. As can be seen, the buffet onset is not modeled accurately when the X-parameter is used as onset indicator, as the onset occurs at different values of X.

In the figures, it shows that exceeding the maximum lift coefficient, might be a better indication of the buffet onset. In Figure 5.2 the onset is shown at $C_{L_{max}}$ for the accelerations in lateral and vertical directions in both clean and landing configuration for two other flight recordings. Thus, exceeding the lift coefficient is a better indicator of buffet onset for the Fokker data, when compared to the X-parameter.

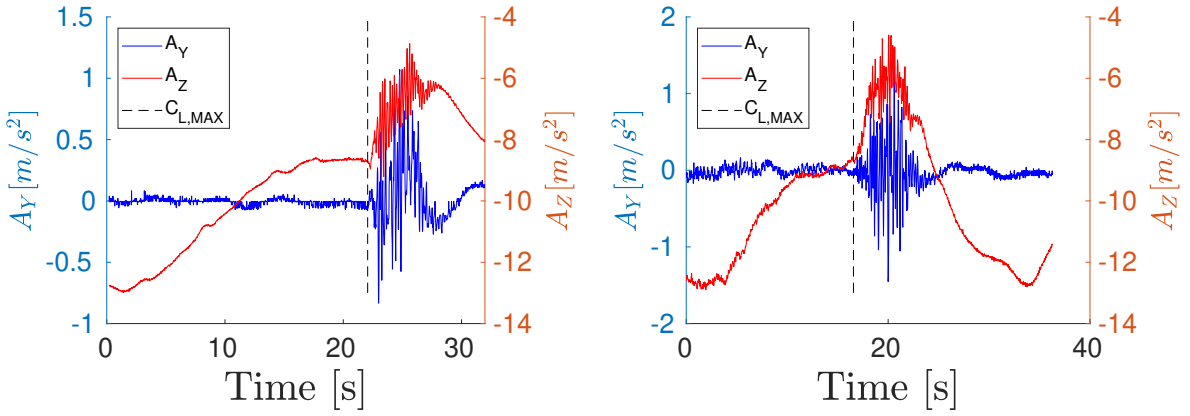

(a) Acceleration in lateral and vertical directionin clean configuration.

(b) Acceleration in lateral and vertical direction in landing configuration

Figure 5.2: Buffet onset based on the maximum lift coefficient in clean and landing configuration for accelerations in lateral and vertical direction.

From a typical lift curve, as shown in Figure 2.1, exceeding the maximum lift coefficient will decrease the lift coefficient and therefore change the slope of the curve from positive to negative. In this research the change in sign for the slope of the lift coefficient versus alpha will be used to model the buffet onset point.

However, a drawback of using the real-life data is that the lift curves typically do not look the one in Figure 2.1. An example, is given in Figure 5.3, where a small dent in the lift curve before the maximum lift coefficient indicates a false positive.

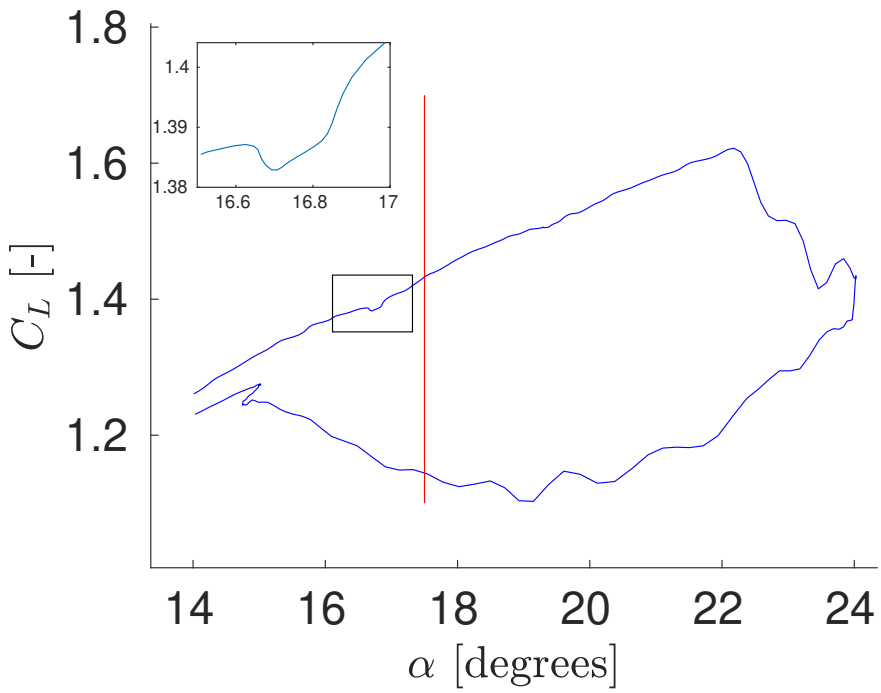

Figure 5.3: Lift coefficient versus alpha curve for the Fokker 100.

Setting an additional constraint reduces the amount of false positives. In this case buffet onset only occurs at angles of attack above 17.5 degrees in conjunction with the change in sign for the slope of the $C_L - \alpha$ curve.

The transient behaviour of the buffet model shall be modeled somewhat similarly as the buffet model in the work of van Horssen [18]. There, the buffet is modeled as a white noise signal shaped through second-order low-pass filters. For this research, the input signal is also assumed white noise, however the peak frequencies are fitted using band-pass filters. A total of three peak frequencies in vertical direction would be fitted as can be seen in Figure 4.3. Additionally, the intensity of the model would be scaled using a gain, which is determined based on different factors, for example, Mach number, angle of attack or dynamic pressure.

It is possible separate the aerodynamic stall model from the buffet model, as the frequencies of each model are sufficiently separated on the frequency axis. The buffet component of the measured accelerations is extraced by subtracting the filtered acceleration from the measured accelerations, give in the formula below:

$$A_{buffet} = A_{measured} - A_{filtered} \tag{5.1}$$

where $A_{measured}$ is the measured acceleration in the vertical direction and $A_{filtered}$ is the filtered acceleration in the vertical direction. A fourth-order Butterworth filter with a zero-order hold is used to filter the data, where the half-power frequency (-3dB) was set at 3 Hertz, as the buffet component in the vertical direction has mainly power at 4.8 Hertz, see Figure 4.3. This buffet component is then compared to the output of the model, which is the shaping filter output multiplied with the gain. Lastly, the buffet offset should be looked into. In current stall models the approach is similar to the approach for the buffet onset [18, 28], which shall also be applied to the Fokker data.

Conclusion

In recent years research has shifted towards modeling of stall dynamics for commercial aircraft as regulations dictate new requirements for upset conditions in flight simulators. Most studies based their models on extensive wind-tunnel data as well as computational fluid dynamics calculations whereas models based on flight test data are uncommon due to the expensiveness and public unavailability of this data. A common conclusion or deficiency is the insufficient haptic feedback of buffeting felt by pilots in a stalled condition when flying in a simulator. However, adequate modeling of the buffet is a recommendation given by ICATEE. Additionally, the buffet is a prime indicator for pilots that an aircraft is outside its safe flight envelope and is likely to be in a stalled condition. Therefore, this research focuses on accurately modeling the buffet onset and transient behavior for flight simulators. Another aspect of this research is to identify the influence of sweep on buffeting behavior.

A database containing over 600 stall maneuvers of the Fokker 100 is available to create a new buffet model. However, not all available stall maneuvers are suitable and therefore the flight data is divided into two different flight conditions, as the buffet intensity and frequency depend on altitude and flight maneuvers. Both flight conditions are based on stalls in idling conditions but differ in aircraft configuration, where the first one flight envelope has 100 stall recordings in a clean aircraft configuration and the other envelope has 99 stall recordings in the landing configuration. Both flight envelopes are in the subsonic flight regime between approximately 4,000 and 6,000 meters. A further division into three different altitudes was based on the Desdemona visit and as the buffet intensity also depends on dynamic pressure. Therefore, both flight envelopes are further divided into altitudes below 5,000 meter, altitudes between 5,000 and 5,500 meter and altitudes above 5,500 meter.

Analysis of the buffet in each body-axis showed some remarkable effects. As there were pilot seat accelerometers at some stall recordings a periodogram was made for these accelerometers as well as at the IRS location. It showed that the intensity of the buffet was higher in all aircraft body axis but was found at lower frequencies in the spectrum. An increase in intensity is attributed due to the relative position to the center of gravity and therefore a longer arm has a higher moment, thus intensity. As for the lower frequencies, this might be due to the nonrigid aircraft structure which has a certain structural damping mode and thus lowers the frequency. However, this is still under investigation.

As already mentioned, the buffet onset and buffet transient behavior is not accurately modeled in the current settings and is also clearly visible in the figure and thus requires further research.

As a practical relevance, the identified buffet model will contribute to the field of flight simulator UPRT and will help increase model fidelity. An increase in model fidelity leads to increased pilot awareness and avoids negative training which increases UPRT effectiveness. Increasing training effectiveness mitigates LOC-I occurrences and will ultimately increase aviation safety.

References

[1] Boeing. Statistical Summary of Commercial Jet Airplane Accidents, 2016. Retrieved on September 27, 2018, from http://www.boeing.com/resources/boeingdotcom/company/about_bca/pdf/statsum.pdf .

[2] International Civil Aviation Organization. 2017 Safety Report, 2017. Retrieved on September 27, 2018, from https://www.icao.int/safety/Documents/ICAO_SR_2017_18072017.pdf .

[3] Airbus S.A.S. A Statistical Analysis of Commercial Aviation Accidents 1958-2017, 2017. Retrieved on September 27, 2018, from https://www.airbus.com/content/dam/corporate-topics/publications/safety-first/Airbus-Commercial-Aviation-Accidents-1958-2017.pdf.

[4] International Civil Aviation Organization. 2018 Safety Report, 2018. Retrieved on September 27, 2018, from https://www.icao.int/safety/Documents/ICAO_SR_2018_30082018.pdf .

[5] CAST/ICAO Common Taxonomy Team. Aviation Occurrence Categories - Definitions and Usage Notes, 2017. Retrieved on October 2, 2018, from http://www.intlaviationstandards.org/Documents/OccurrenceCategoryDefinitions.pdf .

[6] European Aviation Safety Agency. Opinion No 06/2017, 2017. Retrieved on October 2, 2018, from https://www.easa.europa.eu/sites/default/files/dfu/Opinion%20No%2006-2017.pdf .

[7] Federal Aviation Administration. 120-109A - Stall Prevention and Recovery Training with Change 1, 2017. Retrieved on October 2, 2018, from https://www.faa.gov/documentLibrary/media/Advisory_Circular/AC_120-109A_CHG_1.pdf .

[8] International Air Transport Association. Loss of Control In-Flight Accident Analysis Report, 2015. Retrieved on September 27, 2018, from https://www.iata.org/whatwedo/safety/Documents/LOC-I-1st-Ed-2015.pdf .

[9] Jacboson, S.R. *Aircraft Loss of Control Causal Factors and Mitigation Challenges*. (Technical Report DFRC-E-DAA-TN1949)., Edwards, CA, United States: NASA Dryden Flight Research Center, 2010.

[10] Crider, D.A. *Need for Upset Recovery Training*. Guidance, Navigation, and Control and Co-located Conferences. American Institute of Aeronautics and Astronautics, 2008. doi:10.2514/6.2008-6864.

[11] Federal Aviation Administration. AC 120-111 - Upset Prevention and Recovery Training - with Change, 2017. Retrieved on October 2, 2018, from https://www.faa.gov/documentLibrary/media/Advisory_Circular/AC_120-111_CHG_1.pdf .

[12] Advani, S. and Field, J. Upset Prevention and Recovery Training in Flight Simulators. *In AIAA Modeling and Simulation Technologies Conference: American Institute of Aeronautics and Astronautics*, 2011. doi:10.2514/6.2011-6698.

[13] Caruana, D., Correge, M., Reberga, O., Despre, C. & Mignosi, A. *Buffet and buffeting active control*. Fluid Dynamics and Co-located Conferences. American Institute of Aeronautics and Astronautics, 2000. doi:10.2514/6.2000-2609.

[14] Caruana, D., Mignosi, A., Corrège, M., Le Pourhiet, A. & Rodde, A. M. Buffet and buffeting control in transonic flow. *Aerospace Science and Technology*, 9(7):605–616, 2005. https://doi.org/10.1016/j.ast.2004.12.005.

[15] Schroeder, J.A., Burki-Cohen, J.S., Shikany, D., Gingras, D.R., & Desrochers, P.P. . An Evaluation of Several Stall Models for Commercial Transport Training. *In AIAA Modeling and Simulation Technologies Conference: American Institute of Aeronautics and Astronautics.*, 2014. doi:10.2514/6.2014-1002.

[16] Smets, S.E.C. Subjective Noticeability of Variations in Quasi-Steady Aerodynamic Stall Dynamics. Master's thesis, Delft University of Technology, 10 2018.

[17] van Ingen, J. Dynamic Stall Modeling for the Cessna Citation II. Master's thesis, Delft University of Technology, 10 2017.

[18] van Horssen, L.J., de Visser, C.C. & Pool, D.M. Aerodynamic Stall and Buffet Modeling for the Cessna Citation II Based on Flight Test Data. *In 2018 AIAA Modeling and Simulation Technologies Conference: American Institute of Aeronautics and Astronautics.*, 2018. doi: 10.2514/6.2018-1167.

[19] O'Rourke, M.J., Ralston, J.N., Bell, J.W. & Lash, S.F. *PC-based simulation of the F-16/MATV*. Guidance, Navigation, and Control and Co-located Conferences. American Institute of Aeronautics and Astronautics, 1997. doi:10.2514/6.1997-3728.

[20] Kay, J., Ralston, J.N. & Lash, S.F. *Development of non-linear, low-speed aerodynamic model for the F-16/VISTA*. Guidance, Navigation, and Control and Co-located Conferences. American Institute of Aeronautics and Astronautics, 1997. doi:10.2514/6.1997-3576.

[21] Dickes, E., Ralston, J.N. & Lawson, K. *Application of large-angle data for flight simulation*. Guidance, Navigation, and Control and Co-located Conferences. American Institute of Aeronautics and Astronautics, 2000. doi:10.2514/6.2000-4584.

[22] McKeehen, P.D., Cord, T. J. & Nguyen, B.T. *Modified VISTA/F-16 piloted simulation study*. Guidance, Navigation, and Control and Co-located Conferences. American Institute of Aeronautics and Astronautics, 1996. doi:10.2514/6.1996-3508.

[23] Klein, V., Ratvasky, T.R. & Cobleigh, B.R. *Aerodynamic parameters of High-Angle-of attack Research Vehicle (HARV) estimated from flight data*. (Technical Report NASA-TM-102692)., Hampton, VA, United States: NASA Langley Research Center, 1990.

[24] Bowers, A.H., Pahle, J.W., Wilson, R.J., Flick, B.C & Rood, R.L. *An Overview of the NASA F-18 High Alpha Research Vehicle*. (Technical Report NASA-TM-4772)., Edwards, CA, United States: NASA Dryden Flight Research Center, 1996.

[25] National Aeronautics and Space Administration. NASA Armstrong Fact Sheet: F-18 High Angle-of-Attack (Alpha) Research Vehicle, 2014. Retrieved on December 14, 2018, from https://www.nasa.gov/centers/armstrong/news/FactSheets/FS-002-DFRC.html .

[26] Foster, J.V., Cunningham, K., Fremaux, C.M., Shah, G.H. and Stewart, E.C. and Rivers, R.A., Wilborn, J.E., & Gato, W. *Dynamics Modeling and Simulation of Large Transport Airplanes in Upset Conditions*. Guidance, Navigation, and Control and Co-located Conferences. American Institute of Aeronautics and Astronautics, 2005. doi:10.2514/6.2005-5933.

[27] Murch, A.M. and Foster, J.V. *Recent NASA Research on Aerodynamic Modeling of Post-Stall and Spin Dynamics of Large Transport Airplanes*. Aerospace Sciences Meetings. American Institute of Aeronautics and Astronautics, 2007. doi:10.2514/6.2007-463.

[28] Abramov, N.B., Goman, M.G., Khrabrov, A.N., Kolesnikov, E.N., and Fucke, L., Soemarwoto, B. & Smaili, H. *Pushing Ahead - SUPRA Airplane Model for Upset Recovery*. Guidance, Navigation, and Control and Co-located Conferences. American Institute of Aeronautics and Astronautics, 2012.

[29] Groen, E., Ledegang, W., Field, J., Smaili, H., Roza, M., Fucke, L., Nooij, S., Goman, M., Mayrhofer, M., Zaichik, L., Grigoryev, M. & Biryukov, V. *SUPRA - Enhanced Upset Recovery Simulation*. Guidance, Navigation, and Control and Co-located Conferences. American Institute of Aeronautics and Astronautics, 2012. doi:10.2514/6.2012-4630.

[30] Liu, S.F., Luo, Z., Moszczynski, G., & Grant, P.R. *Post-stall Aerodynamic Model Identification of a T-tailed Turbo-prop Aircarft*. AIAA SciTech Forum. American Institute of Aeronautics and Astronautics, 2016. doi: 10.2514/6.2016-1039.

[31] Grant, P.R., Luo, Z., Liu, S.F., & Moszczynski, G.J. . Development of Post-stall Flight Models from Certification Flight Test and Wind-tunnel Data. *In AIAA Modeling and Simulation Technologies Conference: American Institute of Aeronautics and Astronautics*, 2017. doi: 10.2514/6.2017-1549.

[32] Teng, T. Representative Post-Stall Modeling of T-tailed Regional Jets and Turboprops for Upset Recovery Training. Master's thesis, University of Toronto, 2016.

[33] Gingras, D.R., Ralston, J.N., Oltman, R., and Wilkening, C., Watts, R. & Derochers, P. *Flight Simulator Augmentation for Stall and Upset Training*. AIAA SciTech Forum. American Institute of Aeronautics and Astronautics, 2014. doi:10.2514/6.2014-1003.

[34] Grant, P.R. and Moszczynski, G.J. and Schroeder, J.A. *Post-stall Flight Model Fidelity Effects on Full Stall Recovery Training*. AIAA AVIATION Forum. American Institute of Aeronautics and Astronautics, 2018. doi:10.2514/6.2018-2937.

[35] Dias, J.N. Unsteady and Post-Stall Model Identification Using Dynamic Stall Maneuvers. *In AIAA Atmospheric Flight Mechanics Conference: American Institute of Aeronautics and Astronautics.*, 2015. doi: 10.2514/6.2015-2705.

[36] Bérard, A. and Isikveren, A.T. Conceptual Design Prediction of the Buffet Envelope of Transport Aircraft. *Journal of Aircraft*, 46(5):1593–1606, 2009. doi: 10.2514/1.41367.

[37] van Eijndhoven, J.N.A. Buffet envelope prediction of transport aircraft during the conceptual design phase: Predict transonic, shock induced buffet onset. Master's thesis, Delft University of Technology, 2012.

[38] de Paula, A.A., Kleine, V.G. & Porto, F.M. *The Thickness Effect on Symmetrical Airfoil Flow Characteristics at low Reynolds number*. AIAA SciTech Forum. IOS Press, 2017. doi:10.2514/6.2017-1422.

[39] Obert, E. *Aerodynamic Design of Transport Aircraft*. IOS Press 2009, Amsterdam, 2009.

[40] Anderson, J.D. Jr. *Introduction to Flight*. McGraw-Hill, 1221 Avenue of the Americas, New York, NY 10020, 7th edition, 2012.

[41] Shevell, R.S. *Fundamentals of Flight*. Prentice Hall, Inc, 2 edition, 1989.

[42] Gingras, D.R. and Ralston, J.N. Aerodynamics Modeling for Upset Training. *In AIAA Modeling and Simulation Technologies Conference and Exhibit: American Institute of Aeronautics and Astronautics.*, 2008. doi:10.2514/6.2008-6870.

[43] Ralston, J.N., Gingras, D.R., Wilkening, C. & Descrochers, P. *The Application of Potential Data Sources for Simulator Compliance with ICATEE Recommended Stall Modeling Requirements*. Guidance, Navigation, and Control and Co-located Conferences. American Institute of Aeronautics and Astronautics, 2012. doi:10.2514/6.2012-4568.

[44] Yang, Z., Igarashi, H., Martin, M. & Hu, H. *An Experimental Investigation on Aerodynamic Hysteresis of a Low-Reynolds Number Airfoil*. Aerospace Sciences Meetings. American Institute of Aeronautics and Astronautics, 2008. doi:10.2514/6.2008-315.

[45] Fischenberg, D. *Identification of an unsteady aerodynamic stall model from flight test data*. Guidance, Navigation, and Control and Co-located Conferences. American Institute of Aeronautics and Astronautics, 1995. doi:10.2514/6.1995-3438.

[46] Lemley, C. and Mullans, R. *Buffeting pressures on a swept wing in transonic flight - Comparison of model and full scale measurements*. Structures, Structural Dynamics, and Materials and Co-located Conferences. American Institute of Aeronautics and Astronautics, 1973. doi:10.2514/6.1973-311.

[47] Liguore, S. and Pitt, D. Aircraft Buffet Prediction Using Unsteady Aerodynamic Wind Tunnel Model Six-Component Balance Data. *In 45th AIAA/ASME/ASCE/AHS/ASC Structures, Structural Dynamics & Materials Conference: American Institute of Aeronautics and Astronautics.*, 2004. doi:10.2514/6.2004-2045.

[48] Huston, W.B., Rainey, A.G. & Baker, T.F. *A Study of the Correlation Between Flight and Wind-Tunnel Buffeting Loads*. (Technical Report NACA-RM-L55E16b)., Langley Field, VA, United States: National Advisory Committee for Aeronautics. Langley Aeronautical Lab., 1955.

[49] Skopinski, T.H. and Huston, W.B. *A semi-empirical procedure for estimating wing buffet loads in the transonic region*. (Technical Report NACA-RM-L56E01)., Langley Field, VA, United States: National Advisory Committee for Aeronautics. Langley Aeronautical Lab., 1956.

[50] Davis, D.D., Jr and Wornom, D.E. *Buffet Tests of an Attack-airplane Model with Emphasis on Analysis of Data from Wind-tunnel Tests*. (Technical Report NACA-RM-L57H13)., Langley Field, VA, United States: National Advisory Committee for Aeronautics. Langley Aeronautical Lab., 1957.

[51] Lawson, S., Greenwell, D & Quinn, M.K. *Characterisation of Buffet on a Civil Aircraft Wing*. AIAA SciTech Forum. American Institute of Aeronautics and Astronautics, 2016. doi:10.2514/6.2016-1309.

[52] Dang, H., and Yang, Z. . Buffet Onset Prediction and Flow Field Around a Buffeting Airfoil at Transonic Speeds. *In 51st AIAA/ASME/ASCE/AHS/ASC Structures, Structural Dynamics, and Materials Conference: American Institute of Aeronautics and Astronautics.*, 2010. doi:10.2514/6.2010-3051.

[53] D.G. Mabey. Some aspects of aircraft dynamic loads due to flow separation. *Progress in Aerospace Sciences*, 26(2):115–151, 1989. https://doi.org/10.1016/0376-0421(89)90006-7.

[54] Bérard, A., Rizz, A. & Isikveren, A.T. Development and Implementation of Aerodynamic Analysis Methods for Aircraft Conceptual Design . *Canadian Aeronautics and Space Institute Annual General Meeting. Aircraft Design & Development Symposium.*, 2007. Retrieved on March 13, 2019, from `https://www.researchgate.net/publication/274706692_Development_and_Implementation_of_Aerodynamic_Analysis_Methods_for_Aircraft_Conceptual_Design` .

[55] Brunet, V. *Computational Study of Buffet Phenomenon with Unsteady RANS Equations*. Fluid Dynamics and Co-located Conferences. American Institute of Aeronautics and Astronautics, 2003. doi:10.2514/6.2003-3679.

[56] Federal Aviation Administration. AC 25-7D - Flight Test Guide for Certification of Transport Category Airplanes, 2018. Retrieved on September 23, 2019, from `https://www.faa.gov/documentLibrary/media/Advisory_Circular/AC_25-7D.pdf` .

[57] Danowsky, B.P. and Schulze, P.C. *Control Surface Buffet Load Measurement using Aircraft Actuators*. AIAA SciTech Forum. American Institute of Aeronautics and Astronautics, 2016. doi:10.2514/6.2016-2005.

[58] Nocedal, J. and Wright, S.J. *Numerical Optimization*. Springer-Verlag New York Inc., New York, 2 edition, 2006.

[59] Courtland, D.P. *Stability and Control: Flight Testing*. Pergamon, The Boulevard, Langford Lane, Kidlington ,Oxford, 2 edition, 2014.

[60] Lai, M.J. and Schumaker, L.L. *Spline Functions on Triangulations*. Cambridge University Press, 2007.

[61] De Visser, C.C., Chu, Q.P. & Mulder, J.A. *Global Nonlinear Aerodynamic Model Identification with Multivariate Splines*. 2009.

[62] de Boor, C. B-form Basics. *Society For Industrial and Applied Mathematics*, pages 131–148, 1987.

[63] Hu, X.L., Han, D.F. & Lai, M.J. Bivariate Splines of Various Degrees for Numerical Solution of Partial Differential Equations. *SIAM Journal on Scientific Computing*, 29:1338–1354, 2007.

Appendices

Appendix I

Introduction Appendices

The appendices contain additional information to the final thesis report. In Appendix II an overview of all the Fokker 100 recordings used in this research can be found. Vibration analysis for the Fokker 100 is based on Fokker report V-28-106 and is presented in Appendix III, where the most dominant frequencies and modes have been identified. In Appendix IV additional results for the Fokker 100 buffet model are presented. Appendices V to XIII have been published in a separate document due to the sensitivity of the information. These appendices are available upon request. In Appendix VI and VII, the buffet onset and offset for all recordings in either configuration is shown. Appendices VIII to XI, show the periodogram and the frequency response fits. Appendices XII and XIII show the results for the full buffet model. In Appendix XIII, an overview of all validation recordings including the buffet model for the Cessna Citation is presented. Lastly, appendix XIV concludes the thesis report with recommendations for future research.

Appendix II

Overview Fokker 100 Recordings

In this appendix an overview shall be given for all recordings used to train and validate the buffet model in either direction. In Table II.1 an overview of all recordings in the clean configuration is shown and Table II.2 shows all recordings in the landing configuration.

Table II.1: All recordings used for training and validation in the clean configuration.

Rec. No.	Training Rec.	Validation Rec.	Rec. No.	Training Rec.	Validation Rec.
1	100000006	100000103	28	100000298	100000380
2	100000007	100000105	29	100000299	100000381
3	100000008	100000106	30	100000300	100000382
4	100000009	100000111	31	100000329	100000383
5	100000010	100000112	32	100000330	100000384
6	100000213	100000139	33	100000331	100000385
7	100000214	100000141	34	100000334	100000386
8	100000215	100000149	35	100000335	100000401
9	100000224	100000150	36	100000336	100000402
10	100000225	100000151	37	100000337	100000403
11	100000226	100000158	38	100000338	100000404
12	100000228	100000159	39	100000339	
13	100000229	100000160	40	100000349	
14	100000230	100000170	41	100000357	
15	100000249	100000188	42	100000358	
16	100000250	100000189	43	100000359	
17	100000251	100000190	44	100000360	
18	100000252	100000191	45	100000361	
19	100000274	100000309	46	100000362	
20	100000275	100000310	47	100000363	
21	100000276	100000311	48	100000364	
22	100000277	100000317	49	100000405	
23	100000286	100000318	50	100000424	
24	100000287	100000319	51	100000425	
25	100000288	100000320	52	100000426	
26	100000289	100000347	53	100000477	
27	100000297	100000379	54	100000478	

Table II.2: All recordings used for training and validation in the landing configuration.

Rec. No.	Training Rec.	Validation Rec.	Rec. No.	Training Rec.	Validation Rec.
1	100000023	100000113	28	100000344	100000327
2	100000024	100000114	29	100000345	100000328
3	100000221	100000115	30	100000346	100000394
4	100000222	100000116	31	100000353	100000395
5	100000223	100000146	32	100000354	100000397
6	100000235	100000147	33	100000355	100000398
7	100000236	100000148	34	100000373	100000399
8	100000237	100000155	35	100000374	100000400
9	100000238	100000156	36	100000375	100000412
10	100000269	100000157	37	100000376	
11	100000270	100000165	38	100000377	
12	100000271	100000166	39	100000378	
13	100000272	100000167	40	100000414	
14	100000273	100000168	41	100000415	
15	100000282	100000175	42	100000416	
16	100000283	100000176	43	100000417	
17	100000284	100000177	44	100000418	
18	100000294	100000187	45	100000419	
19	100000295	100000209	46	100000420	
20	100000296	100000210	47	100000421	
21	100000305	100000211	48	100000422	
22	100000306	100000212	49	100000423	
23	100000307	100000314	50	100000434	
24	100000308	100000315	51	100000435	
25	100000332	100000316	52	100000436	
26	100000333	100000325			
27	100000343	100000326			

Appendix III

Vibration Analysis Fokker 100

In several flight tests, additional accelerometers were installed, which were located at the fintips, wingtips and the pilot seats. A total of 54 recordings were used to determine the mode-shaped frequencies of the Fokker 100 in a clean configuration only. Figure III.1 shows the periodogram of the fin tip accelerations in the lateral and vertical direction. Analysis of the Fokker 100 buffet characteristics and identifying the buffet peak-frequencies is based on Fokker report V-28-106.

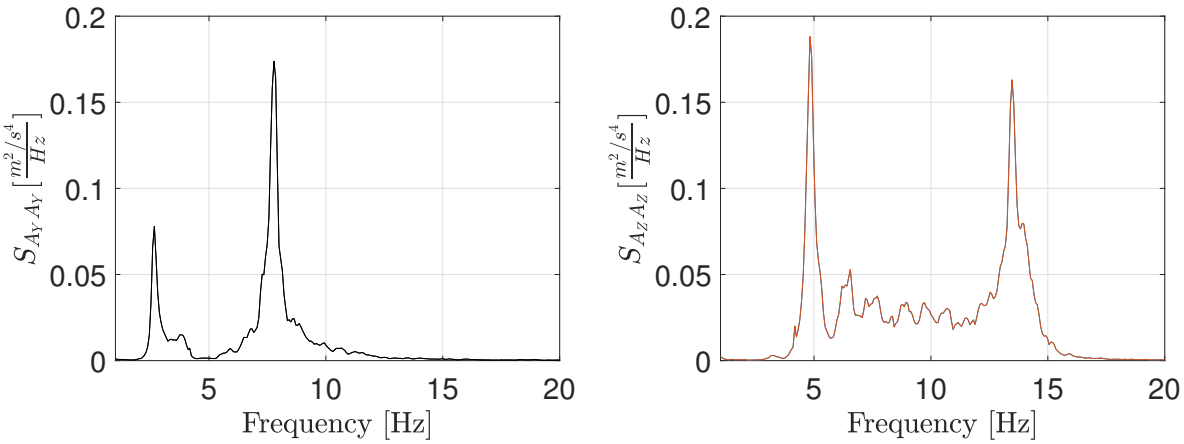

(a) Periodogram for the fin tip accelerations in lateral direction.

(b) Periodogram for the fin tip accelerations in vertical direction.

Figure III.1: Periodogram in lateral and vertical direction for measured accelerations at the fin tips in clean configuration.

Certain frequencies have a peak in the periodogram in Figure III.1 and correspond to a specific eigenmode shape of the Fokker 100. In Table III.1 these vibration mode-shapes can be found.

Table III.1: Vertical fin vibration mode shapes.

Symmetrical modes		Asymmetrical modes	
Origin	Frequency	Origin	Frequency
Fuselage vertical bending	4.8236 Hz	Fin bending	2.6653 Hz
Fuselage bending and engine roll	6.5505 Hz	Fin torsion	3.8188 Hz
Stabilizer bending	13.903 Hz	Wing bending	7.2754 Hz

In Figure III.2 the vibrations on the wing tips of the right and left wing are depicted. In these recordings, accelerations were measured at the front and rear spar of the wing tips. It can be seen that front and rear spar measurements are almost identical.

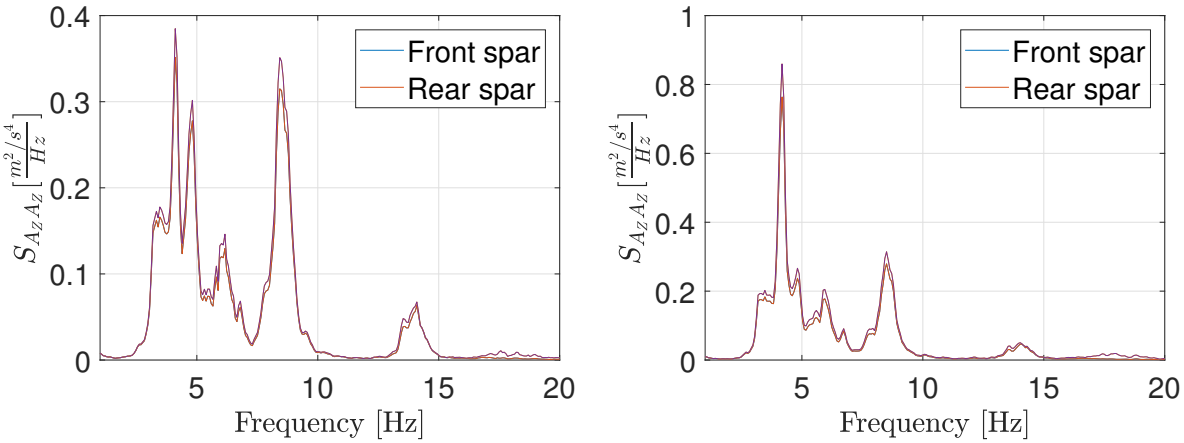

(a) Periodogram for the right wing in vertical direction.

(b) Periodogram for the left wing in vertical direction.

Figure III.2: Periodogram in vertical direction for measured accelerations at the fin wing tips in clean configuration.

From this figure also several new eigenmode shapes for the Fokker 100 were identified, which can be found in Table III.2.

Table III.2: Wing vibration symmetrical mode shapes.

Origin	Frequency
1^{st} wing bending	3.4707 Hz
Engines yaw/pitch	4.1437 Hz
Fuselage vertical bending	4.8167 Hz
Fuselage bending and engine roll	6.5875 Hz
2^{nd} wing bending	8.4952 Hz
Stabilizer bending	14.202 Hz

Lastly, the periodogram and the mode shapes for the pilot seat vibrations are shown in Figure III.3 and Table III.3.

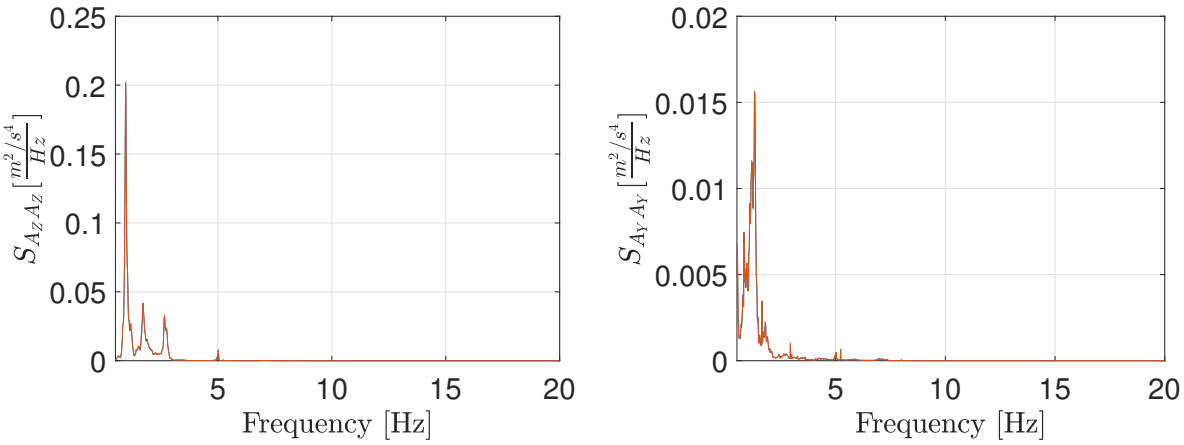

(a) Periodogram for the pilot seat in vertical direction.

(b) Periodogram for the pilot seat in lateral direction.

Figure III.3: Periodogram in lateral and vertical direction for measured accelerations at the pilot seat in clean configuration.

Table III.3: Pilot seat vibration mode shapes.

Symmetrical modes		Asymmetrical modes	
Origin	Frequency	Origin	Frequency
Airplane pitch	0.9463 Hz	Airplane yaw	1.2995 Hz
Airplane heave	2.6978 Hz	Airplane roll	1.7090 Hz
Fuselage vertical bending	5.0141 Hz		

Appendix IV

Fokker 100 Buffet Modeling

An overview of the modeling of the buffet for the Fokker 100 can be found in this chapter. Approximately 60% of the recordings are used for training the model whereas the remaining 40% is used for validation purposes. In section IV.1 results for the buffet onset and offset are given. Parameter correlations for the frequency response fit are given in section IV.2. Lastly, the results of the gain scheduling procedure using multivariate B-splines is described in section IV.3. However, in the paper, a multivariate polynomial using linear regression was used, as this has a reduced complexity compared to the multivariate B-splines.

IV.1 Buffet Onset and Offset

Although buffet onset starts buffeting, the buffet intensity is not maximum, as the buffet builds up quadratically to its maximum according to Courtland [59]. Therefore, a median duration in seconds was used to model the transient time of the buffet onset to reach the maximum buffet intensity. The median duration was taken as the one-sample Kolmogorov–Smirnov test (KS-test) and Shapiro-Wilk test (SW-test) indicated that a normal distribution could not be assumed. In Table IV.1 the values for the tests are shown.x

Table IV.1: KS-test and WS-test test values for the onset duration.

	KS-test	p-value KS-test	WS-Test	p-value SW-test
Clean AY	1	$1.7645e-16$	1	$6.2885e-06$
Clean Az	1	$3.0118e-21$	1	$1.0746e-05$
Landing AY	1	$4.1339e-29$	1	$2.9997e-05$
Landing AZ	1	$1.0768e-30$	1	$6.8245e-04$

The number '1' in the table indicates that the hypothesis of a normal distribution with a significance of 5% is rejected. In Figure IV.1 the median of the time to the maximum buffet is depicted. The two top sub-figures (sub-figures (a) and (b)) indicate the aircraft in clean configuration, whereas the bottom two figures (sub-figures (c) and (d)) indicate the aircraft in landing configuration. In the landing configuration, the onset times are approximately twice as large. The letter "N" indicates the total number of recordings.

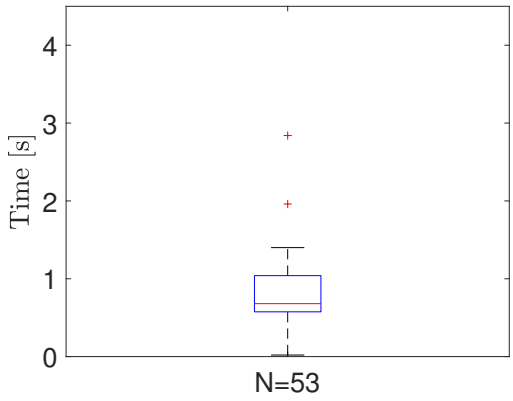

(a) Median buffet onset duration in vertical direction in clean configuration.

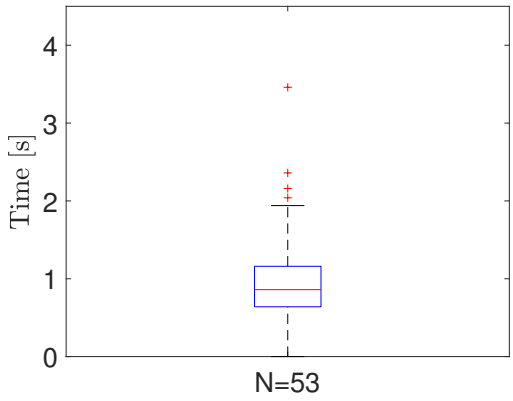

(b) Median buffet onset duration in lateral direction in clean configuration.

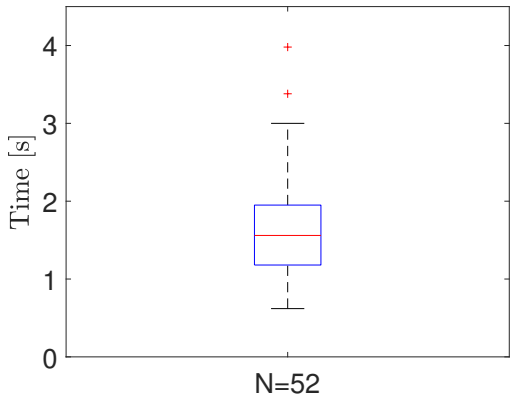

(c) Median onset time in vertical direction for an aircraft in landing configuration.

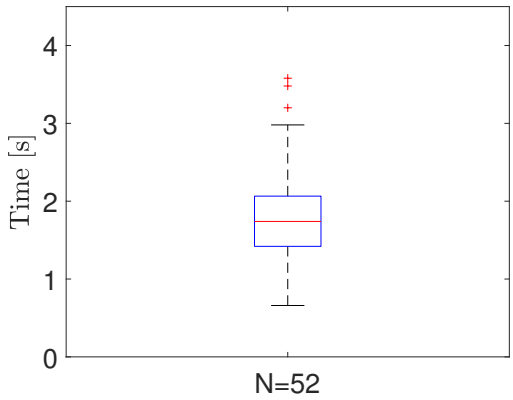

(d) Median onset time in lateral direction for an aircraft in landing configuration.

Figure IV.1: Median buffet onset duration for the Fokker 100 in clean and landing configuration for accelerations in lateral and vertical direction.

A similar approach is used for the offset of the buffet, i.e. when aircraft is recovered and buffeting ends. For the Fokker 100, the aircraft is recovered once the angle of attack starts to increase again. However, depending on the severity and duration of the stall, this angle of attack varies. However, when the angle of attack starts to increase again the change in the angle of attack ($\dot{\alpha}$) changes sign (from negative in the stall, to positive after the stall). Thus, the buffet offset is determined when the angle of attack rate changes from positive to negative. In Figure IV.2 the buffet onset point is visualized, where the minimum angle of attack corresponds with a zero change in the angle of attack rate for both the landing and clean configurations.

Airflow attaches at lower angles of attack due to the hysteresis effect. Therefore, a similar constraint as for the buffet onset is set, which is exceeding an angle of attack. In this case, the angle of attack has to be below 17.5 degrees. Buffet intensity also decreases when the airflow re-attaches, therefore a similar approach as for the onset is used. The buffet onset is scaled down when the rate of change in the angle of attack starts to increase again, up until the buffet offset.

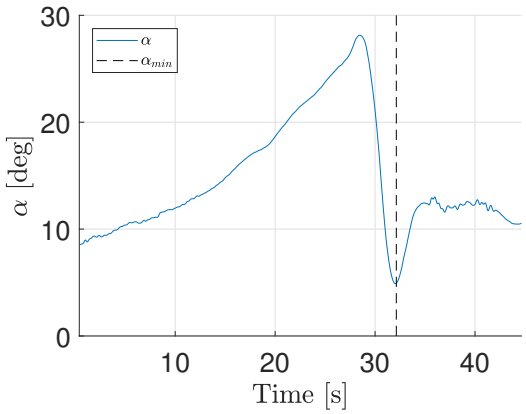

(a) Buffet offset in vertical direction for an aircraft in clean configuration.

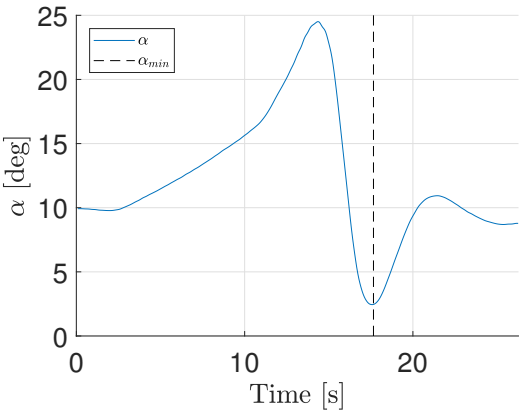

(b) Buffet onset and offset in lateral direction for an aircraft in clean configuration.

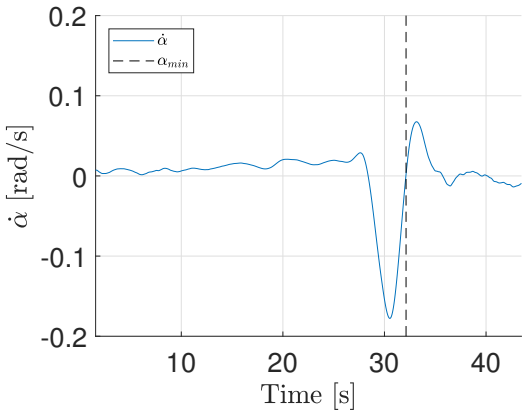

(c) Buffet offset in vertical direction for an aircraft in landing configuration.

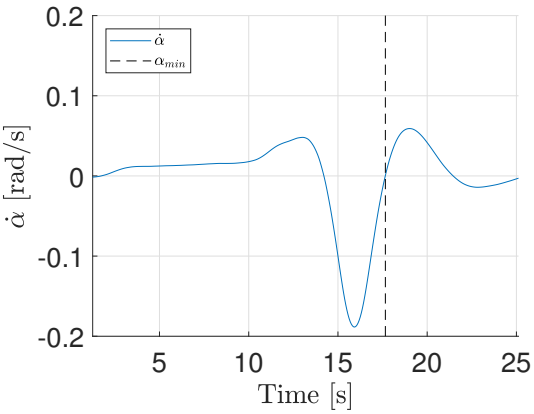

(d) Buffet onset and offset in lateral direction for an aircraft in landing configuration.

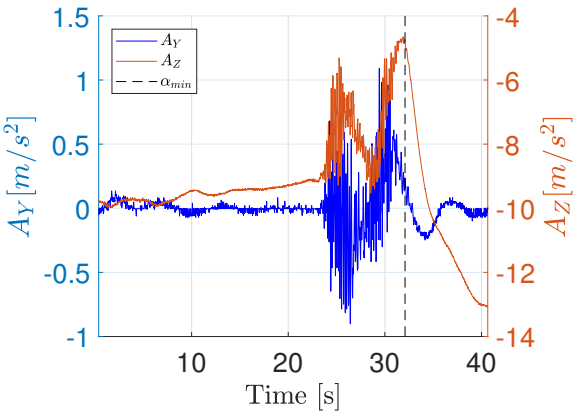

(e) Buffet offset in vertical direction for an aircraft in landing configuration.

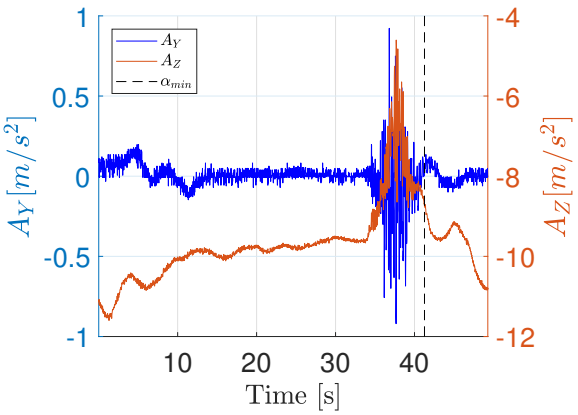

(f) Buffet onset and offset in lateral direction for an aircraft in landing configuration.

Figure IV.2: Buffet offset point in both clean and landing configuration.

An overview with the buffet onset, buffet offset and 95% accelerations confidence interval is given in Figure IV.3.

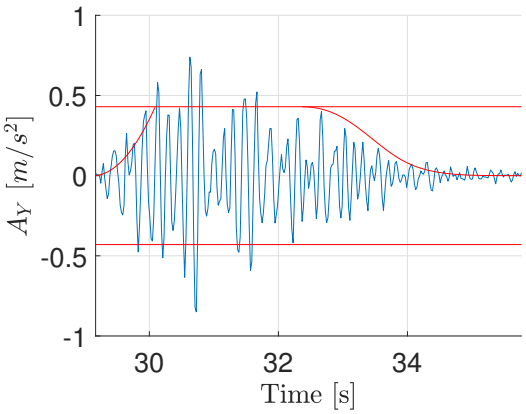

(a) Buffet onset and offset in vertical direction for an aircraft in clean configuration.

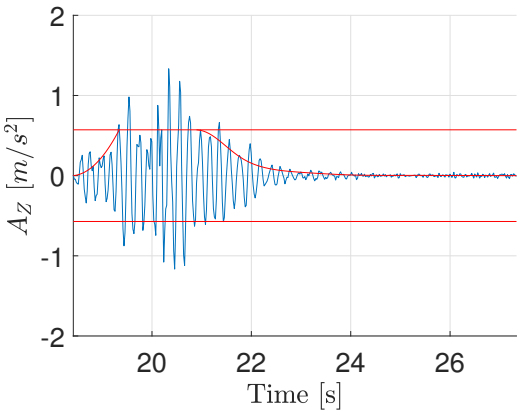

(b) Buffet onset and offset in lateral direction for an aircraft in clean configuration.

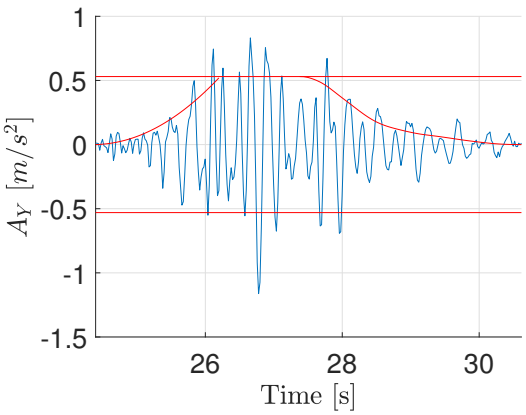

(c) Buffet onset and offset in vertical direction for an aircraft in landing configuration.

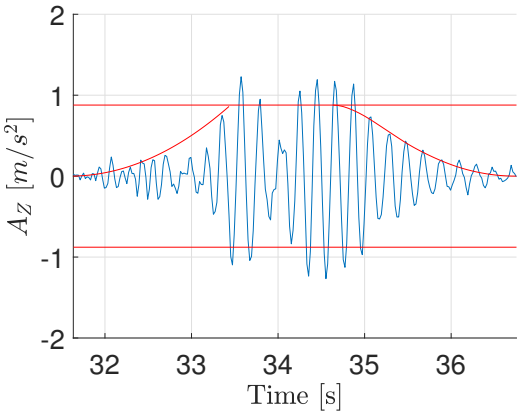

(d) Buffet onset and offset in lateral direction for an aircraft in landing configuration.

Figure IV.3: Buffet onset and offset for aircraft in clean and landing configuration for accelerations in lateral and vertical direction.

IV.2 Frequency Response Fit Parameters

The frequency response fit for each second-order band-pass filter is fitted separately. Therefore, correlations between frequency response fit parameters are given for each band-pass filter. In Table IV.2 and Table IV.3 the parameter correlations in lateral direction in clean and landing configuration respectively are given. In Table IV.4 and Table IV.5 the parameter correlations in lateral direction in clean and landing configuration respectively are given.

Table IV.2: Frequency response fit parameter correlations in lateral direction in clean configuration.

	H_1	ω_1	Q_1	H_2	ω_2	Q_2	H_3	ω_3	Q_3	H_4	ω_4	Q_4
H_1	1.0000	-0.1574	-0.7271									
ω_1	-0.1574	1.0000	-0.1265									
Q_1	-0.7271	-0.1265	1.0000									
H_2				1.0000	0.1888	-0.6781						
ω_2				0.1888	1.0000	0.0769						
Q_2				-0.6781	0.0769	1.0000						
H_3							1.0000	-0.0467	-0.6407			
ω_3							-0.0467	1.0000	-0.2861			
Q_3							-0.6407	-0.2861	1.000			
H_4										1.0000	0.0606	-0.6441
ω_4										0.0606	1.0000	0.2517
Q_4										-0.6441	0.2517	1.0000

Table IV.3: Frequency response fit parameter correlations in lateral direction in landing configuration.

	H_1	ω_1	Q_1	H_2	ω_2	Q_2	H_3	ω_3	Q_3	H_4	ω_4	Q_4
H_1	1.0000	-0.1975	-0.7189									
ω_1	-0.1975	1.0000	0.3110									
Q_1	-0.7189	0.3110	1.0000									
H_2				1.0000	0.0125	-0.7003						
ω_2				0.0125	1.0000	0.0375						
Q_2				-0.7003	0.0375	1.0000						
H_3							1.0000	0.2267	-0.6433			
ω_3							0.2267	1.0000	0.2017			
Q_3							-0.6433	0.2017	1.0000			
H_4										1.0000	0.1243	-0.3562
ω_4										0.1243	1.0000	0.5743
Q_4										-0.3562	0.5743	1.0000

Table IV.4: Frequency response fit parameter correlations in vertical direction in clean configuration.

	H_1	ω_1	Q_1	H_2	ω_2	Q_2	H_3	ω_3	Q_3
H_1	1.0000	-0.1504	0.7816						
ω_1	-0.1504	1.0000	0.1243						
Q_1	0.7816	0.1243	1.0000						
H_2				1.0000	0.1499	-0.7011			
ω_2				0.1499	1.0000	-0.0606			
Q_2				-0.7011	-0.0606	1.0000			
H_3							1.0000	-0.7694	-0.2941
ω_3							-0.7694	1.0000	0.7579
Q_3							-0.2941	0.7579	1.0000

Table IV.5: Frequency response fit parameter correlations in vertical direction in landing configuration.

	H_1	ω_1	Q_1	H_2	ω_2	Q_2	H_3	ω_3	Q_3
H_1	1.0000	0.3740	-0.6954						
ω_1	0.3740	1.0000	-0.0462						
Q_1	-0.6954	-0.0462	1.0000						
H_2				1.0000	-0.0301	0.6814			
ω_2				-0.0301	1.0000	0.0009			
Q_2				0.6814	0.0009	1.0000			
H_3							1.0000	-0.0449	0.6672
ω_3							-0.0449	1.0000	-0.1689
Q_3							0.6672	-0.1689	1.0000

Parameters are correlated if the absolute parameter value is greater than 0.9. However, this is not the case for any of the estimated parameters.

IV.3 Multivariate B-Splines

A short and brief introduction on multivariate B-splines is given here, whereas Lai and Schumaker [60] cover a more in depth overview on the matter of splines. In the work of de Visser [61] a multivariate simplex b-spline is applied for global nonlinear model identification purposes. A plus of multivariate b-splines is the fitting of scattered datasets, of which the recordings in this research are a good example.

A multivariate simplex B-spline consists of piecewise polynomials defined on simplices, which are expressed in Barycentric coordinates. A n-simplex t is defined as a convex hull with $n+1$ unique, non-degenerate points in n-dimensional space:

$$t := \langle \mathcal{V}_t \rangle \in \mathbb{R}^n \tag{IV.1}$$

Non-degenerate points are points which change the dimension of simplex t, when removed from simplex t. A simplex spline function $s(\mathbf{x})$ is the collection of all polynomials with a given degree d and predefined continuity order r between simplices t_i:

$$s(\mathbf{x}) = \sum_{i=1}^{M} \delta_i(\mathbf{x}) p^{t_i}(\mathbf{x}) \tag{IV.2}$$

where M is the total number of simplices, $p^{t_i}(\mathbf{x})$ is the polynomial on simplex t_i and $\delta_i(\mathbf{x})$ is the activation function which relates the data points in $\mathbf{x}$ to each simplex with:

$$\delta_i(\mathbf{x}) = \begin{cases} 1, & \text{if } \mathbf{x} \in t_i \\ 0, & \text{if } \mathbf{x} \notin t_i \end{cases} \tag{IV.3}$$

When a set of simplices are combined a triangulation is formed. A triangulation is a partition of the data set, which contains the M non-overlapping simplices:

$$\mathcal{T} := \bigcup_{i=1}^{M} t_i, \;\; t_i \cap t_j \in \{\emptyset, \tilde{t}\}, \;\; \forall (t_i, t_j) \in \mathcal{T}, \;\; i \neq j \tag{IV.4}$$

where $\tilde{t}$ is an n-simplex, with $0 \leq m \leq n-1$. The spline space contains all spline functions s with a given degree d and continuity order C^r on the triangulation $\mathcal{T}$, defined as:

$$S_d^r(\mathcal{T}) := s \in C^r(\mathcal{T}) : s|_t \in P_d, \forall t \in \mathcal{T} \tag{IV.5}$$

where, s is the n-variate simplex spline function with degree d, a continuity of order r on the triangulation $\mathcal{T}$ and where P_d is the space containing all the polynomials of total degree d. A cubic spline with continuity one on a triangulation $\mathcal{T}$ is then given as $S_3^1(\mathcal{T})$.

A local coordinate system, in this case the Barycentric coordinate system, is defined on each n-simplex t. All data points $\mathbf{x}$ in a n-dimensional Cartesian plane can be described using a weighted vector sum of the vertices in the simplex t:

$$\mathbf{x} = \sum_{i=0}^{n} b_i \mathbf{v}_i, \qquad \sum_{i=0}^{n} b_i = 1 \tag{IV.6}$$

where, $b_i \in \mathbb{R}$ are the normalized scalar weights and $\mathbf{v}_i \in \mathbb{R}^n$ the vertices. Transforming from Cartesian to Barycentric coordinates using the properties above, where the barycentric coordinates are calculated with respect to the n-simplex t:

$$\mathbf{x} - \mathbf{v}_0 = \sum_{i=1}^{n} b_i(\mathbf{v}_i - \mathbf{v}_0), \qquad b_0 = 1 - \sum_{i=1}^{n} b_i \tag{IV.7}$$

rewriting it to vector form, will solve for the barycentric coordinates:

$$\begin{bmatrix} b_1 \\ b_2 \\ \vdots \\ b_n \end{bmatrix} = \begin{bmatrix} (\mathbf{v}_1 - \mathbf{v}_0) & (\mathbf{v}_2 - \mathbf{v}_0) & \dots & (\mathbf{v}_n - \mathbf{v}_0) \end{bmatrix}^{-1} (\mathbf{x} - \mathbf{v}_0), \tag{IV.8}$$

A combination of neighboring simplices with Barycentric coordinates, where on each simplex a single simplex polynomial is defined is called an simplex spline function, as given in Equation IV.2. A simplex polynomial $p^{t_i}(\mathbf{x})$ can be expressed in the B-form [62], which is derived from the multinomial theorem:

$$(b_0 + b_1 + \cdots + b_n)^d = \sum_{\kappa_0+\kappa_1+\cdots+\kappa_n=d} \frac{d!}{\kappa_0!\kappa_1! \dots \kappa_n!} \prod_{i=0}^{n} b_i^{\kappa_i} \tag{IV.9}$$

introducing the multi-index κ, which is defined as

$$\kappa := (\kappa_0, \kappa_1, \dots, \kappa_n) s \in \mathbb{N}^{n=1} \tag{IV.10}$$

The multi-index has the following two properties, which are the 1-norm and the factorial given by:

$$\begin{aligned} |\kappa| &= \kappa_0 + \kappa_1 + \cdots + \kappa_n) = d, \qquad d \geq 0, \\ \kappa! &= \kappa_0!\kappa_1 \dots \kappa_n! \end{aligned} \tag{IV.11}$$

recall, $d \in \mathbb{N}$ being the degree of the polynomial. All elements in the multi-index are sorted lexicographically [60,63], which help defining and ensuring continuity. An integer number of possible permutations is defined up to the sum of the degree of the polynomial. The total number of polynomials in Equation IV.13 is determined by the number of valid permutations of κ, which are determined by dimension n and degree d and calculated as:

$$\hat{d} = \frac{(d+n)!}{n!d!} \tag{IV.12}$$

Using the multi-index notation, Equation IV.9 is simplified to

$$(b_0 + b_1 + \cdots + b_n)^d = \sum_{|\kappa|=d} \frac{d!}{\kappa!} \mathbf{b}^{\kappa} \tag{IV.13}$$

The basis function of the multivariate spline in B-form is then defined as:

$$B_{\kappa}^{d}(\mathbf{b}) := \frac{d!}{\kappa!} \mathbf{b}^{\kappa} \tag{IV.14}$$

A n-variate basis function is a stable basis for a space of polynomials of degree d [62], such that any polynomial $p(b)$ with degree d can be written in the B-form:

$$p(\mathbf{b}) = \sum_{|\kappa|=d} c_\kappa B_\kappa^d(\mathbf{b}) \tag{IV.15}$$

where, c_κ are the B-coefficients.

Polynomials from adjacent n-simplices, which share an edge, can be joined together to ensure continuity up to a certain order $r < d$. Continuity conditions are enforced by condinuity conditions which are defiend for two adjacent simpleces and are equal at every point along the edge of the two simplices. In order to achieve a continuity of C^r for an n-variate spline function $s \in S_d^r(\mathcal{T})$ a constraint is set as:

$$c^{t_j}_{(m,\kappa_0,\ldots,\kappa_{n-1})} = \sum_{|\gamma|=m} c^{t_j}_{(0,\kappa_0,\ldots,\kappa_{n-1})+\gamma} B_\gamma^m(\mathbf{v}_{i,j}), \;\; \forall \;\; 0 \leq m \leq r \tag{IV.16}$$

where $\gamma \in \mathbb{R}$ is an independent multi-index similar sized as κ and $B_\gamma^m(\mathbf{v}_{i,j})$ is the B-form polynomial with respect to simplex t_j. Collecting all valid permutations of the multi-indices κ and γ and combining all continuity equations, resulted in the following vector form:

$$\mathbf{Hc} = 0 \tag{IV.17}$$

where, **H** is the smoothness matrix containing all continuity equations and **c** being the global B-coefficients matrix. Ensuring the equality constraints during calculation of the B-coefficients will therefore ensure the order of continuity.

Estimation of the B-coefficients including equality constraints is possible using an Ordinary Least Squares (OLS) technique:

$$\min_{\mathbf{c}} \frac{1}{2}(\mathbf{Y} - \mathbf{Xc})^T(\mathbf{Y} - \mathbf{Xc}), \qquad \text{subject to } \mathbf{Hc} = 0 \tag{IV.18}$$

where **Y** are all measurements and **X** the local regression matrix for all measurements. Using the Lagrange multipliers leads to the following OLS form:

$$\begin{bmatrix} \hat{\mathbf{c}} \\ \hat{\lambda} \end{bmatrix} = \begin{bmatrix} \mathbf{X}^T\mathbf{X} & \mathbf{H}^T \\ \mathbf{H} & 0 \end{bmatrix}^+ \begin{bmatrix} \mathbf{X}^T\mathbf{Y} \\ 0 \end{bmatrix} = \begin{bmatrix} C_1 & C_2 \\ C_3 & C_4 \end{bmatrix}^+ \begin{bmatrix} \mathbf{X}^T\mathbf{Y} \\ 0 \end{bmatrix} \tag{IV.19}$$

such that the estimated B-coefficients are calculated with

$$\hat{\mathbf{c}} = C_1\mathbf{X}^T\mathbf{Y} \tag{IV.20}$$

However, as the smoothness matrix is a sparse matrix and inverse of a rank deficit matrix may cause errors. Therefore, the Kasteljau theorem is used in this research, which is an efficient iterative solver, which is able to deal with the rank deficiency of **H**.

IV.3.1 Multivariate B-Spline Results

A commonly used triangulation is the Delaunay triangulation, which is most flexible when using simplex splines. However, only one pre-defined triangulation is used, as the Delaunay triangulation was not usable, due to the scarceness of the data points, resulting in triangulations without any data points. A rectangular grid triangulation with two simplices was used, based on the minimum and maximum values of the input data.

The resulting spline space in clean and landing configuration is given by $S_2^1(\mathcal{T})$, which is a spline with degree two and a continuity order of one. Also, this spline space yielded the best possible results for the gains in either the lateral or vertical direction. In IV.6b the goodness-of-fit parameter results are shown. A similar result for the goodness-of-fit parameters, Relative Root Mean Squared Error (RMSE_{rel}) and Coefficient of Determination (R^2) is achieved, which indicates that a similar gain proportion was required to model the gains. Even though the RMSE and RMSE_{rel} are rather low in the $S_2^1(\mathcal{T})$, the R^2 value is also rather low, which indicates that the model output does not entirely represent the calculated gains. The low R^2 value is due to the scarceness of data points in combination with the continuity order of one, which smooths the splines over the entire surface and will, therefore, result in not an exact match of the output gains.

Table IV.6: Goodness-of-fit for the $S_2^1(\mathcal{T})$ in clean and landing configuration.

(a) Goodness-of-fit for the $S_2^1(\mathcal{T})$ in landing configuration.

		Lateral direction	Vertical direction
RMSE	[-]	1.709	2.051
$RMSE_{rel}$	[%]	15.55	14.98
R^2	[-]	0.621	0.642

(b) Goodness-of-fit for the $S_2^1(\mathcal{T})$ in clean configuration.

		Lateral direction	Vertical direction
RMSE	[-]	2.158	3.476
$RMSE_{rel}$	[%]	24.06	24.05
R^2	[-]	0.572	0.572

Another measure of the goodness-of-fit of the spline model is checking the variance of the B-coefficients. In the spline space, $S_2^1(\mathcal{T})$ a total of twelve B-coefficients are available, which can also be seen in Figure IV.4. In Figure IV.4 the black dashed lines indicate the values of the B-coefficients whereas the red lines indicate the logarithmic value of the variance per B-coefficient.

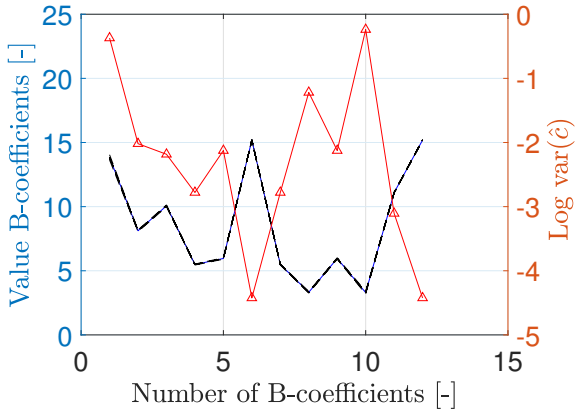

(a) Values and variances of the B-coefficients in lateral direction in clean configuration.

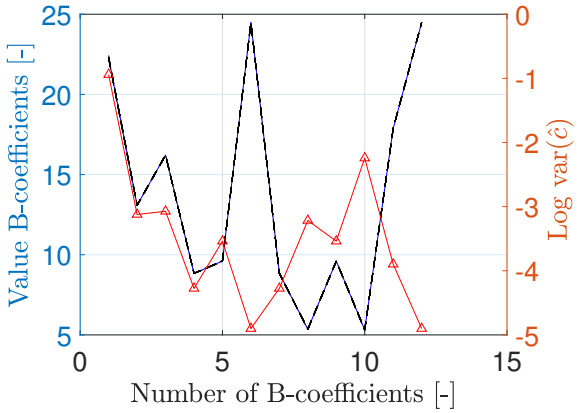

(b) Values and variances of the B-coefficients in vertical direction in clean configuration.

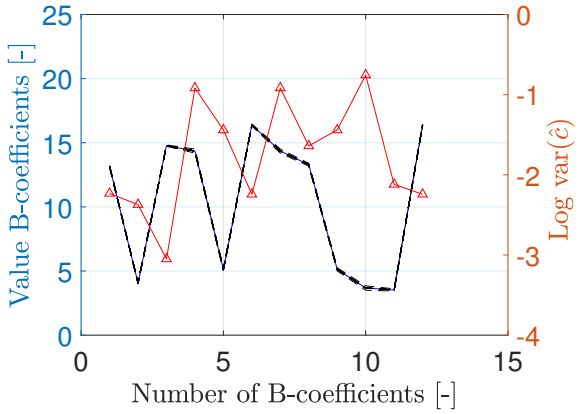

(c) Values and variances of the B-coefficients in lateral direction in landing configuration.

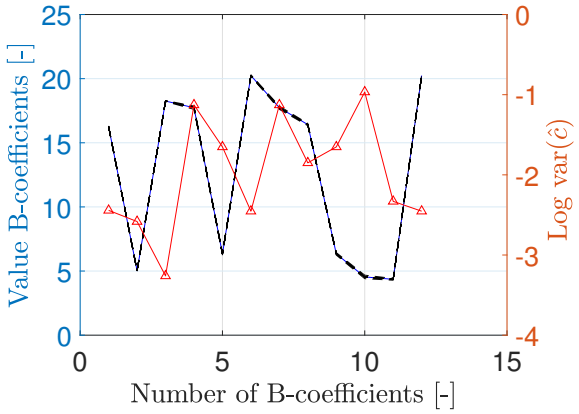

(d) Values and variances of the B-coefficients in vertical direction in landing configuration.

Figure IV.4: Values and variances of the B-coefficients in the clean configuration.

The intensity in the vertical direction is larger than the intensity in the lateral direction, which is also indicated by the higher B-coefficients values. In the clean configuration, in either direction, the variances at the first and tenth B-coefficient are larger compared to the others. In this case, these B-coefficients are located at the regions where fewer data points are available, thus at high deceleration rates and low angles of attack or high angles of attack and low deceleration rates. Additionally, the B-coefficient variances in the vertical direction are lower compared to the ones in the lateral direction, which is opposite

compared to the $RMSE_{rel}$ and RMSE values. In the landing configuration, larger variances are located at the fourth, seventh and tenth B-coefficient in both directions. This is due to the fact of the scarceness of data points in the regions at high dynamic pressures over weight as well as the high dynamic pressure over weight values in combination with low-pressure altitudes. Also, the variances of the B-coefficients in the vertical direction are lower than the variances in the lateral direction, which indicates a better fit in the vertical direction. As mentioned before, the intensity in the vertical direction larger than the intensity in the lateral direction, which is also indicated by the larger B-coefficients values.

Although low $RMSE_{rel}$ and RMSE values are acquired in the model, the R^2 in each spline model is also rather low. This indicates that the regression prediction represents the real data less when compared to the frequency response function. An increase in R^2 value might be achieved by adding more data points to the model, which is not possible with the current method. However, an increase inR^2 might be achieved by lowering the continuity order, as this smooths the flight envelope. Lastly, even though the predicted model output does not approximate the gain values accurately, a low RMSE and high B-coefficient values indicate that the difference in the model output is not too large and therefore the output could represent the buffet. In terms of the variance of the B-coefficients, the variances in the clean configuration are higher compared to the variances in the landing configuration, as a better model fit was achieved in terms of the goodness-of-fit parameters.

Additionally, each B-coefficient has a value greater than zero which indicates that each gain has a positive value, which is necessary for the gain. The larger B-coefficient values in the clean configuration also indicate that the buffet intensity is higher compared to the buffet intensity in landing configuration.

Lastly, due to the relatively simple triangulation and the added complexity of the multivariate B-splines, the multivariate B-splines were converted to a more simple multivariate polynomial model. Similar results were obtained for this multivariate polynomial model.

Appendix XIII

Fokker 100 Stall Buffet Methdology applied on Cessna Citation Data

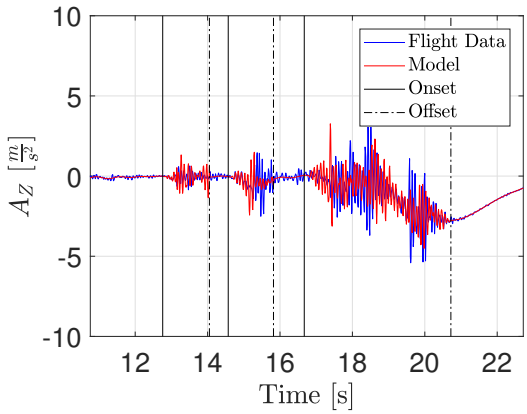

(a) Full buffet model including buffet onset and offset in recording 2 for the measured accelerations in vertical direction in clean configuration.

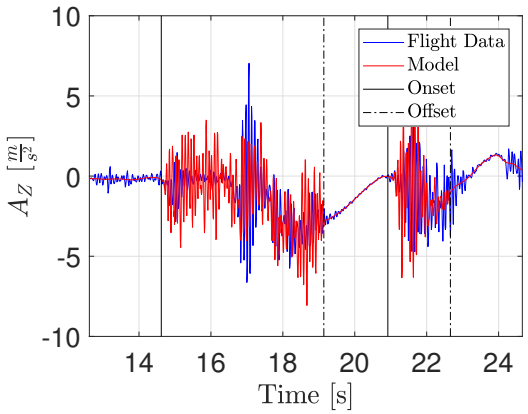

(b) Full buffet model including buffet onset and offset in recording 3 for the measured accelerations in vertical direction in clean configuration.

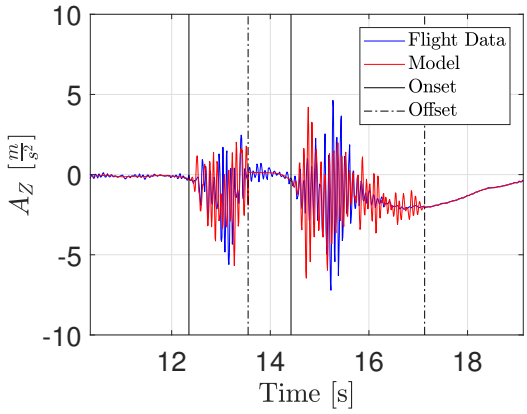

(c) Full buffet model including buffet onset and offset in recording 4 for the measured accelerations in vertical direction in clean configuration.

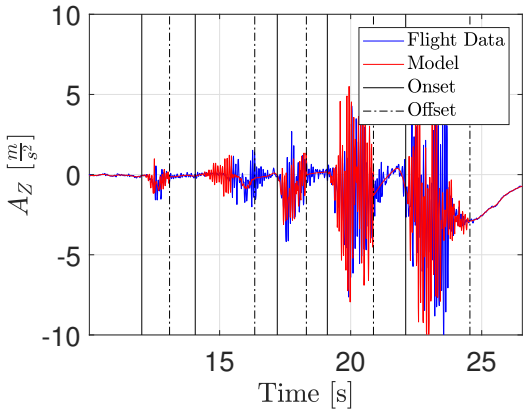

(d) Full buffet model including buffet onset and offset in recording 5 for the measured accelerations in vertical direction in clean configuration.

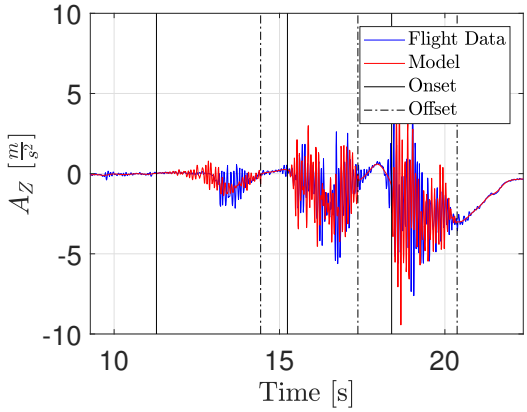

(e) Full buffet model including buffet onset and offset in recording 6 for the measured accelerations in vertical direction in clean configuration.

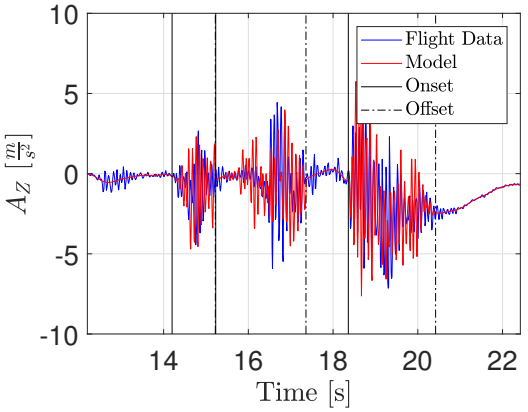

(f) Full buffet model including buffet onset and offset in recording 7 for the measured accelerations in vertical direction in clean configuration.

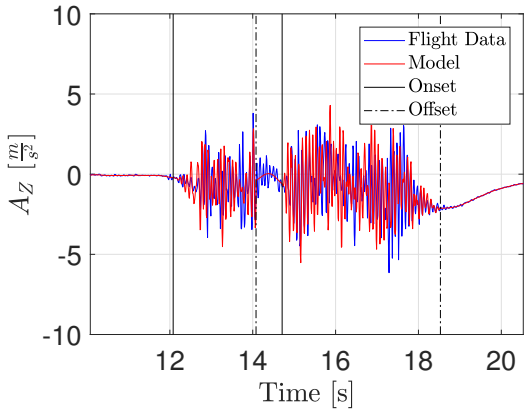

(g) Full buffet model including buffet onset and offset in recording 8 for the measured accelerations in vertical direction in clean configuration.

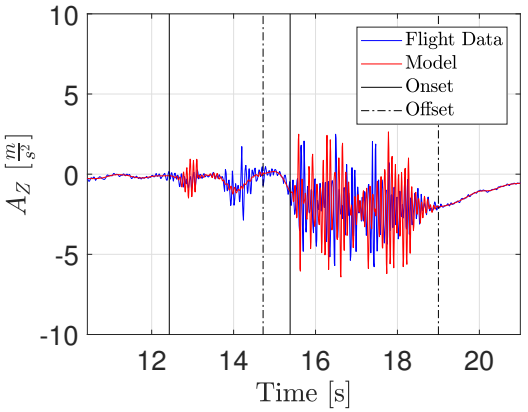

(h) Full buffet model including buffet onset and offset in recording 9 for the measured accelerations in vertical direction in clean configuration.

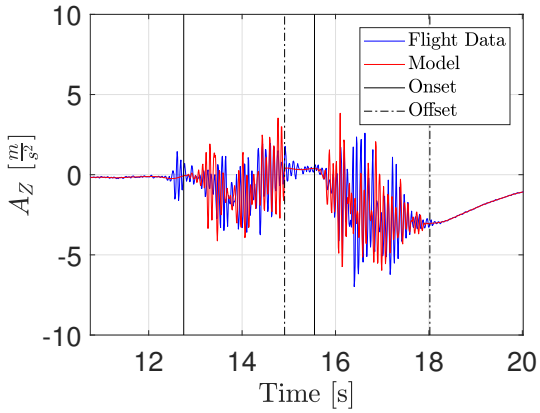

(i) Full buffet model including buffet onset and offset in recording 10 for the measured accelerations in vertical direction in clean configuration.

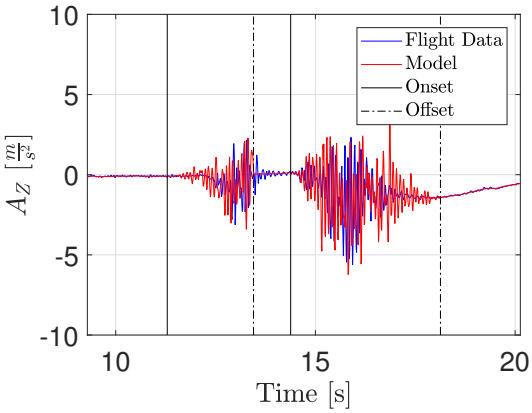

(j) Full buffet model including buffet onset and offset in recording 11 for the measured accelerations in vertical direction in clean configuration.

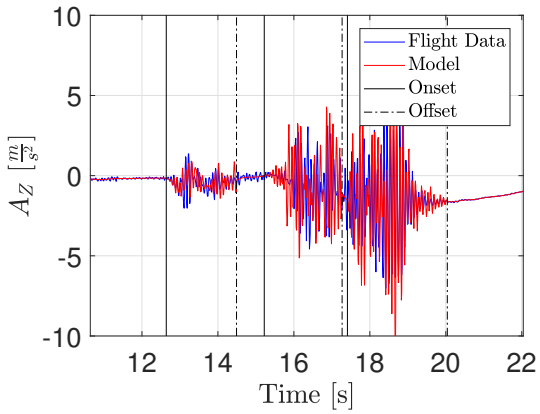

(k) Full buffet model including buffet onset and offset in recording 12 for the measured accelerations in vertical direction in clean configuration.

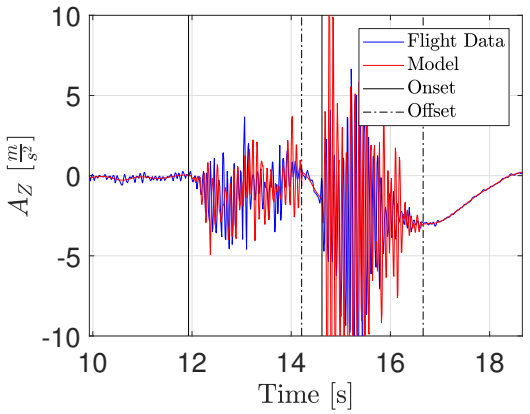

(l) Full buffet model including buffet onset and offset in recording 13 for the measured accelerations in vertical direction in clean configuration.

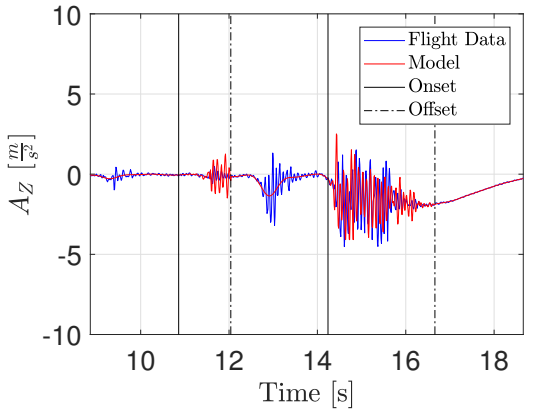

(m) Full buffet model including buffet onset and offset in recording 14 for the measured accelerations in vertical direction in clean configuration.

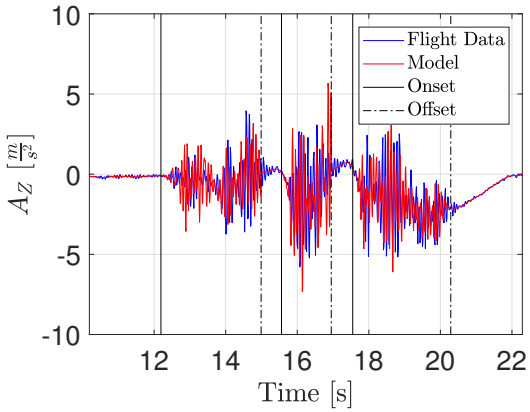

(n) Full buffet model including buffet onset and offset in recording 15 for the measured accelerations in vertical direction in clean configuration.

Figure XIII.1: Buffet model on Cessna Citation data for accelerations in vertical direction in clean configuration.

Appendix XIV

Future Research

In this chapter, an overview of recommendations for future research into buffet stall modeling is given. A quick recap of the research question is given, to indicate the relevance of the research and improvements for future research. The research question was given as:

Research Question

Which current state-of-the-art stall modeling techniques would identify an accurate buffet model in vertical direction for a swept wing aircraft including onset and transient behaviour using flight test data?

In this research, a combination of current-state-of-the art stall modeling techniques was combined to identify a more accurate buffet model in the vertical and lateral direction for two flight conditions, namely aircraft in clean configuration and landing configuration. A total of 190 quasi-stall maneuvers according to JAR-25 were flown, using a 60/40 split were combined to train and validate the models. In each of the four models, onset behavior is identified at the point where the maximum lift coefficient is exceeded in combination with an onset transient time. Secondly, the transient behavior was identified as using multivariate second-order polynomial which modeled the buffet intensity as a gain, and a frequency response fit, which modeled the aircraft specific mode-shape frequencies. Lastly, offset behavior was modeled at the minimum angle of attack in the stall. An additional validation set was run for the Cessna Citation II data, which indicated the generability of the model.

XIV.1 Recommendations

An overview of several recommendations are listed below:

- Due to the limited number of aircraft states required for the research, a fourth-order Butterworth filter with a cut-off frequency at 2 Hertz is used to get state estimates. In concurrent research, a Kalman filtered state estimation is conducted and results from that research could be applied to the current model to yield better results, as the state estimates are likely to be more accurate.
- The buffet onset is based on the change in the slope of the $C_L - \alpha$ curve which is a good indicator of a stall. However, it requires an additional constraint to be modeled accurately, i.e. the angle of attack has to be larger than 17.5 degrees for the Fokker 100. An improved result could be achieved by determining the slope more accurately using better state estimates or finding a more suitable buffet offset point, which may omit the additional constraint.
- The buffet onset transient behavior may be modeled differently, instead of using a median onset duration, the current flight condition could be used, as the data indicated a different onset duration for different flight conditions. Altering the model structure of the multivariate B-splines or

the polynomial model to an onset duration model could also yield a better result for the buffet onset transient on the input conditions.

- In the buffet transient behavior, specifically the splines model, model accuracy could be increased. First of all, the triangulation method could be altered to a pre-defined triangulation or Delaunay triangulation. Secondly, the number of simplices could be increased. Thirdly, the set of input parameters could be increased, as in the number of data points or the number of inputs.
- The improved buffet model could be implemented in the stall model of the Cessna Citation II and a human-in-the-loop experiment in the SIMONA could be performed to determine model accuracy based on SME.
- An extension of the model including the vibrations to the pilot seat could be included. For example, a gain is calculated based on distance from the center of gravity to the pilot seat could be used. In that sense, the gain for the buffet model depends on aircraft type characteristics and will provide the TU with a more generic model.
- Another validation using Cessna Citation data should be conducted. The flight test maneuvers used in this research do not represent the Fokker maneuvers. Also, the model could be validated on other aircraft configurations of the Cessna Citation.